HIGH FREQUENCY RADIO OBSERVATIONS OF TIDES AND CURRENTS SOUTH OF O'AHU

A THESIS SUBMITTED TO THE GRADUATE DIVISION OF THE
UNIVERSITY OF HAWAI'I IN PARTIAL FULFILLMENT
OF THE REQUIREMENTS FOR THE DEGREE OF

MASTER OF SCIENCE

IN

OCEANOGRAPHY

SEPTEMBER 2010

By

Jacob L. Cass

Thesis Committee:

Pierre Flament, Chairperson
Glenn Carter
Brian Powell

We certify that we have read this thesis and that, in our opinion, it is satisfactory in scope and quality as a thesis for the degree of Master of Science in Oceanography.

THESIS COMMITTEE

_____
Chairperson

_____

_____

Contents

Acknowledgments

Thank you to the U.S. Coast Guard for affording me the opportunity to pursue graduate school in paradise. My two years at school have been truly educational, challenging and enjoyable.

To Dr. Pierre Flament, my advisor. Thank you for your counsel, patience and support. The time and efforts you dedicated to teaching and helping me think through problems was invaluable. I feel very lucky to have had the chance to work with you.

Thank you to Dr. Cedric Chavanne for the many helpful lessons along the way. Dr. Glenn Carter and Dr. Brian Powell, thank you for serving on my committee and for your efforts in guiding my progress. To Dr. Mark Merifield, thank you for the guidance and lessons in working with real data. To Dr. Douglas Luther, your insights, suggestions and class notes for investigating island trapped and surface gravity waves were extremely helpful; thank you for taking the time to facilitate my analysis. Mahalo to Tyson Hilmer for your advice and work in processing the beamforming calibrations; without those I would have been lost. Thanks to my friends and classmates Assaf Azouri, Becky Baltes, KR MacDonald and Saulo Soares for keeping things interesting and teaching me the important points I missed in class. Thanks to all RADLAB members for the hard work and dedication you put forward to install the HFR sites.

Finally, thank you to my beautiful wife, Sarah. Your patience, love and kindness helped in dealing with the ups and downs of being a student.

Abstract

A year of radial current data from a high frequency radio current meter (HFR) on Oahu's south shore is analyzed from long to short time scales. Monthly and seasonal currents reveal a large scale inversion in the winter months of the typically westward propagating flow. A region of significant cyclonic flow west of Penguin Bank is identified as an eddy generation zone likely driven by cyclonic wind stress curl. Island trapped waves are investigated while complications from local vorticity and the close proximity of the inertial period are considered. Observed tidal characteristics are compared with three existing models. Incoherent tidal features, presumably attributed to energetic internal tides in the area, are presented. Deep-ocean Assessment and Reporting of Tsunamis (DART) buoy data is used to determine the open ocean characteristics of waves generated by the Samoan and Chilean tsunamis and predict the surfaces currents excited as they approached Oahu. An complex-demodulation based on the frequency of the local sea level fluctuations is conducted to amplify any evidence for the tsunamis in the record because the predicted currents were below the detection threshold of the HFR.

List of Figures

Chapter 1

Introduction

High Frequency Radio (HFR) current meters provide a high resolution record of surface ocean dynamics relevant to operational and theoretical oceanography. Direct applications of vector current fields into high stakes operational missions such as pollution response and search and rescue or research of geophysical flows leave radial currents often overlooked. The analysis contained herein focuses on radial current data from a single HFR current meter on Oahu's southeast shore. While radial current data analysis is less intuitive in a spatial context, rich spectral content provides insights into important processes across the frequency spectrum. The goal of this report is to showcase the diverse processes evident in the radial current data record.

Radial currents collected by the Koko Head HFR current meter are used to investigate surface ocean dynamics from long to short time scales along Oahu's south shore. Chapter 2 describes environmental and instrumental settings. Chapter 3 presents low frequency radial and inferred vector currents. Vector currents were inferred by assuming sub-inertial currents are non-divergent. Chapter 4 investigates evidence for island trapped waves isolated around Oahu. Observed tides are compared with modeled tidal characteristics in Chapter 5. Chapter 6 discusses the unique observation opportunities presented by two tsunami events during the HFR deployment. Finally, Chapter 7 concludes with results and presents suggestions for future work.

Chapter 2

Environmental and Instrumental Setting

2.1 Physical Setting

The Hawaiian archipelago lies isolated in the central Pacific Ocean. The North Equatorial Current, forming the the southern boundary of the North Pacific gyre, drives the large scale oceanic flow to the west. Atmospheric conditions are strongly influenced by the persistent North Pacific high pressure system, causing northeasterly trade winds to dominate. The Hawaiian Islands form a physical barrier to both of these flow regimes.

Mountains rising through the atmospheric inversion layer block the trade winds, creating a wind shadow in their lee and enhanced flow around their extremities (Chavanne et al., 2004; Lumpkin, 1995). The resulting wind stress curl anomalies force Ekman transport divergence at the northern and convergence to the southern extremes of the islands, respectively lifting and depressing the thermocline (Chavanne et al., 2002). Thermocline fluctuations by wind forcing leads to intense eddy formation in the lee of the islands. The series of steep bathymetric slopes from the sea floor to the surface obstruct the North Equatorial Current creating shear instabilities and vortices in the flow (Flament et al., 2001). Counter rotating eddies generated by the Hawaiian islands give rise to an eastward flowing Hawaiian Lee Counter Current that further complicates dynamics (Lumpkin and Flament, 2001).

Recent numerical and observational studies have shown that baroclinic tides are energetic in waters near Oahu (Merrifield et al., 2001; Merrifield and Holloway, 2002; Eich et al., 2004; Carter et al., 2008). When the barotropic tide traverses steep bathymetric features, such as those present in the Ka'iwi and Kauai channels, baroclinic tides are generated. These dramatic bathymetric features represent an area of significant internal wave generation and mixing. These strong internal waves may

represent an intermediate stage in the cascade of energy from tides to turbulence, which may provide a significant portion of the energy required to maintain large scale thermohaline structure (Rudnick et al., 2003).

Penguin Bank, the now submerged remnants of an ancient shield volcano, extends approximately 50 km westward from Molokai with depths as shallow as 50 meters and then quickly drops to depths ~1000 m (Price et al., 2004). Here, the deep, narrow and notoriously turbulent Ka'iwi Channel funnels large scale flows and internal waves between the islands (Figure 2.1).

2.2 Instrument Setting

An HFR current meter atop Koko Head on Oahu's southeast shore collected radial current data from July 2009 through June 2010. The site is situated to observe surface currents south of Oahu, its domain extending south of Penguin Bank and west through Mamala Bay past Barber's Point (Figure 2.2). The HFR is complementary to two other deployment locations along O'ahu's south shore. One of similar characteristics to Koko Head is planned for deployment during the summer of 2010 at Barber's Point. Another smaller site at Kaka'ako park near downtown Honolulu has been in operation since December 2009. The Kaka'ako site is primarily intended to provide favorable geometry for nearshore vector currents along the baseline between Koko Head and Barber's Point and does not provide a large overlapping domain for vector current generation.

Positive radial current is designated as the component of the total current directed away from the receive site. Data is collected every 1.5 km and for each degree between 160°T and 280°T. Plots of radial current and products derived from this data will naturally have higher resolution at shorter ranges because the density of data points is a function of the coordinate system.

The receive array at Koko Head is 14 antennas long, faces to the southwest and is capable of receiving backscatter between 160° and 280° T. The site is operated in frequency-modulated continuous wave (FMCW) mode over 100 kHz bandwidth starting at 16.3 MHz. The averaging time

for each sample is set to 12 minutes every 15 minutes where various calibration measurements are taken during the time remaining. Additional instrumental settings are summarized in table 2.1.

The Koko Head transmit site is a rectangular 4 antenna array orientated to direct the majority of its energy to the southwest (~210°T). The beam forming configuration is intended to form a null toward the receive array minimizing transmission directly to the receive array.

Temporal data coverage changes on short time scales due to signal propagation and ambient electromagnetic noise (Figure 2.3). Longer data gaps are due to hardware failures. Coverage in space illustrates slight suppression of the coverage to the southwest, a direction of documented electromagnetic interference (Figure 2.4; Hilmer 2010). Like the HFR deployment along Oahu's west shore in conjunction with the Hawaiian Ocean Mixing Experiment (HOME; Chavanne, 2007), the Koko Head HFR exhibits slightly increased coverage during the day (average 50% coverage range day / night = 66.5 km / 64.6 km).

Nearly a year of radial current data has been used for the low frequency and tidal analysis in chapters 3 and 5. Only information collected between 01 December 2009 and 06 May 2010 has been analyzed for island trapped waves (chapter 5).

As a data quality assessment the cross correlation of the radial currents between Koko Head and Kaka'ako was evaluated (Figure 2.5). If along baseline and across baseline current components are uncorrelated with equal variance, the correlation pattern would follow that of a cosine of the angle between the two sites (Chavanne, 2007).

Further quality assessment of the accuracy of the HFR was conducted during a shipboard beamforming calibration (Appendix A). Based on the beamforming assessment of Kaka'ako, steered angles beyond ~30 - 45° from normal do not effectively focus the signal. This degraded beamforming at large steered angles may explain the less than ideal cross-correlation pattern.

The location of the Koko Head receive array requires signals collected from the western portion of the domain to propagate across land, including urban areas, and up topographic features before arriving to the site. Assessment of the Koko Head HFR shows observed beamforming patterns closely match the theoretical pattern, tightly focusing energy in the intended look direction. Therefore, any detrimental effects resulting from this over-land path appear to be insignificant and high levels of confidence can be placed in data collected from Koko Head based on the shipboard beamforming calibration.

Operating Characteristic	Relationship	Setting
Frequency		16.315 MHz
Transmitted Power		6 W
Direct Path Rejection		64 dB
Working Range		>90 km
Dynamic Range		135 dB
Bragg Wavelength	$\lambda/2$	9.1875 m
Range Resolution	$c/2B$	100kHz bandwidth => 1.5 km
Velocity Resolution	c/Tf	12 min integration time => 2.55 cm/s
Maximum Velocity	$\sqrt{(gc/2\pi f)}$	5.35 m/s
Azimuthal Resolution		~ 8°

Table 2.1 – Instrumental settings of Koko Head HFR.

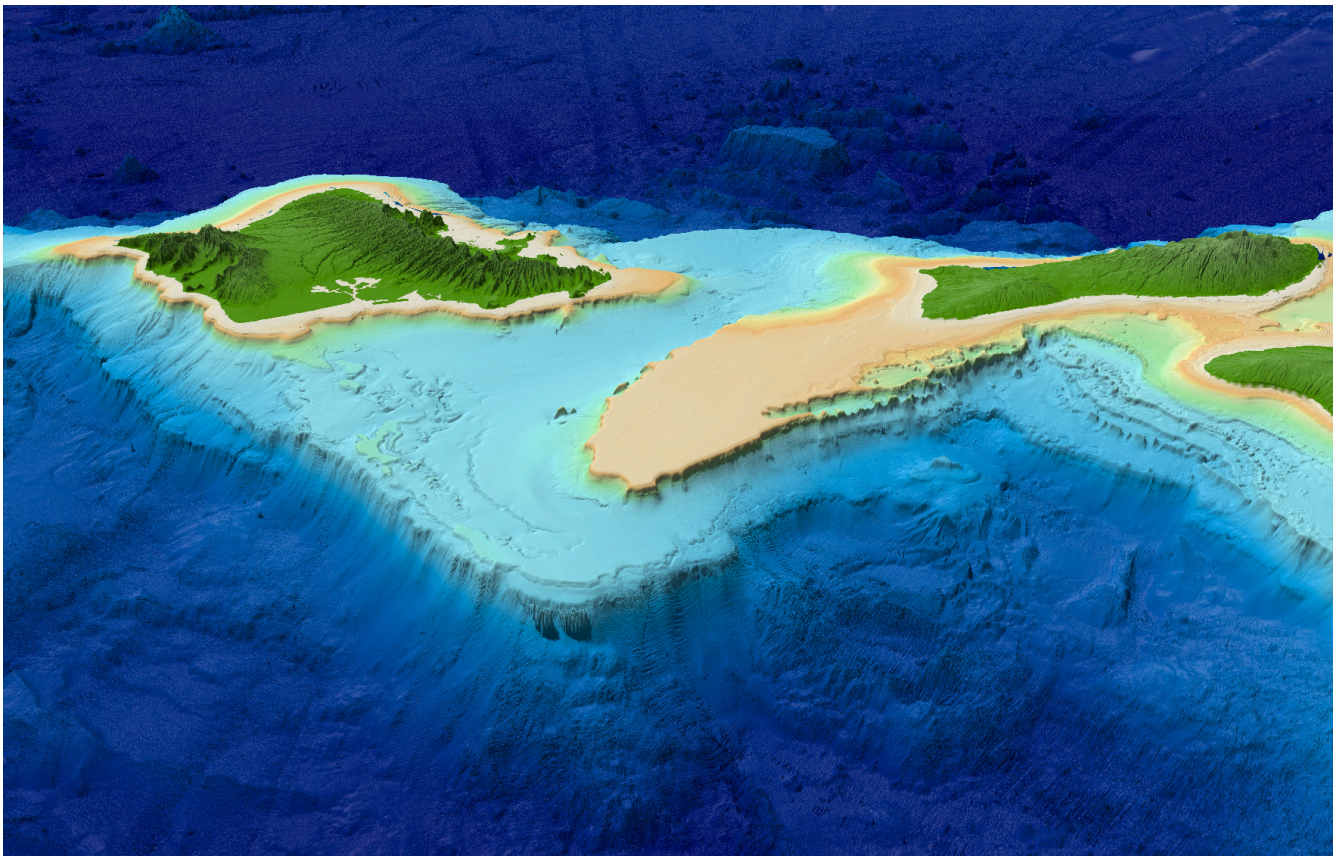

Figure 2.1: Bathymetric features near Oahu and Molokai. Penguin Bank is the shallow shelf extending westward from Molokai.

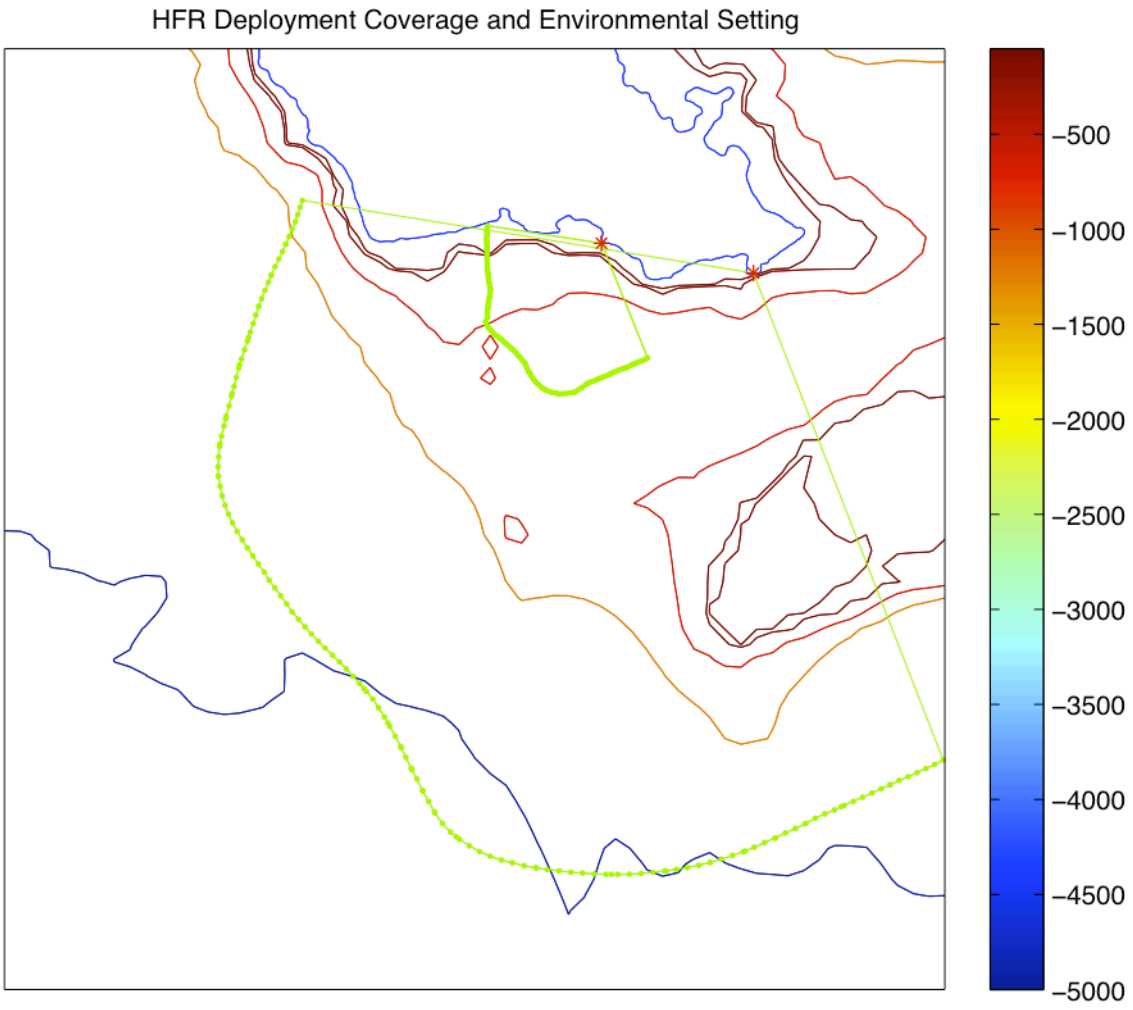

Figure 2.2: Environmental setting of Koko Head and Kaka'ako HFR current meters. Bathymetry (from NOAA ETOPO 1) of Mamala Bay (depth contours at 4000, 1000, 500, 100 and 50 meters) and the 50% coverage limit of Koko Head and Kaka'ako HFR current meters (green lines) between July 7, 2009 and June 15, 2010. Locations of HFR current meters noted by red asterisks.

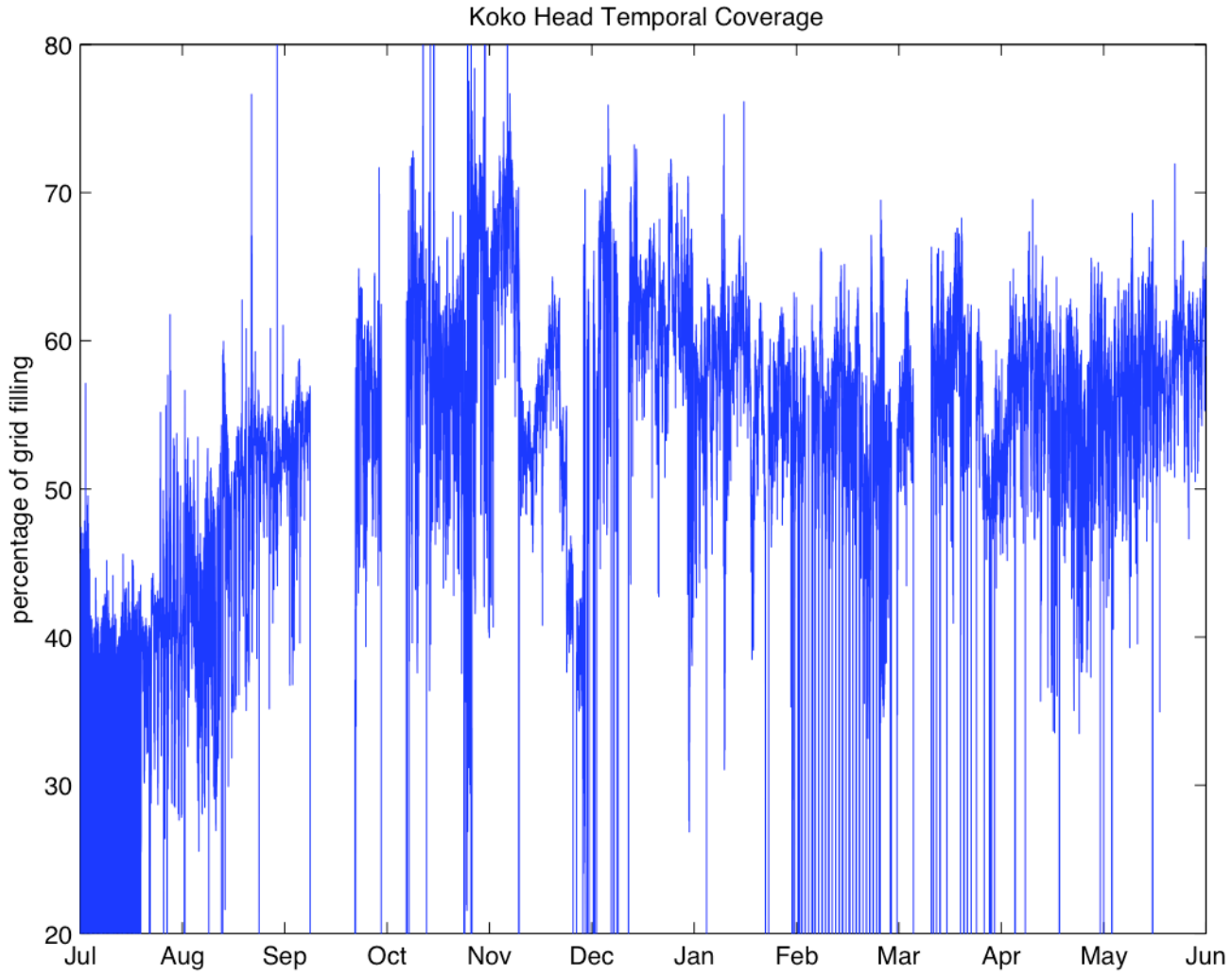

Figure 2.3: Temporal coverage (percentage of grid points with data) for Koko Head HFR current meter Between July 7, 2009 and June 15, 2010.

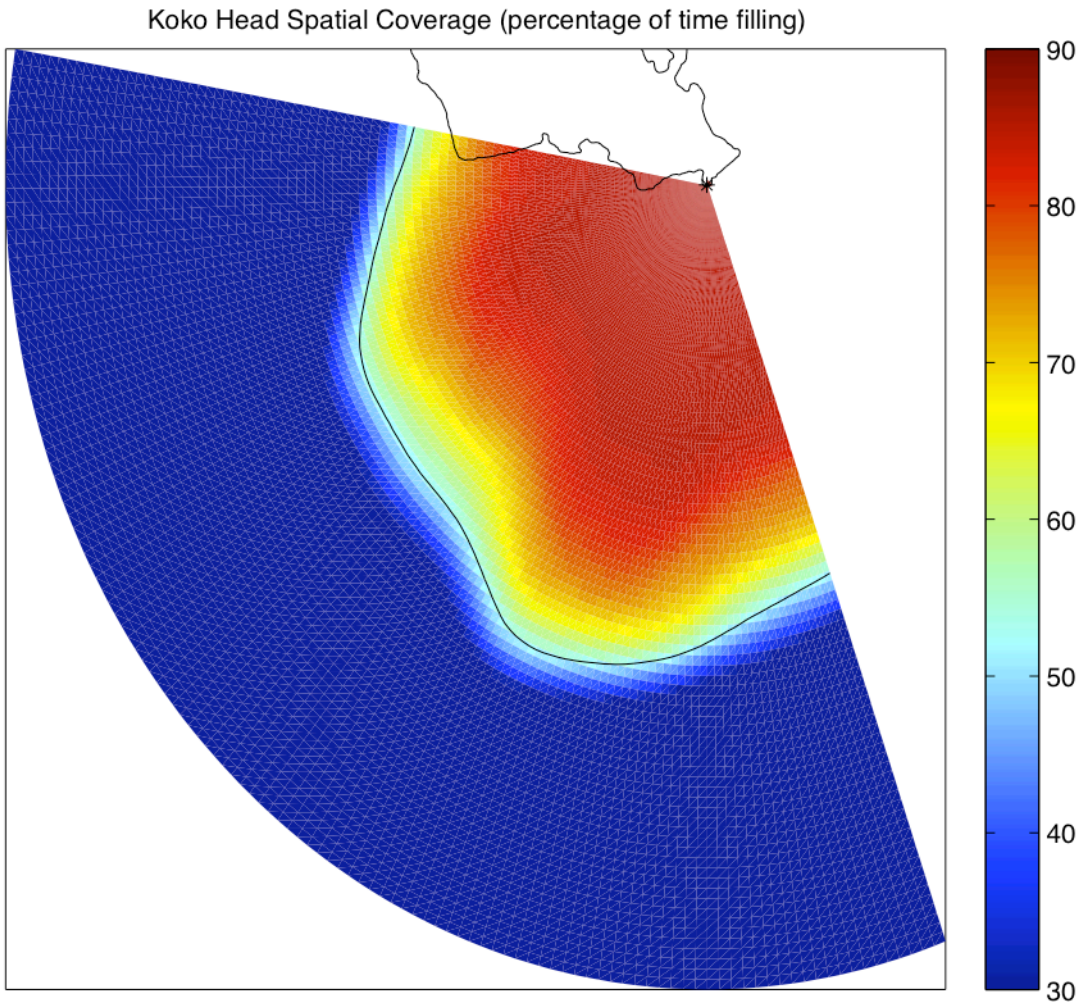

Figure 2.4: Contour of Koko Head Spatial coverage between July 7, 2009 and June 15, 2010. Thin black line indicates 50% coverage.

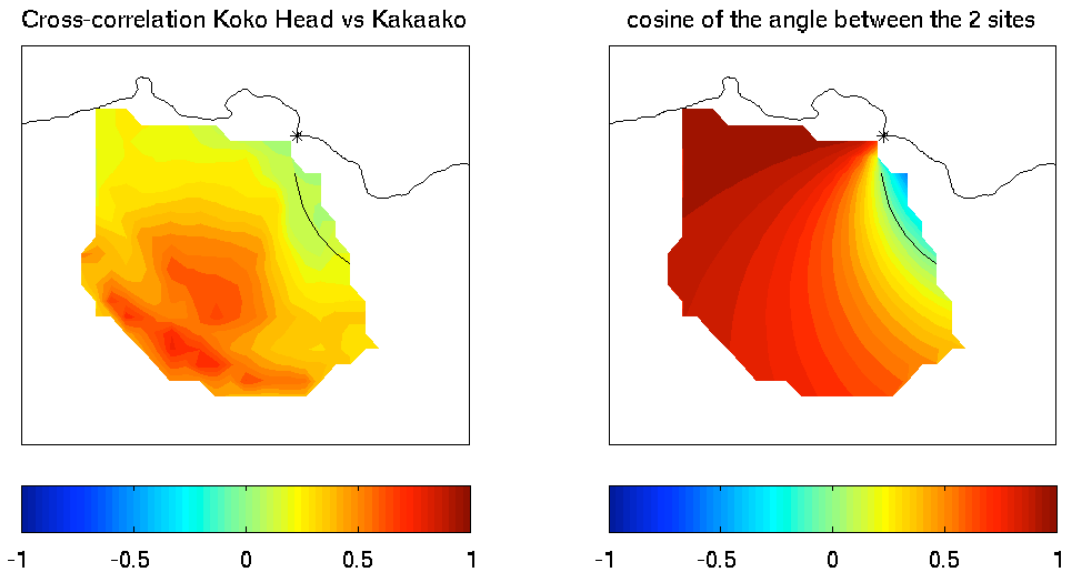

Figure 2.5: Cross correlation between Koko Head and Kaka'ako radial current when data from both sites was available (left) and the cosine of the angle between the sites (right). The circle where the angle between the two sites is 90 degrees is show in black.

Chapter 3

Low Frequency Motions

3.1 Introduction

Over eleven months of HFR radial surface current observations from Koko Head reveal large scale current reversals through the Ka'iwi Channel. Vector currents were inferred from the radial current record by imposing non-divergence and no flow through the coast. The most dominant and persistent feature apparent in the observations is the jet-like flow through the deeper Ka'iwi Channel, bordered by Oahu to the north and Penguin Bank to the south. Elevated levels of strain and vorticity are associated with the edges of the area of enhanced flow through the Ka'iwi Channel. Displacement patterns of simulated drifters highlight areas susceptible to high rates of separation attributable to strain, trends relevant to maritime search and rescue, pollution response and future drifter deployments.

In this chapter analytical techniques for cleaning, interpolating and filtering radial currents then inferring vector currents are described. Assessment of the non-divergent assumption used to infer vector currents, statistical properties and flow features apparent in the low frequency record are presented.

3.2 Quality Control and Vector Generation

Minor quality control and manipulation prior to analysis of the record was required. Irregularities in time spacing were omitted if the time of observation was greater than five minutes different than the fifteen minute time steps. Observations that exceeded variance and accuracy threshold values of .04 m/s or .25 m/s as estimated by the WERA software were rejected. Data returned over land and beyond the 50% spatial coverage contour was masked. Following these minor cleaning steps, basic statistics such as median and standard deviation were computed. Annual and seasonal median radial currents are presented in figures 3.1 and 3.7. Annual and seasonal standard

deviation of radial currents are shown in figures 3.2 and 3.8.

A comparison was made to the HFR observations during the Hawaiian Ocean Mixing Experiment (HOME) deployment as an attempt to quantify how non-divergent the subinertial flow is. Figure 3.3 shows the power spectra of divergence and vorticity calculated from detided vector currents as described by Chavanne et al., 2010 B. Magnitude of the vorticity power spectra dominates divergence at time scales much below the inertial frequency. At time scales over ten days divergence is nearly an order of magnitude less than vorticity. Therefore, divergence at longer time scales is insignificant.

Solving the partial derivatives of a two-dimensional stream function provides the velocity components of a non-divergent flow. In cartesian coordinates, zonal and meridional components of the current are defined as:

$$u = \frac{\partial \Psi}{\partial y} \qquad v = -\frac{\partial \Psi}{\partial x} \tag{3.1}$$

where Ψ is the two dimensional stream function. Adapting this expression for polar coordinates yields:

$$u_r = \frac{1}{r}\frac{\partial \Psi}{\partial \theta} \qquad u_\theta = -\frac{\partial \Psi}{\partial r} \tag{3.2}$$

where r is range, θ is azimuth, u_r is radial current and u_θ is azimuthal current. With u_r known from the radial current observations, the stream function can be solved by rearranging and integrating the first equation of 3.2.

$$\Psi = \int_{\theta_0}^{\theta_f} r\, u_r\, d\theta \tag{3.3}$$

Vector currents were inferred by evaluating expression 3.3 in a counter-clockwise direction where θ_f= 160°T. A no-flow boundary condition was enforced across the coast which was approximated as the

constant bearing line $\theta_0 = 280°T$ from Koko Head. Grid points values over land were held to zero. Azimuthal currents (u_θ) were solved as shown in the second equation from 3.2. Geostrophic height (η) is the stream function scaled by the ratio of the inertial frequency (f) and gravitational acceleration (g):

$$\eta = \frac{f}{g}\Psi \qquad 3.4$$

Polar vectors (u_r and u_θ) were rotated to cartesian coordinates to generate vector currents for plotting. Vector currents were generated using these assumptions from the monthly, seasonal and annual median radial currents. Inferred annual and seasonal vector currents are presented in figures 3.4 and 3.9. Spatial averages of 30 day median inferred vector currents over Penguin Bank, the near shore shelf south of O'ahu and the through the Ka'iwi Channel where the areas were bound by the 100 m depth contour are shown in figure 3.12.

With inferred vector currents now available, vorticity is easily computed. In polar coordinates evaluate the vertical component of the curl:

$$(\nabla \times u)\hat{e}_z = \frac{1}{r}\left(\frac{\partial (r u_\theta)}{\partial r} - \frac{\partial u_r}{\partial \theta}\right)\hat{e}_z = \zeta \qquad 3.5$$

Inferred annual and seasonal median vorticity profiles are plotted in figures 3.5 and 3.10.

Lagrangian properties of the low frequency flow can be also investigated following the generation of vector currents. Futch (2009) used Lyapunov exponents or Lagrangian rates of separation (RoS) to investigate HFR data collected from west of Oahu. A similar variable, instantaneous RoS, was defined using the components of the velocity gradient tensor where it was broken down into three main components: an antisymmetric part representing vorticity, and a symmetric part which is comprised of an isotropic divergence portion and a non-divergent strain portion. While divergence is unavailable from one radial alone and has been set to zero to generate vector currents, the remaining strain component can be evaluated. A parallel derivation to Futch's

strain in polar coordinates is provided in Appendix B.

The following expression was computed to evaluate the strain component (σ) of the velocity gradient tensor from annual and seasonal median currents (figures 3.6 and 3.11).

$$\sigma = \sqrt{\left(\frac{\partial u_r}{\partial r} - \frac{1}{r}\left(\frac{\partial u_\theta}{\partial \theta} + u_r\right)\right)^2 + \left(\frac{\partial u_\theta}{\partial r} + \frac{1}{r}\left(\frac{\partial u_r}{\partial \theta} - u_\theta\right)\right)^2} \qquad 3.6$$

Evaluating strain helps identify areas with elevated dispersion rates, trends relevant to search and rescue operations or drifter deployments. To portray the impact of elevated strain, drift from the static annual median was computed for fifteen minute time steps over 1.5 days by integrating the following expression:

$$\int \frac{dx}{dt}\,dt = \int u_0(x_0)\,dt \qquad 3.7$$

Where x represents space, t is time and u is velocity. Evaluation of the integral provides the change in position from the bi-linear interpolation of velocity at the drifters previous position. Examples of drifters introduced in square patterns placed in areas of varying strain are shown in figure 3.13.

3.3 Numerical Analysis

A least-squares fit of the solar annual (SA) tidal constituent was conducted on the cleaned radial current data using T-Tide (Pawlowicz et al., 2002). The astronomical forcing of SA is very small so changes actually observed at the annual period are likely attributed to atmospheric forcing. The annual wind cycle near Hawaii includes a strengthening of the trade winds through the summer months and slackened or Kona winds in the winter. Using the phase and amplitude characteristics output from T-Tide, radial currents were computed for each quarter cycle then vector currents were inferred using the same process described in section 3.2. Finally, the inferred median annual vector current was added to the inferred vector currents for each quarter cycle. The sum of these two quantities represents the inferred seasonal mesoscale currents (figure 3.14).

Filtering to investigate specific ranges of the frequency spectrum was used throughout this study. Due to the irregularity in data gaps in space and time, careful interpolation was first required. The primary interpolation sequence capitalized on the dominate tidal signal apparent in the record. If less than two days of data was missing across an 8 day interval, interpolation using the least squares fit of the M2, K1 and inertial frequencies, a constant offset and a linear trend was completed. The process was repeated until no further gaps in data satisfied the interpolation criterion. This interpolation sequence filled all but longer time gaps that were the result of a hardware failures greater than 2 days. These final longer gaps were linearly interpolated.

Primarily filtering for this study was accomplished using lanczos filters due to their great phase stability. The lanczos filter routine is a convolution of the record with a sinc-like window and is very effective at suppressing the signals beyond the cut off period.

To show the spatial distribution of radial and inferred vector mesoscale energy densities, $\log_{10}$ average power spectra density values for periods between 7 and 90 days are plotted in space (figures 3.15 and 3.16).

To mitigate the impact of outliers present in the record, robust estimators were employed to evaluate the standard error estimate. Quantile spread (S) was explicitly evaluated by averaging quantile values of .158 and .842. Degrees of freedom (n) were estimated using the auto-correlation function of the record decimated to one day sampling.

$$Standard\ Error = \frac{S}{\sqrt{n}} \tag{3.8}$$

Signal to noise ratio was computed as:

$$SNR = \frac{Median}{Standard\ Error} \tag{3.9}$$

Standard error and signal to noise ratio are plotted in figures 3.17 and 3.18. The black band in figure

3.18 is due to the area of nearly zero radial current in the annual median.

Spatial spectra was computed using the entirety of the radial record and is co-plotted with theoretical slopes for internal and surface quasi-geostrophic theory and as found by Andrews and Hoskins in figure 3.20. The slope is exceptionally straight and very similar to the -8/3 slope.

3.4 Discussion

Annual median radial current shows an enhanced outward flowing area confined between the shelves of south O'ahu and Penguin Bank with weaker outward flow along the nearshore area south of Oahu. Flow is towards the site south and east of Penguin Bank. Similarly, the supporting annual inferred vector plot show enhanced westward flow in the deeper channel.

The salient feature in the annual median vector current plot is the region of cyclonic flow just west of Penguin Bank. Considering atmospheric forcing, the trade winds are obstructed Haleakala or other mountainous areas on Maui, creating positive wind-stress curl to the northern and negative to the southern extremes of the volcanos. This 'Penguin Bank Cyclone' lies in an area of positive wind stress curl (Chavanne et al., 2010c) which would set up upward Ekman pumping causing the doming seen in the geostrophic height contours of figures 3.4 and 3.9.

The dominant region of elevated variability in the annual and seasonal standard deviation plots are between Koko Head and Diamond Head. This pattern is a manifestation of the coastal boundary and is also apparent in the radial current mesoscale kinetic energy density plot (figure 3.15). Coast-normal currents are inhibited by the boundary so are zero compared to alongshore currents which flow freely along the coast. The minimum in standard deviation occur along Oahu's south shore where flow is predominantly westerly through the year with a short and weak reversal between January and March 2010. Penguin Bank shelf area also exhibits relatively low levels of variability while the adjacent Ka'iwi Channel jet and shallow crest of Penguin Bank shows enhanced variability.

Seasonal median radial and vector plots show Kaiwi Channel flow through as maximum in the

summer months, weakening between October and December and reversing between January and March. Spatially averaged monthly median feather plot shows the large scale current inversion in the Ka'iwi channel. Flow along the south shore is consistently weaker, but in the same direction is the Ka'iwi Channel. Patterns across Penguin Bank closely mimics the Ka'iwi Channel.

Seasonal mesoscale vector plots clearly show the Penguin Bank Cyclone. Coincident with the annual trade wind cycle, the cyclonic rotation is most significant in the summer months (April – June) and is hardly detectable in the winter months (October – December). Elevated regions of mesoscale eddy energy density also occur in this same apparent eddy generating site. Mesoscale eddy energy density is low along the south shore and over the shallows of Penguin Bank. Mesoscale features are assumed to be on the order of the thermocline deep, or a few hundred meters around Hawaii, so are inhibited from crossing these shallow features or moving close to shore. Variability of the channel jet also contributes to the mesoscale eddy high energy density in the Ka'iwi Channel.

Annual median vorticity and strain highlight the north and south borders of the Ka'iwi Channel where regions of negative/positive vorticity and elevated strain are generated. The central region of the channel is irrotational with lower strain. Seasonal vorticity and strain mimics the temporal variation of the Ka'iwi Channel jet. During the summer months, when flow to the west is greatest, vorticity and strain along the channel boundaries are elevated. In the winter months when flow weakens and inverts, vorticity and strain are weaker and more variable.

Simulated drifters based on annual median flow show the effects of varying strain. The square of drifters initiated in the jet show a large displacement, but little relative change with respect to one another. Drifters placed along the higher strain regions show larger relative changes, most vividly in the near shore area. The effect of strain is germane to Coast Guard search and rescue or pollution response missions. Areas of higher strain could further disperse survivors, pollutants or debris fields creating a larger search area to be covered by operational assets.

The majority of the discussion of this chapter rests upon the validity of the non-divergent assumption imposed to infer vector currents. Primary contributing processes to the non-divergent component of the flow include geostrophic currents and to a lesser extent, non-divergent Ekman flow. Revisiting the approximations upon which geostrophic balance is based, horizontal motions result from the balance of pressure gradient and Coriolis forces, friction is negligible and flow is independent of time. Geostrophic currents are themselves non-divergent. Explicitly:

$$v = \frac{1}{\rho f}\frac{\partial p}{\partial x} \qquad u = \frac{-1}{\rho f}\frac{\partial p}{\partial y} \tag{3.10}$$

Taking divergence:

$$\nabla \cdot u = \frac{\partial u}{\partial x} + \frac{\partial v}{\partial y} = 0 \tag{3.11}$$

confirming that geostrophic currents are purely non-divergent.

Non-divergent Ekman flow is forced by divergent winds. Considering gyre-scale dynamics, mid-latitude westerlies and tropical trade winds set up atmospheric divergence due to the leftward rotation of the wind caused by the bottom atmospheric Ekman layer. The top Ekman layer excited in the surface ocean in this area experiences large scale convergence and downward Ekman pumping. The portion of Ekman transport that does not result in pumping is non-divergent and is presumably less significant than large scale geostrophic flow. Considering the observational environment south of Oahu, atmospheric divergence is not well resolved so quantification would be difficult. For the purpose of this study, the contribution of the non-divergent Ekman component is assumed to be insignificant leaving flow primarily geostrophic.

From the monthly median vector currents, the neglected time dependent $(\partial u/\partial t)$ and non-linear $(u \cdot \nabla u)$ terms were computed. They are co-plotted with Coriolis acceleration $(f \times u)$ in

figure 3.19. The RMS values over the domain of each of these terms are 6.78×10^{-9}, 7.55×10^{-8} and $6.02\times10^{-6} m^2/s^2$ respectively. This illustration shows the dominance of Coriolis acceleration, validating the geostrophic approximation used to infer vector currents. Comparison of these terms prior to imposing a condition of non-divergence would be valuable, but is not possible with radial currents.

3.5 Conclusions

Low frequency radial currents exhibited a large scale inversion of flow along Oahu's South shore through early 2010. By considering only sub-inertial time scales, inferred two dimensional flow dynamics were investigated. Geostrophic approximation is deemed to be accurate at time scales greater than a few days because divergence is less energetic in the subinertial frequency range. Inferred vector currents supported the large scale inversion apparent in the radial record and allow investigation of vorticity and strain. Vorticity and strain levels are significant near the steep slopes on either side of the Ka'iwi channel. Gyre-scale, wind-driven currents show of potentially significant vorticity generated by wind stress curl or lee eddy formation.

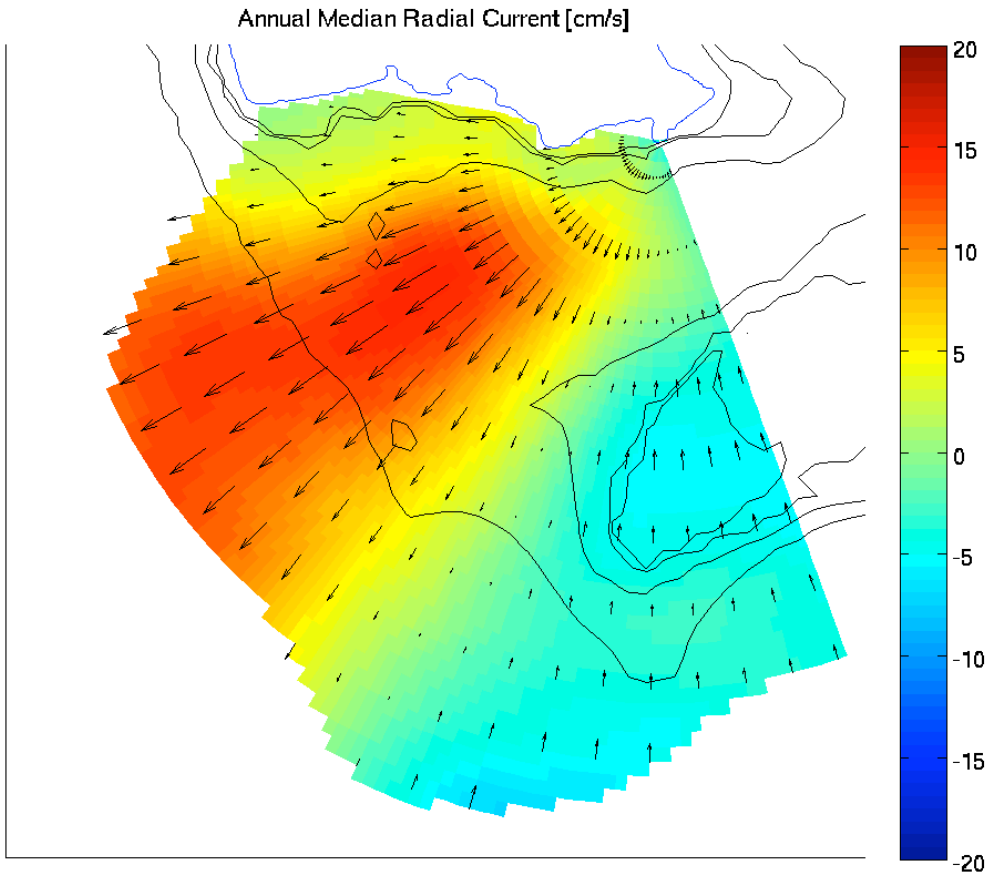

Figure 3.1: Annual median radial currents (cm/s). Bathymetric contours (1000, 500, 100 and 50 meters) in black.

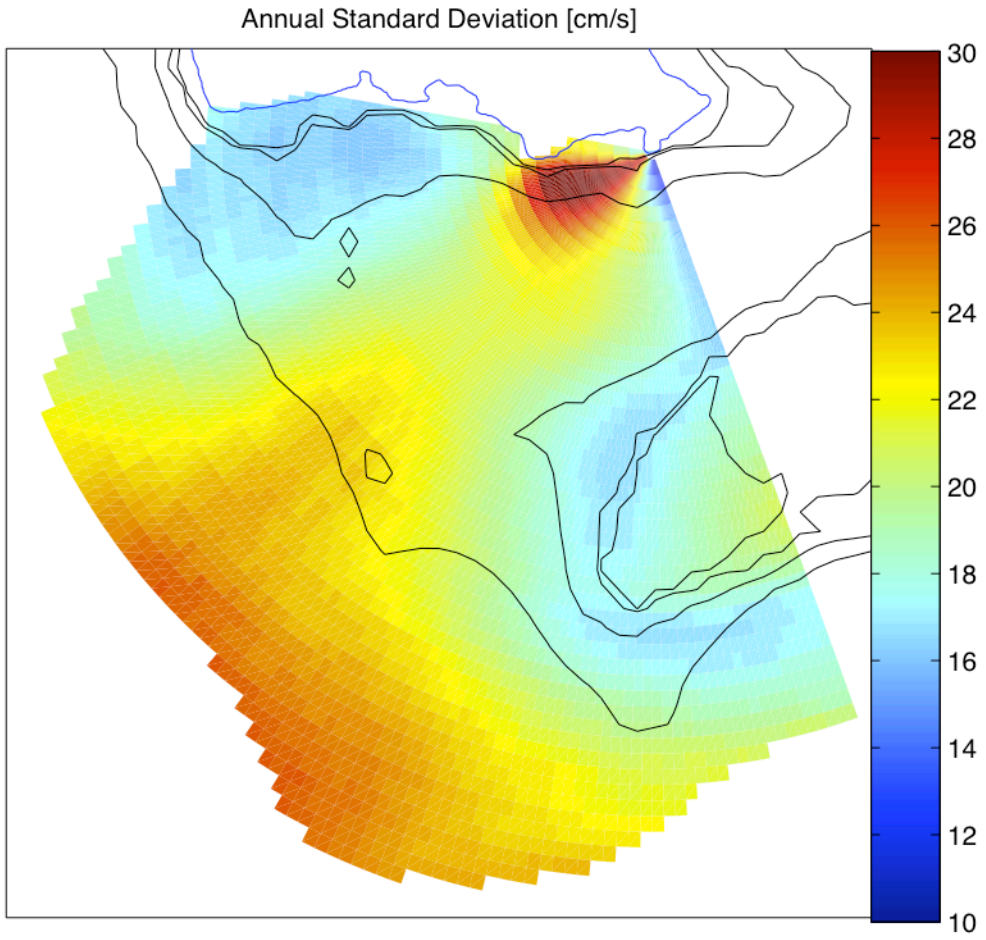

Figure 3.2: Annual standard deviation of radial currents (cm/s). Depth contours same as figure 3.1.

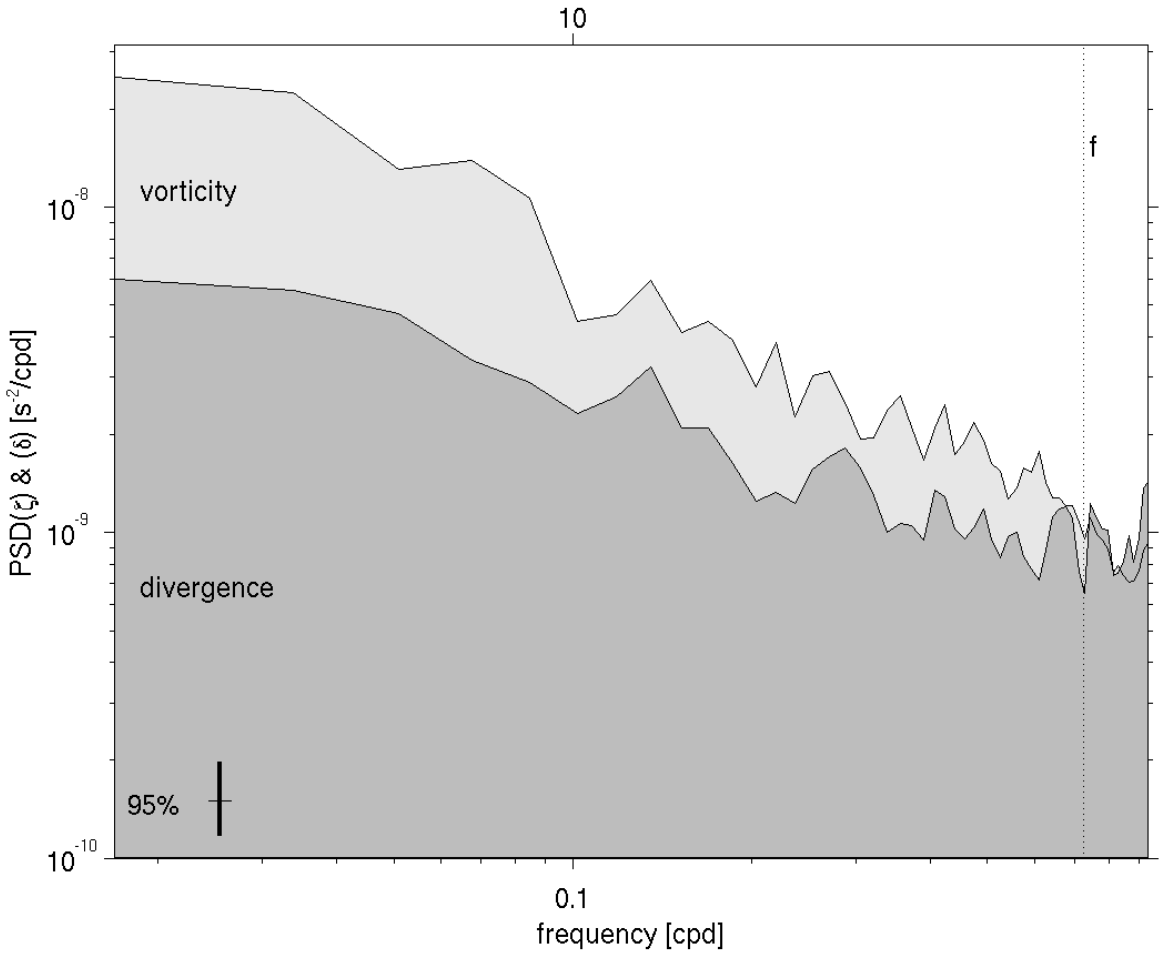

Figure 3.3: Spatially averaged vorticity and divergence power spectra for currents west of Oahu between 11 September and 9 November 2002. Vertical dotted line indicates the inertial frequency. (modified from Chavanne et al. 2010).

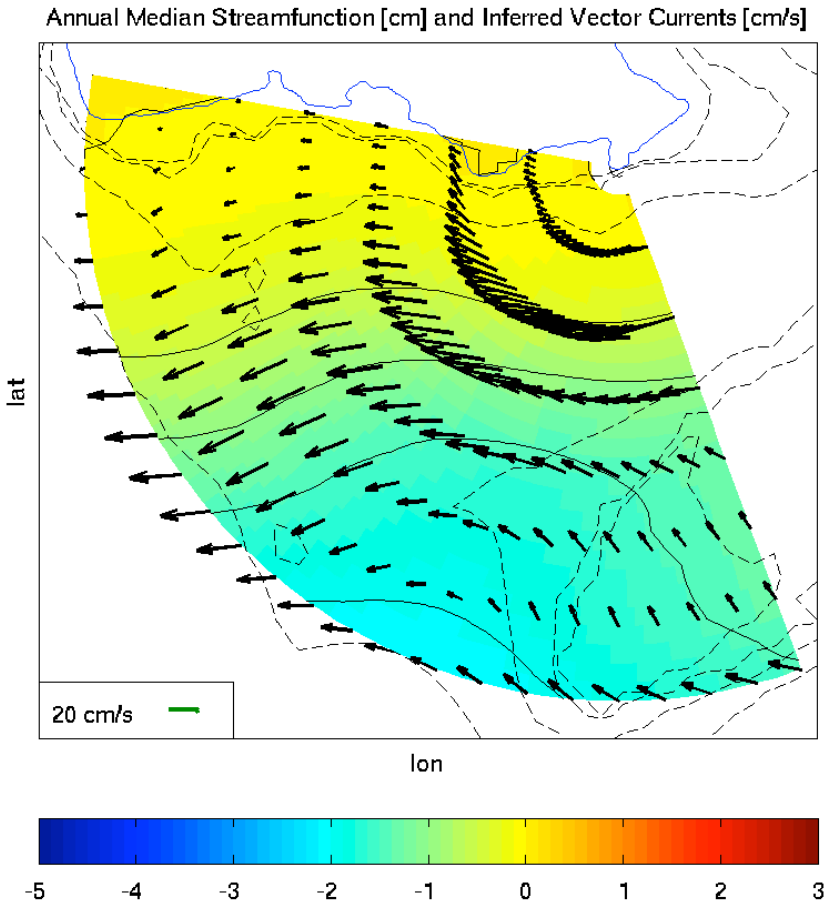

Figure 3.4: Inferred annual median vector currents (cm/s). Contours show inferred geostrophic height (cm) with contours every .5 cm. Bathymetric contours (1000, 500, 100 and 50 meters) shown with dashed black lines.

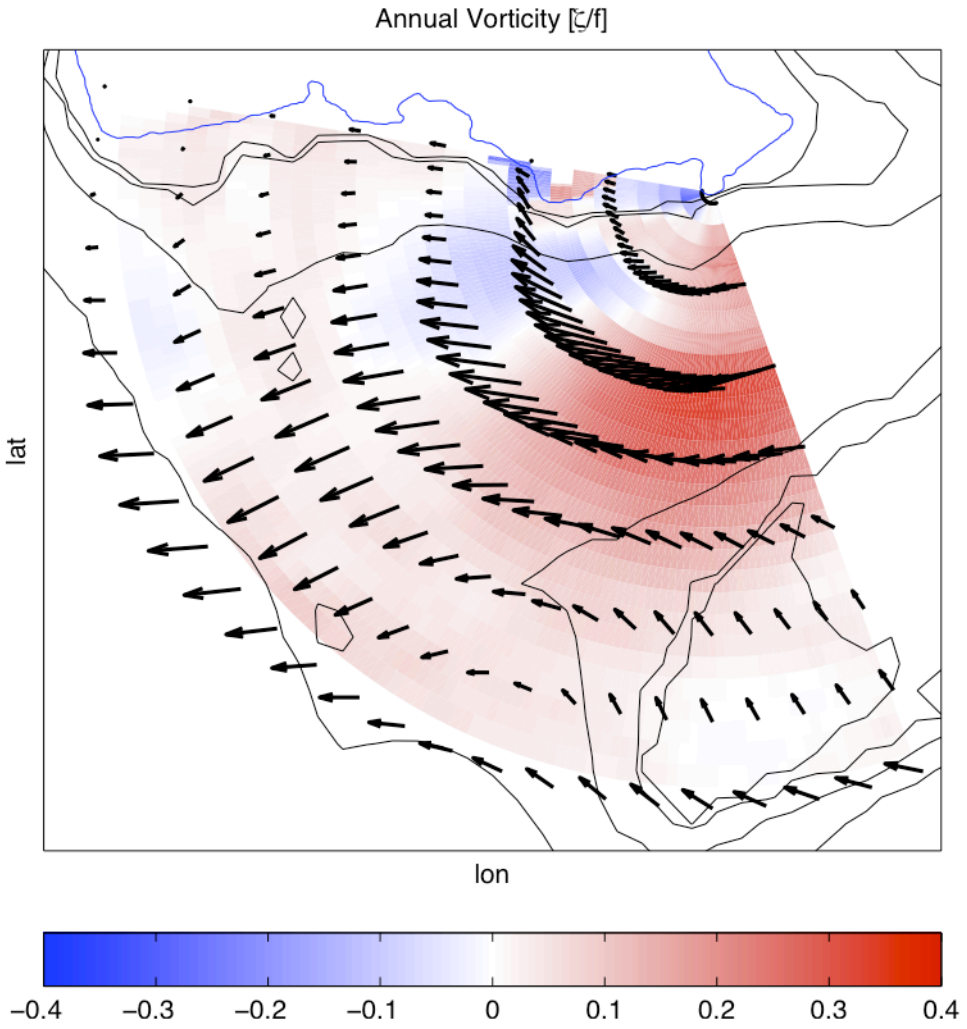

Figure 3.5: Annual median vorticity (ζ/f) from inferred annual median vector currents. Depth contours same a figure 3.1.

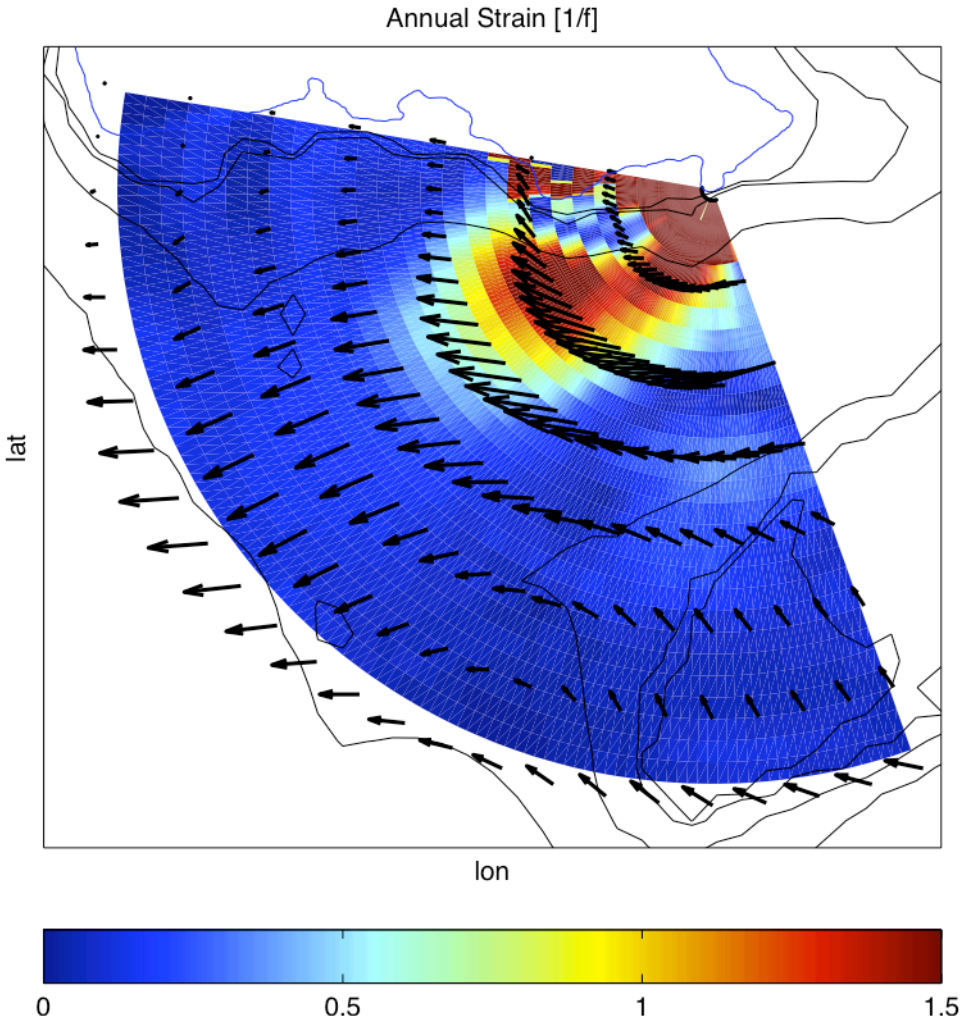

Figure 3.6: Annual non-divergent strain (1/f) from inferred annual median vector currents. Bathymetry profiles are same as figure 3.1.

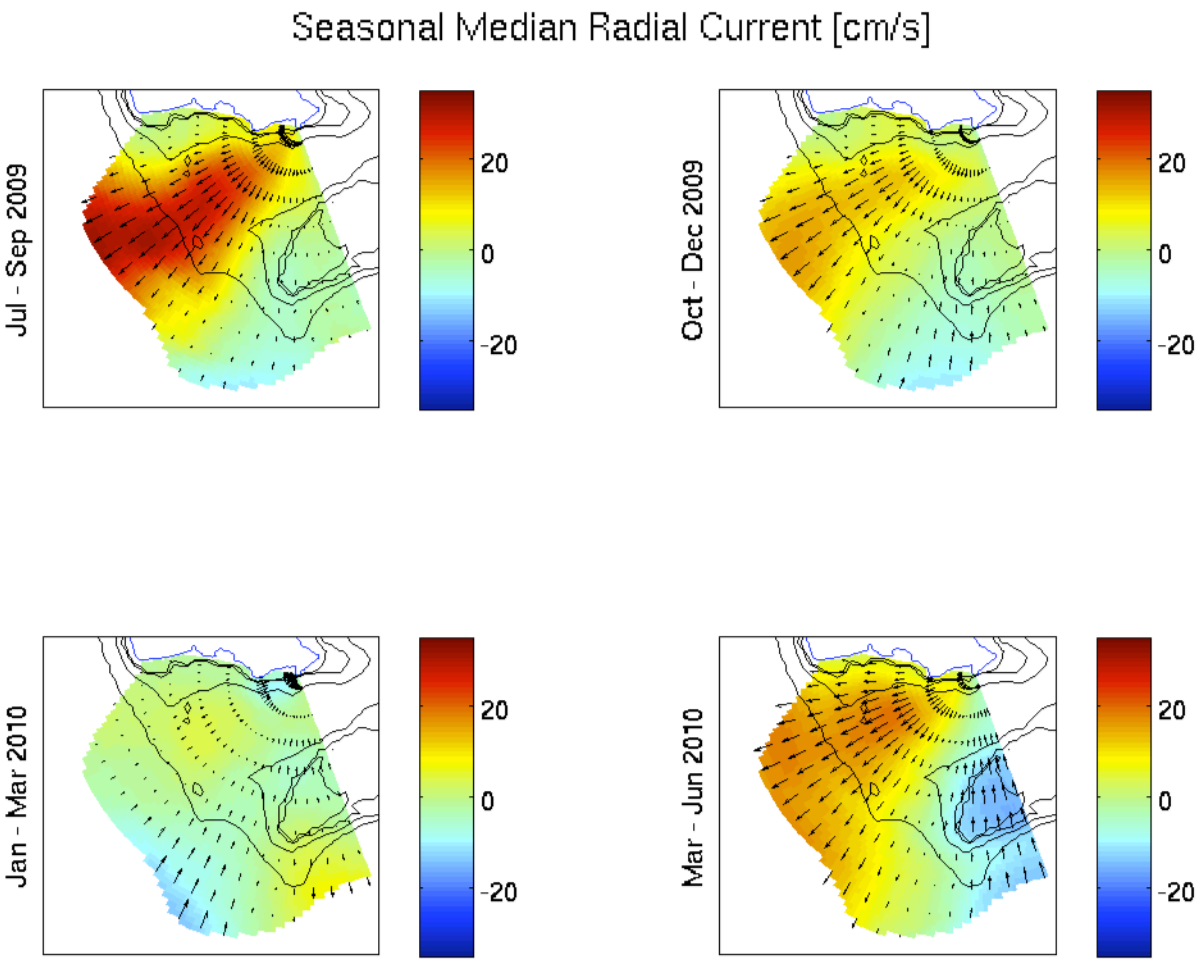

Figure 3.7: Seasonal median radial currents (cm/s). Depth contours same as figure 3.1.

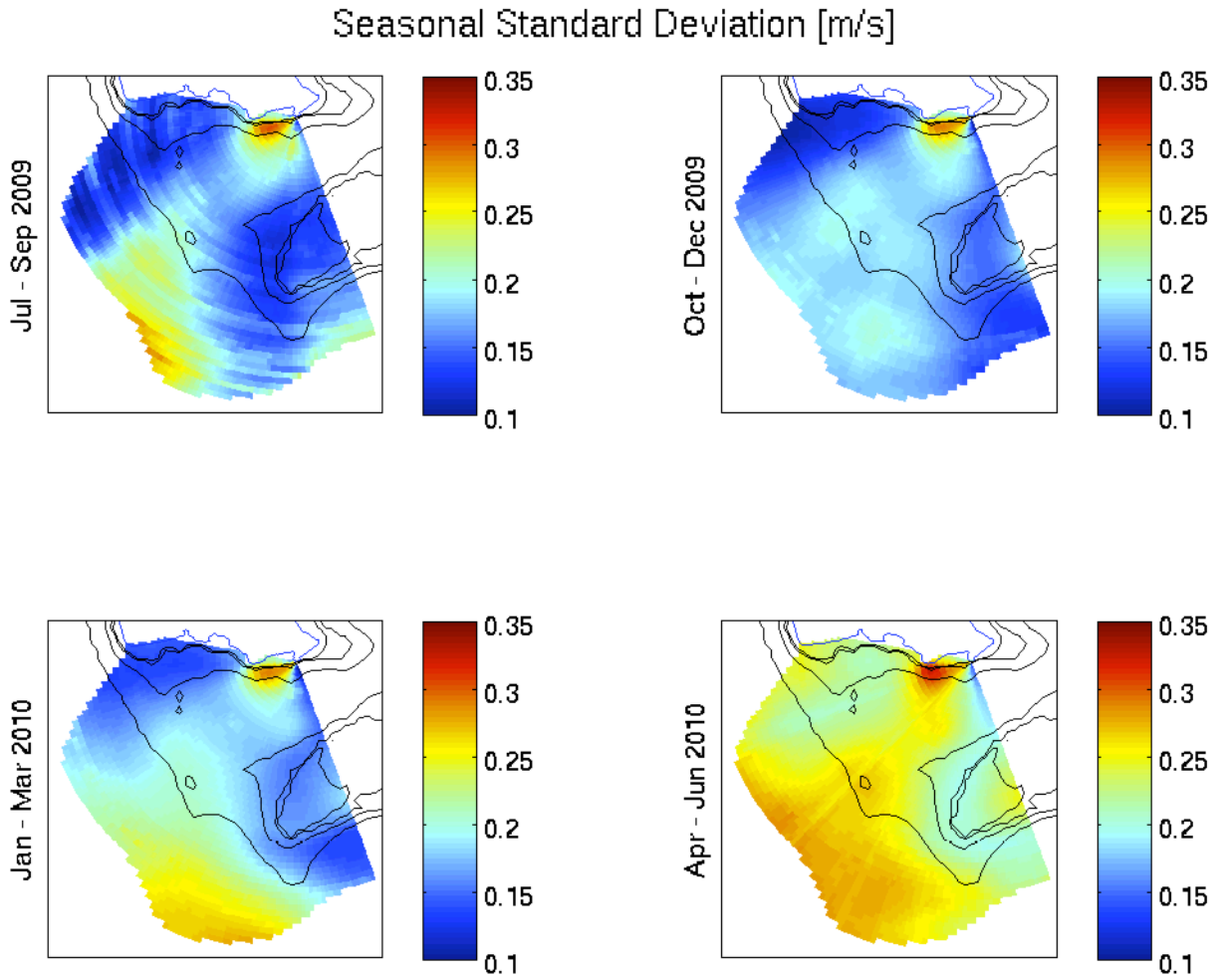

Figure 3.8: Seasonal standard deviation of radial currents (cm/s). Depth contours same as figure 3.1.

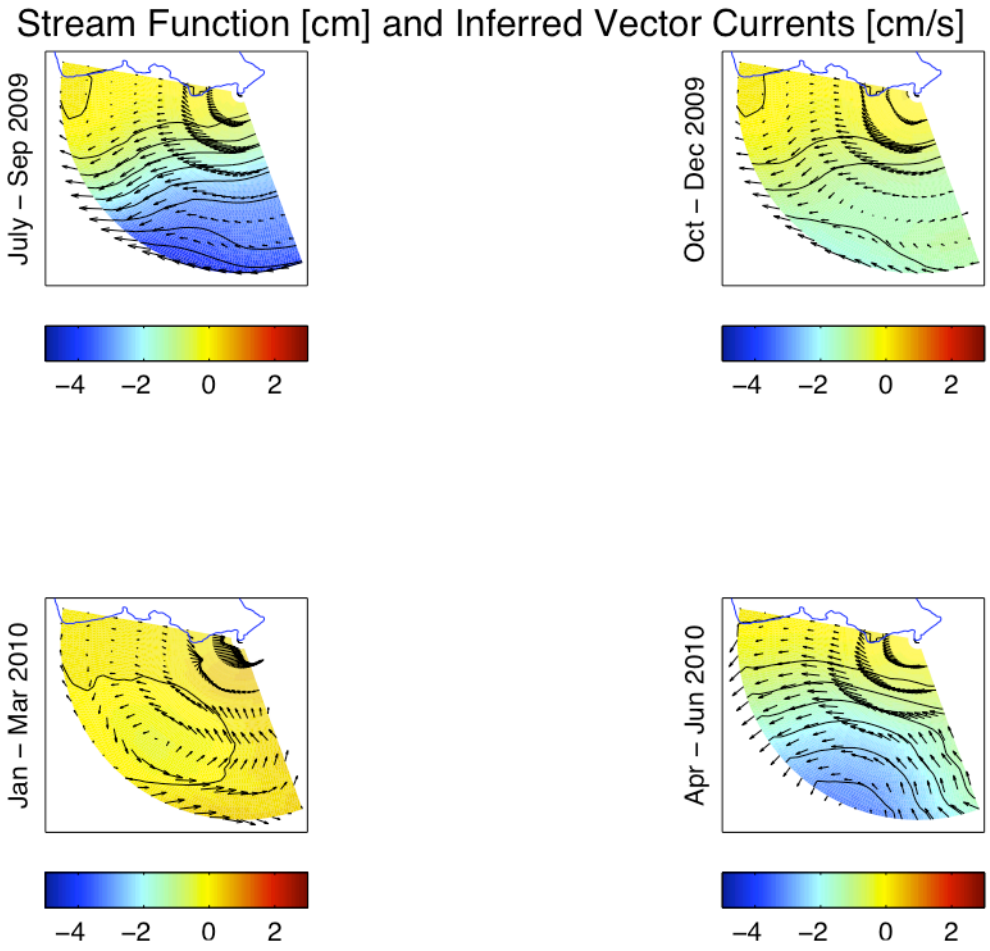

Figure 3.9: Seasonal inferred median vector currents (cm/s). Contours same as figure 3.4.

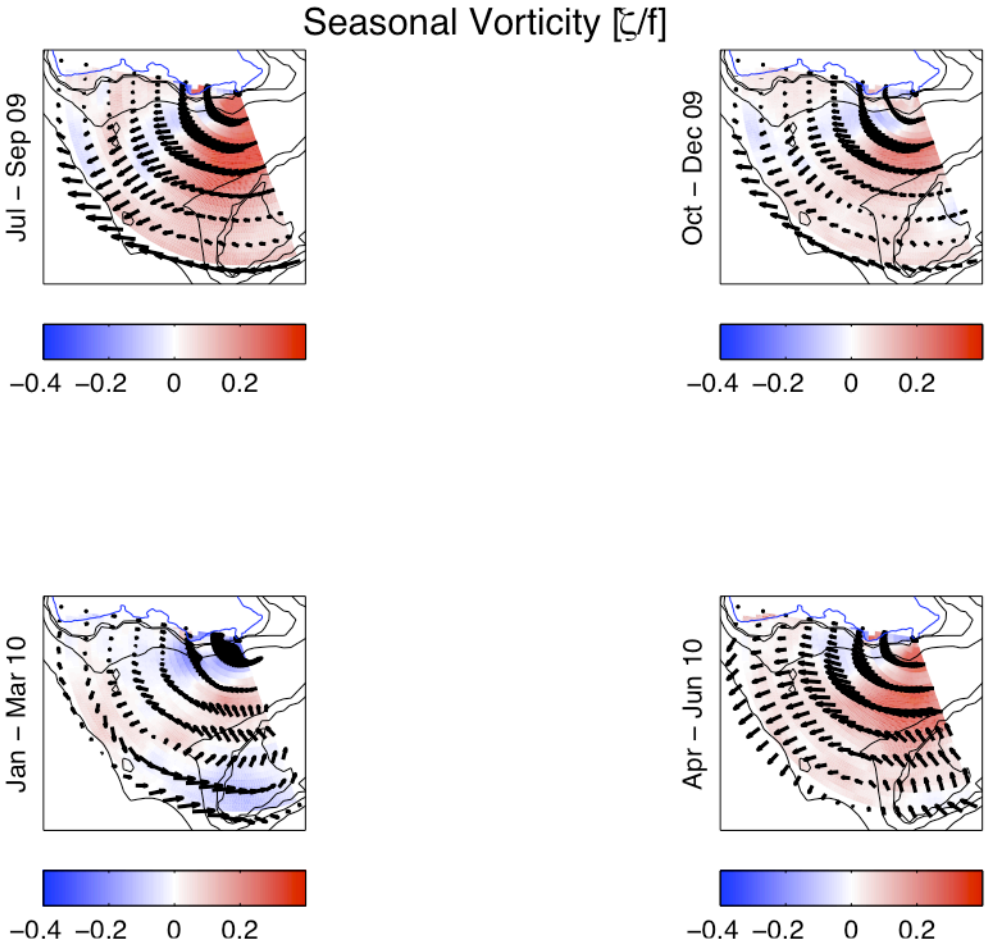

Figure 3.10: Seasonal median vorticity (ξ/f) from inferred annual seasonal vector currents. Depth contours same as figure 3.1.

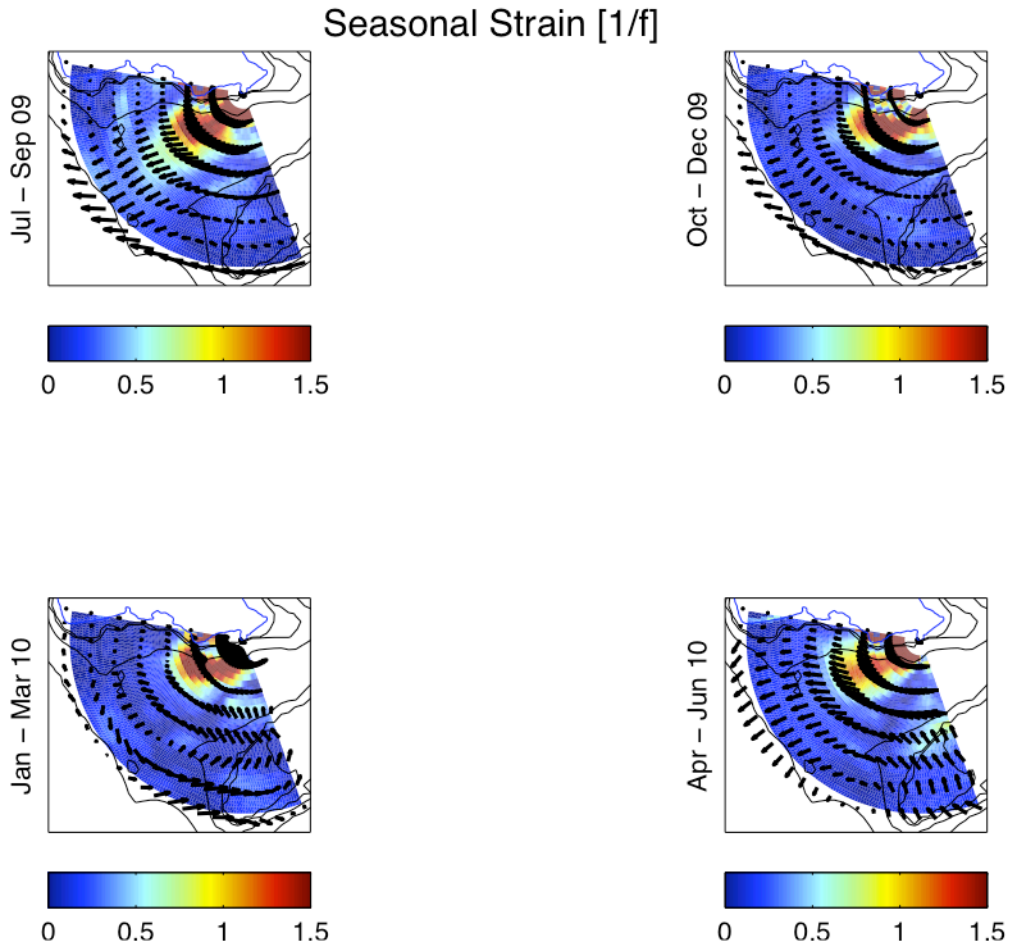

Figure 3.11: Seasonal non-divergent strain (1/f) from inferred seasonal median vector currents. Depth contours same as figure 3.1.

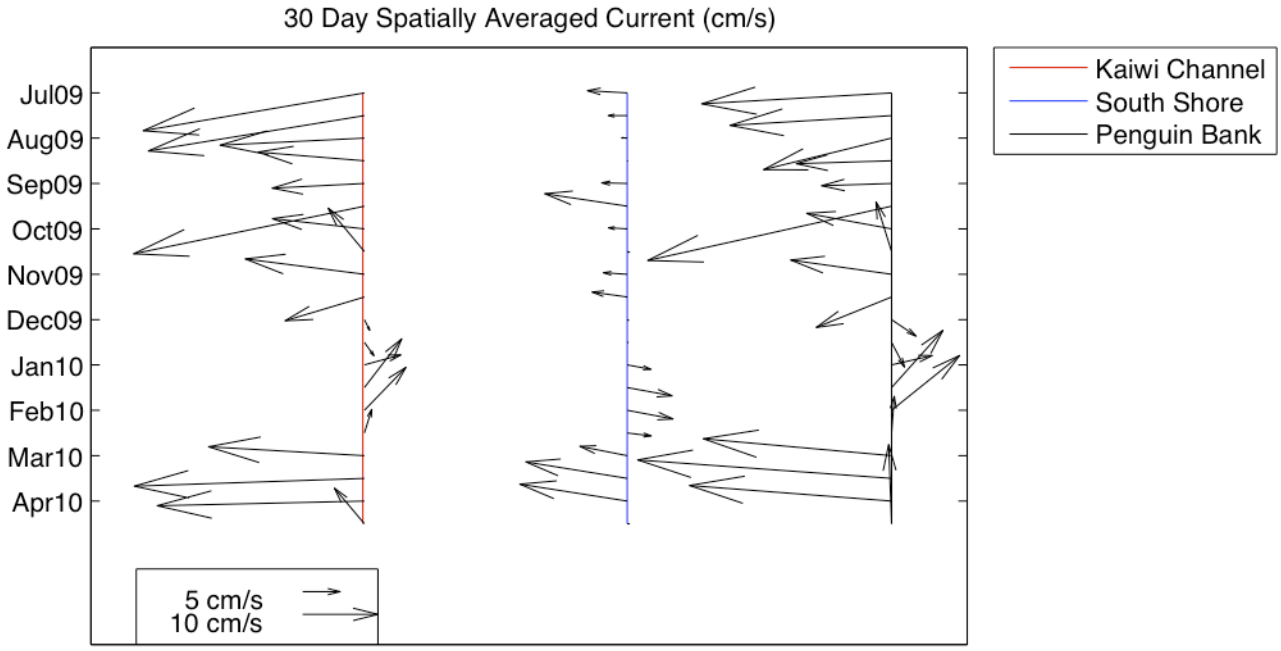

Figure 3.12: Spatially averaged 30-day inferred vector currents for areas bound by 100 m isobath along Oahu's south shore west from Diamond Head (red), less than 100 m isobath over Penguin Bank (blue) and deeper than 100 m isobath in Kaiwi Channel (black).

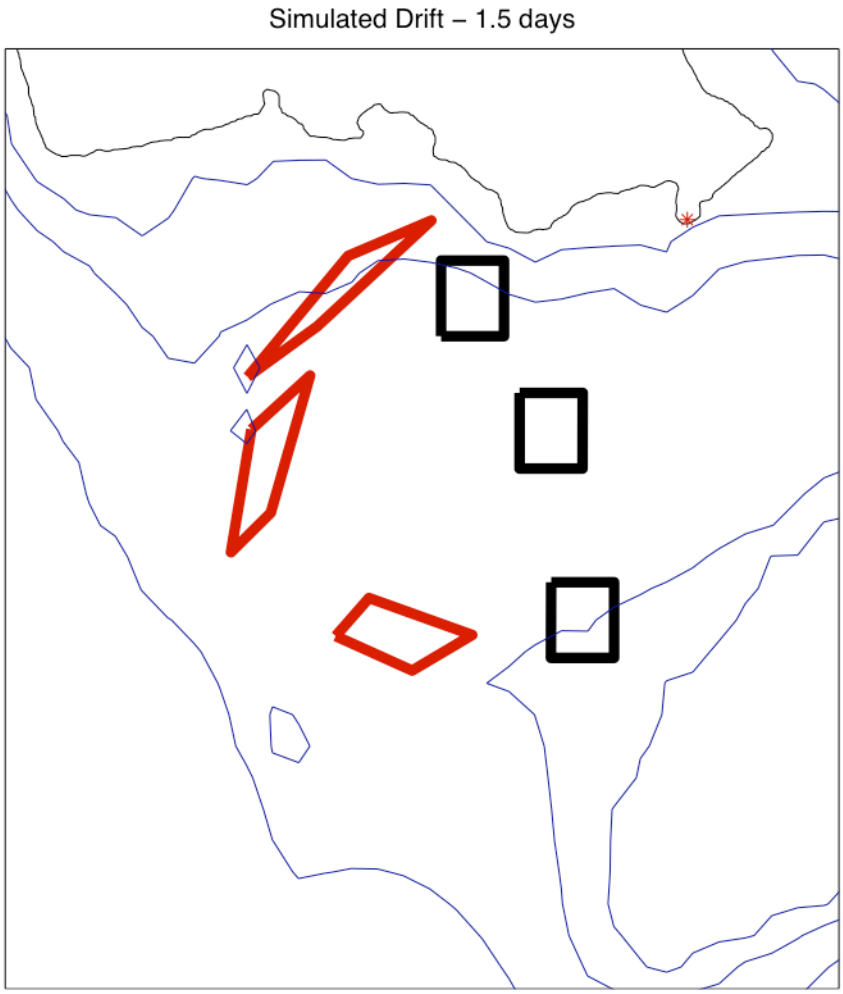

Figure 3.13: Simulated drifter deployment based on annual median flow. Initial location of ~4 km spaced drifter square shown at corners of black square. Location after 2 days of drift shown with corners of red polygon.

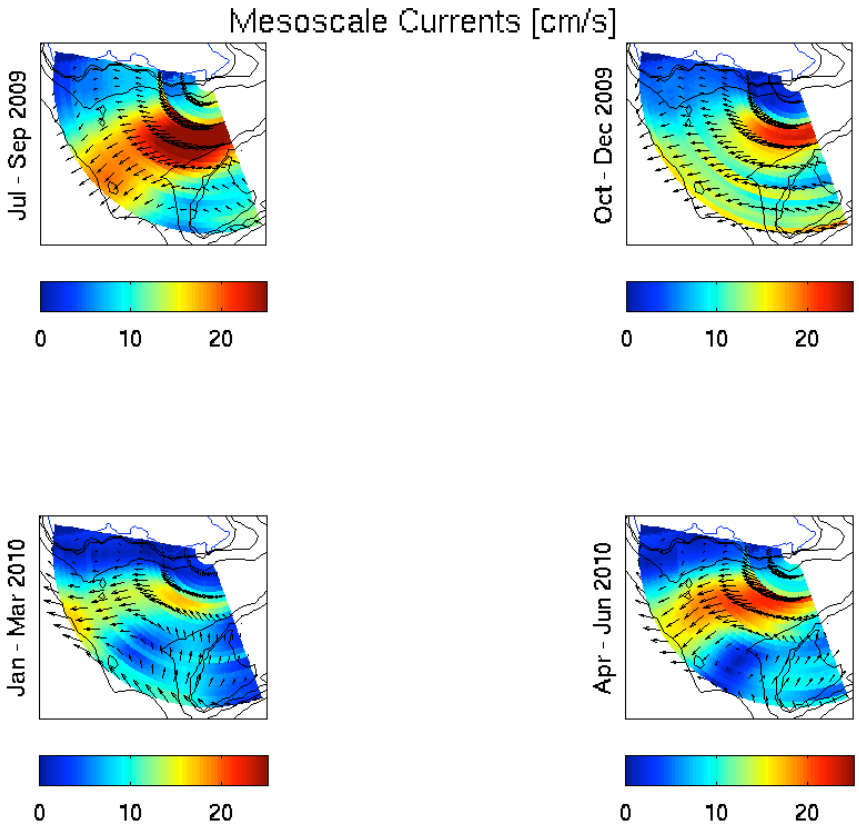

Figure 3.14: Seasonal mesoscale inferred vector currents (cm/s) constructed as the sum of inferred annual median vectors and the vector currents inferred from the phase and amplitude characteristics of a least-squares fit to the solar annual (SA) tidal constituent. Colors indicate magnitude of current in cm/s. Depth contours same as figure 3.1.

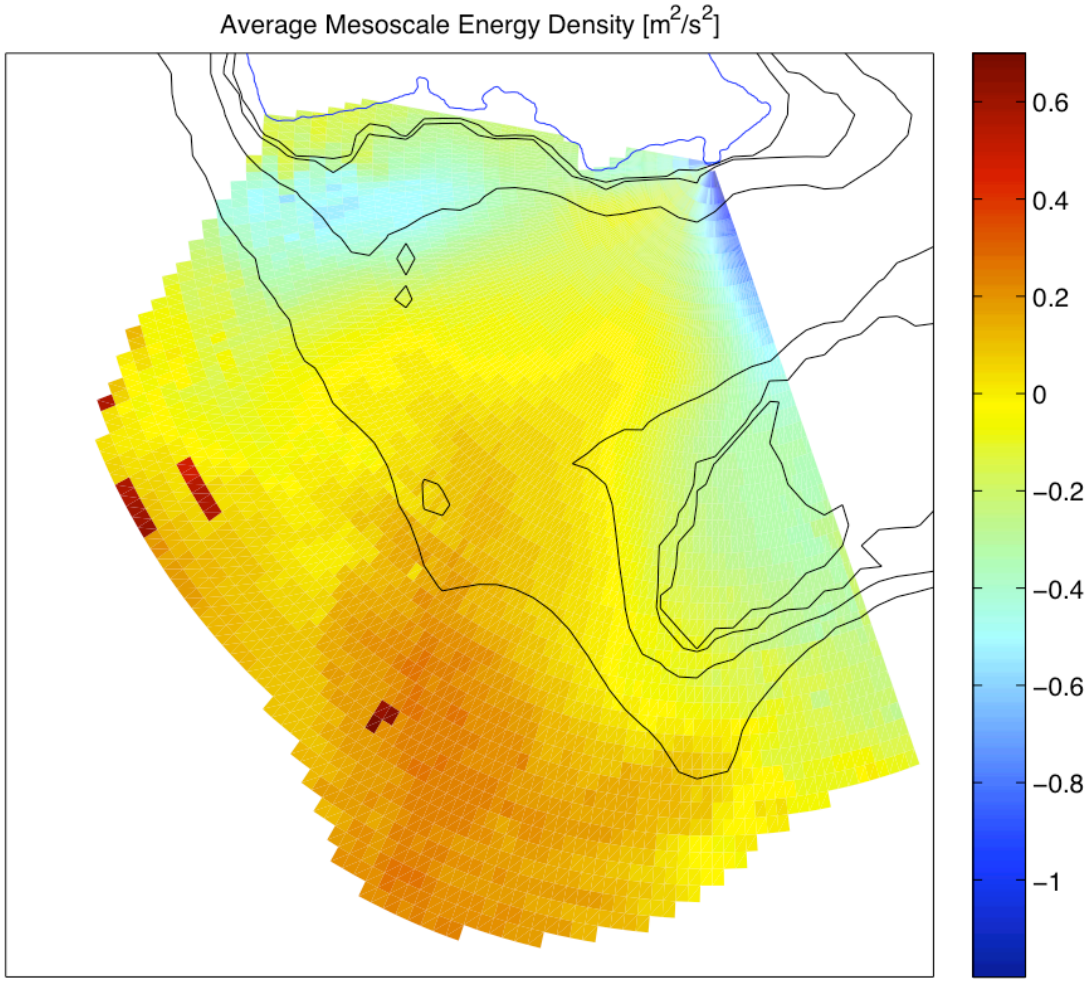

Figure 3.15: Log_{10} of average mesoscale energy density (m^2/s^2) from radial currents plotted in space. Frequency range defined as [1/90 days : 1/7 days].

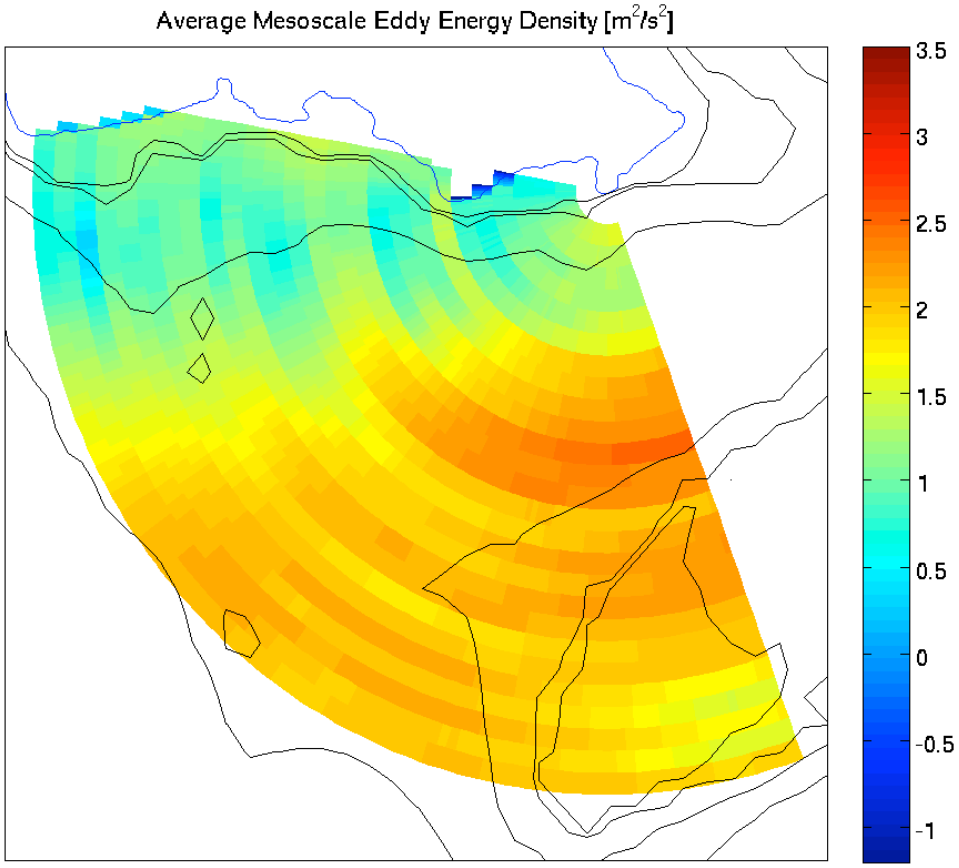

Figure 3.16: Log_{10} of mesoscale eddy energy density (m^2/s^2) from inferred vector currents plotted in space. Frequency range defined as [1/90 days : 1/7 days].

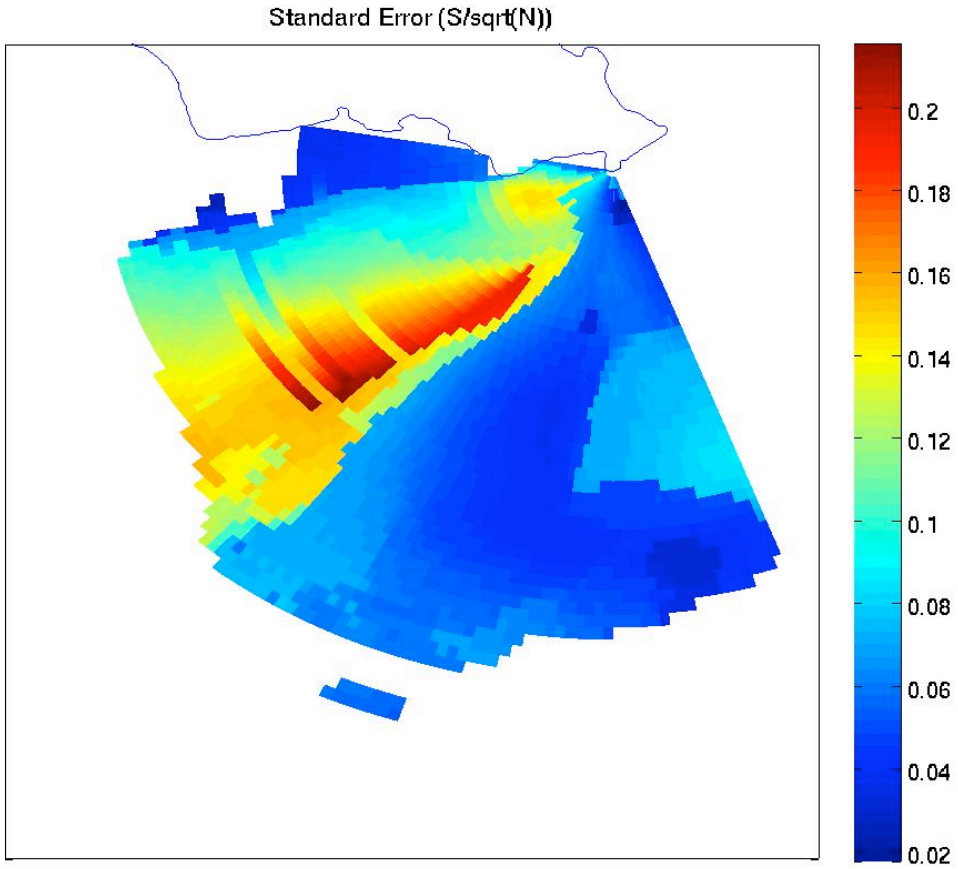

Figure 3.17: Standard error $\frac{S}{\sqrt{(\eta)}}$.

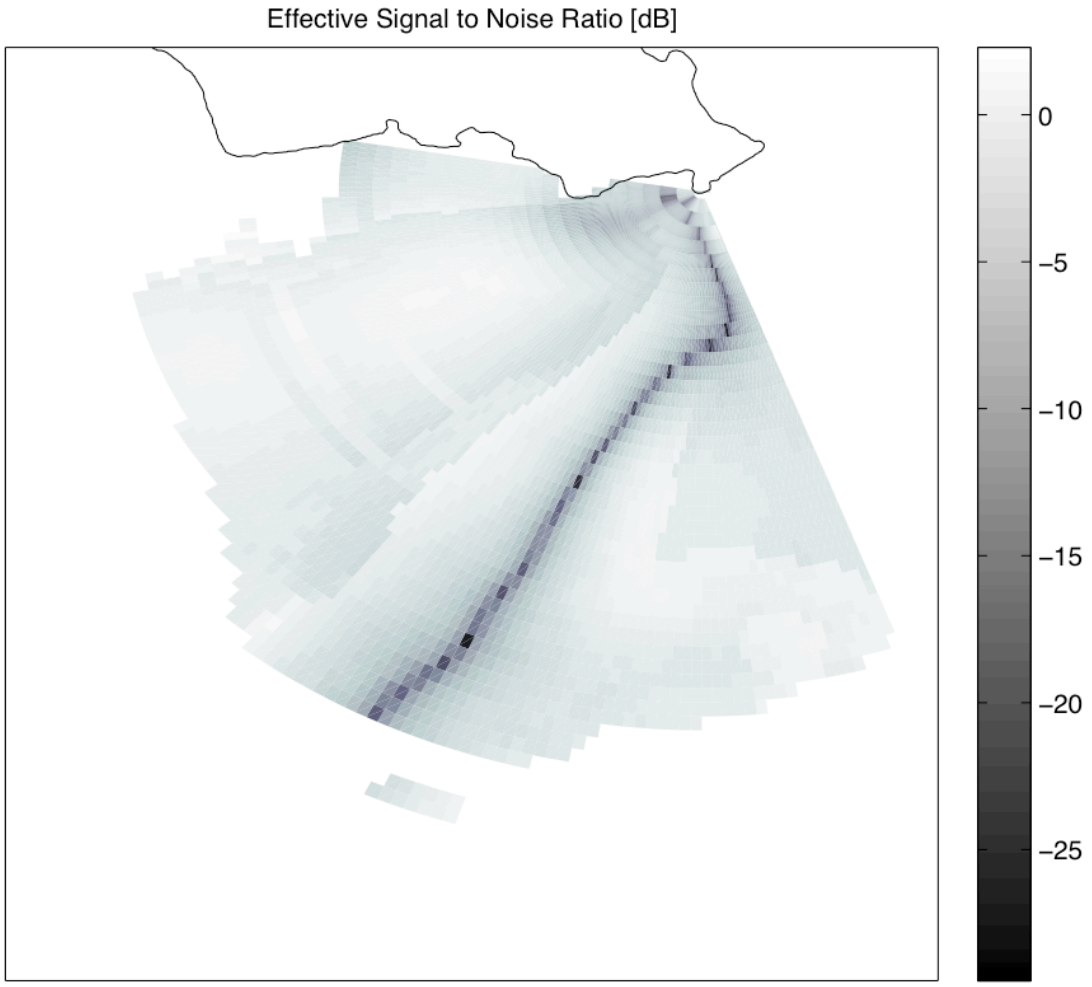

Figure 3.18: Signal to noise ratio estimate for median currents. $10\,log10\left|\frac{median}{standard\ error}\right|$.

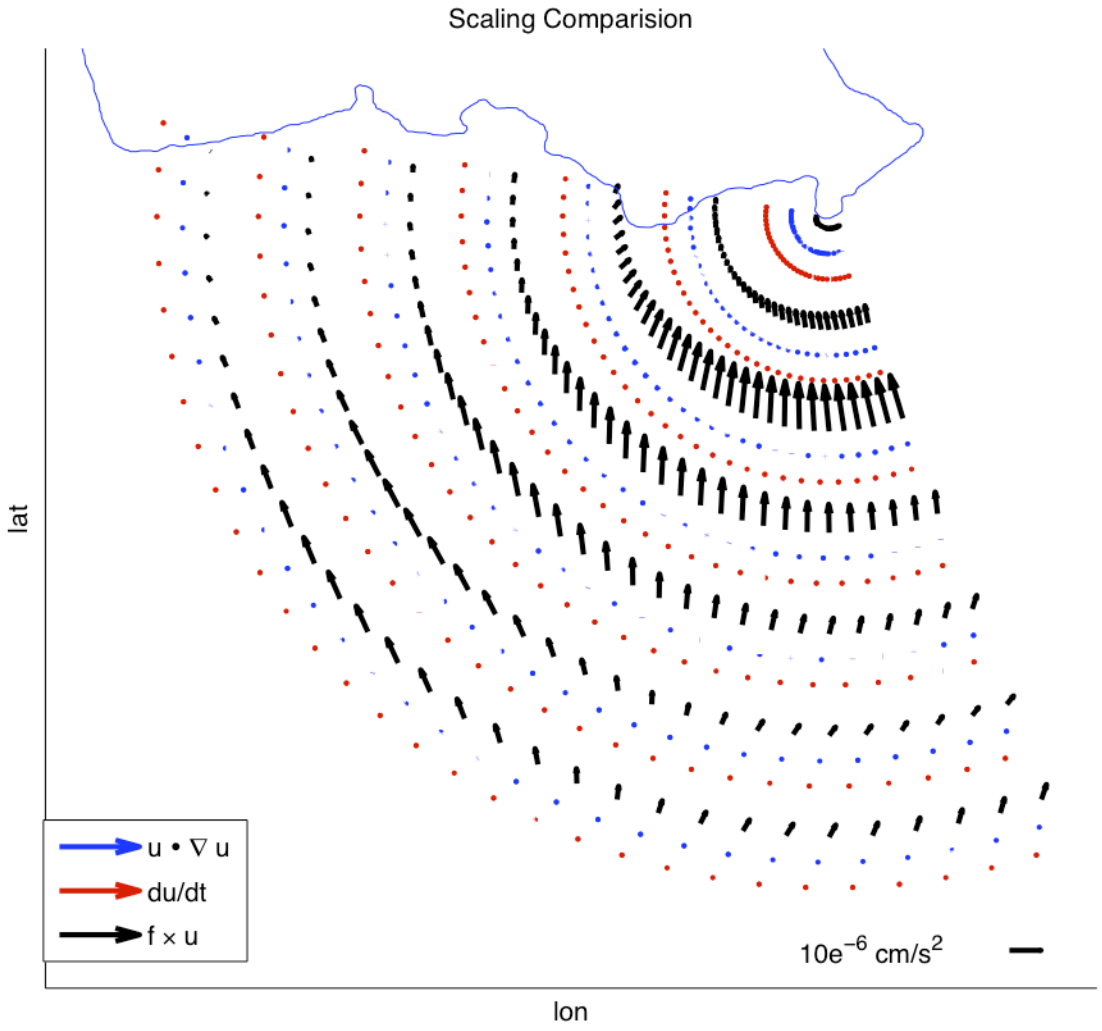

Figure 3.19: Time dependent $(\partial u/\partial t)$, non-linear $(u\cdot\nabla u)$, and Coriolis acceleration $(f\times u)$ terms (cm^2/s) co-plotted using monthly median vectors through deployment.

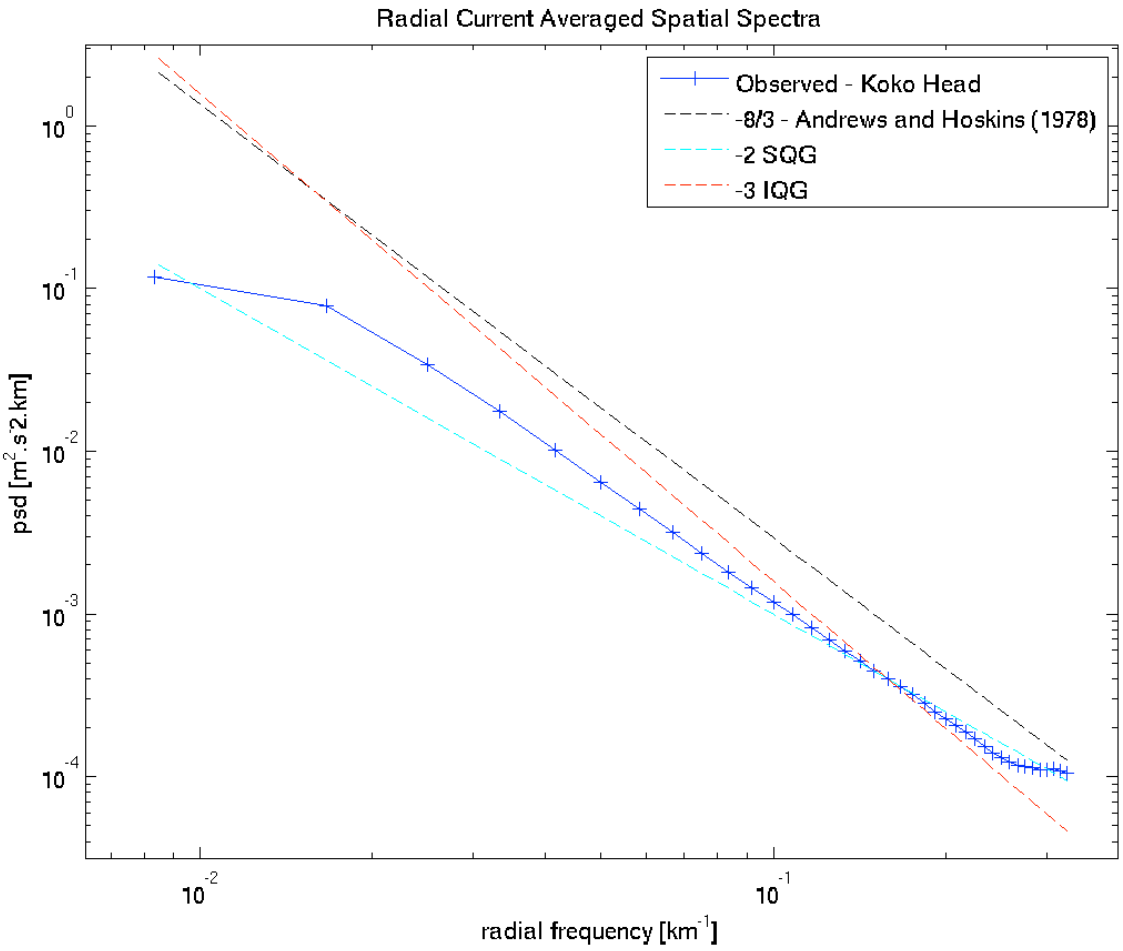

Figure 3.20: Spatial spectrum from Koko Head radial observations, -8/3 slope from Andrews and Hoskins, -2 slope from surface (SQG) and -3 slope from internal quasi-geostrophic (IQG) theory.

Chapter 4

Island Trapped Waves

4.1 Introduction

Minor spectral peaks at frequencies coincident with island trapped waves (ITW) are apparent in the power spectra of Koko Head radial currents, most notably in the de-tided record. Sub-inertial ITWs are a special case of coastally trapped waves occurring around a nearly circular island or shallow bathymetric feature. These kelvin-like waves are primarily excited and reinforced by local wind events but may be the result of remote atmospheric forcing or tsunamis. Their existence and influence have been documented around various island systems including Hawaii and Bermuda (Luther, 1985; Lumpkin, 1995; Brink, 1999).

At first order, ITW periods are dependent on island circumference and mode structure, taking longer to propagate around larger islands. The lowest mode ITW associated with O'ahu occurs very near the inertial frequency $(\Delta f \approx 1/.9\,hr)$. With inertial/near-inertial oscillations and ITWs sharing the same forcing mechanism, both are likely be most energetic following strong wind events making separation in frequency and time domains difficult.

In this chapter separation of the inertial and near-inertial ITW spectral peaks is attempted. EOF analysis of band passed HFR data reveals significant coherence with sea level records in the near-inertial to inertial frequency range. Coherence levels between Oahu sea level records were also significant within the same frequency range. An estimate of potential smearing of the inertial peak was made by considering the doppler shift imposed on inertial motions by vorticity.

4.2 Analysis

The near-inertial (1/34.5h) and super-inertial (1/20h) peaks become more apparent after high passing with a 2.5 day cut off period and removing the tides (process described in chapter 5) (figure 4.1). The lower frequency peaks associated with higher mode ITW on Oahu or the Maui island group (1/47h and 1/64h) are hardly apparent after band passing with cut off periods of 1.5 and 5 days. (figure 4.2) Since the higher mode and Maui group ITW signals appear to be insignificant after filtering, focus was placed only on the near inertial frequency.

The HFR domain was subdivided into a nearshore and offshore area delineated by 21N. Spatially averaged power spectra in these regions was computed for comparison (figure 4.3). A significant decrease in the near-inertial peak in the offshore domain could have supported evidence for ITWs in the record. However, there is very little difference in the near-inertial peak between the two domains.

Isolation of the near-inertial ITW signal was further attempted using Empirical Orthogonal Function (EOF) analysis on the HFR data. EOFs were computed from band passed (1-2.5 day cut off periods) HFR record using MATLAB's eig routine.

Sea level data from Honolulu, Mokuolue and Makapuu was high passed with a 2.5 day cut off period and detided using t-tide. Coherence function and phase spectra between the lowest EOF temporal modes and Honolulu sea level is shown in figure 4.4. Coherence between the de-tided and band passed sea level records at each station is shown in figure 4.5.

To estimate the potential spectral smearing of the inertial frequency due to doppler shift induced by vorticity the effective inertial frequency was computed using inferred weekly median vorticity (computed as explained in Chapter 3) (Kunze, 1985).

$$f_{eff} \simeq f + \frac{1}{2}\left(\frac{\partial V}{\partial x} - \frac{\partial U}{\partial y}\right) = f + \frac{\zeta}{2} \qquad 4.1$$

The histogram of f_{eff} is plotted with the detided power spectra in figure 4.6.

4.3 Discussion

Detided power spectra shows a minor, but statistically significant, peak that appears to coincide with the lowest mode ITW for Oahu. The lower frequency, higher mode ITWs are insignificant after band passing.

There is no detectible difference between the inertial and near-inertial peaks from the near- and off-shore power spectra. Since ITW amplitudes are only significant within an e-folding distance on the order of the Rossby radius of deformation from the shore, dominance of the near-inertial peak from the near-shore domain would have provided a good indication of them. For the baroclinic ITWs of interest in this case, the Rossby radius of deformation is on the order of 10-15 km.

Coherence between low temporal modes and residual band-passed sea level indicates high levels of coherence in the near-inertial to inertial frequency band. However, the distinct peaks apparent in the power spectra are no longer present. The single peak is like due to ITWs since the horizontal inertial oscillations are not significant on tidal records.

The three Oahu sea level records exhibit significant coherence in the near-inertial to inertial range over a broad single peak. This test shows a longer time series would be needed to separate the inertial and near-inertial ITW signals from current records since ITWs are more significant in sea level data.

Further complicating the isolation efforts, the inertial frequency is susceptible to spectral smearing due to the doppler shift imposed by vorticity. In the presence of strong mesoscale eddies such as those generated by the islands windward of Oahu or high levels of vorticity as is generated by the flow through of the Ka'iwi channel, the shift can be significant.

4.4 Conclusion

Efforts to isolate the ITW signal were inconclusive due to the close proximity to the potentially

wide inertial spectral peak. However, since inertial motions are horizontal in nature their presence is not well characterized in sea level records. Therefore, the significant level of coherence between HFR and sea level records was likely attributed to ITW. A longer time series and/or observations in an environment where ITW frequencies are better separated from the inertial peak may allow isolation using the techniques outlined. With two HFR site derived vector currents, inertial motions could potentially be removed and the residual record could be examined for ITW evidence. Further analysis of the HFR data, especially with vector currents and longer records may allow a more fruitful analysis of ITWs.

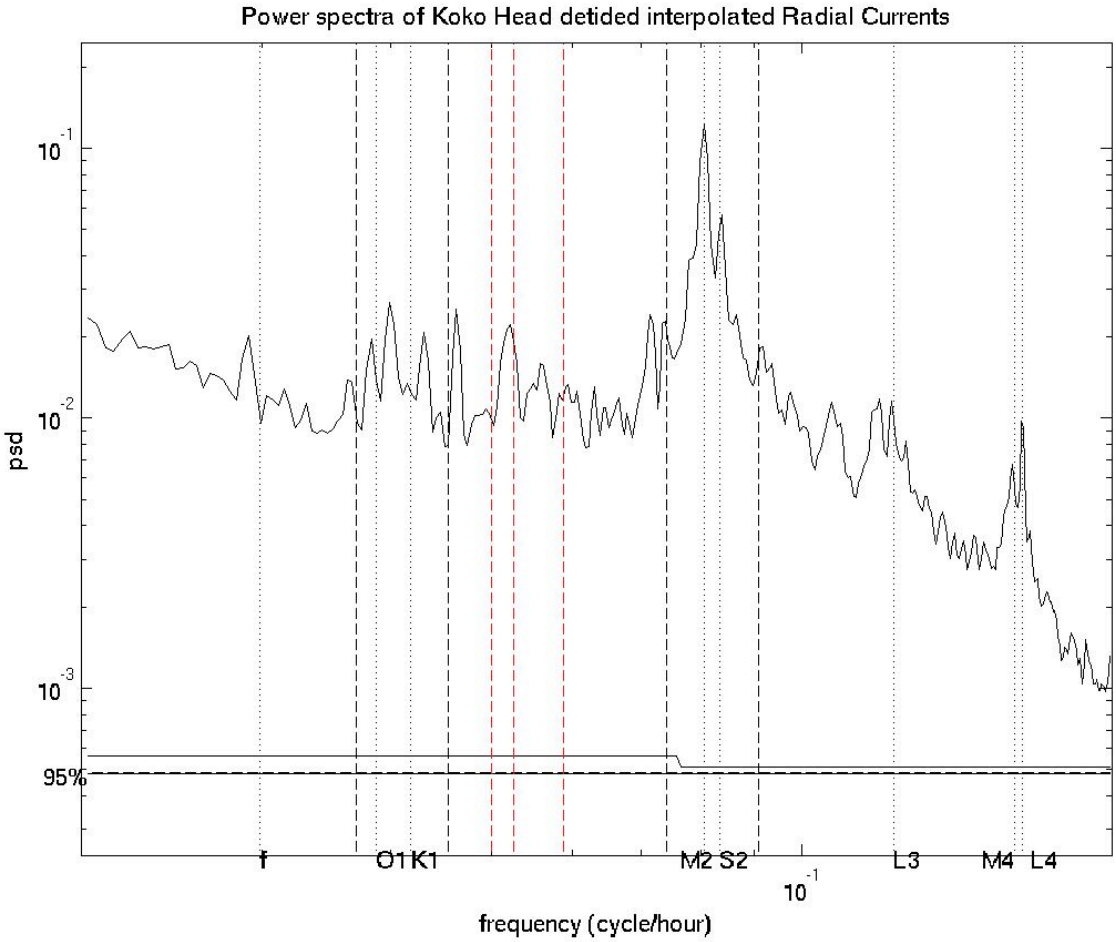

Figure 4.1: Spatially averaged power spectra for detided Koko Head HFR radial currents. 95% confidence interval indicated with thin black line at bottom, narrow at higher frequencies with increased degrees of freedom selected for higher frequencies. Vertical dotted and dashed black lines indicate major tidal constituents and inertial frequency (f). Vertical red dashed lines indicate superinertial island trapped frequencies of interest for Oahu (1/17h and 1/20h).

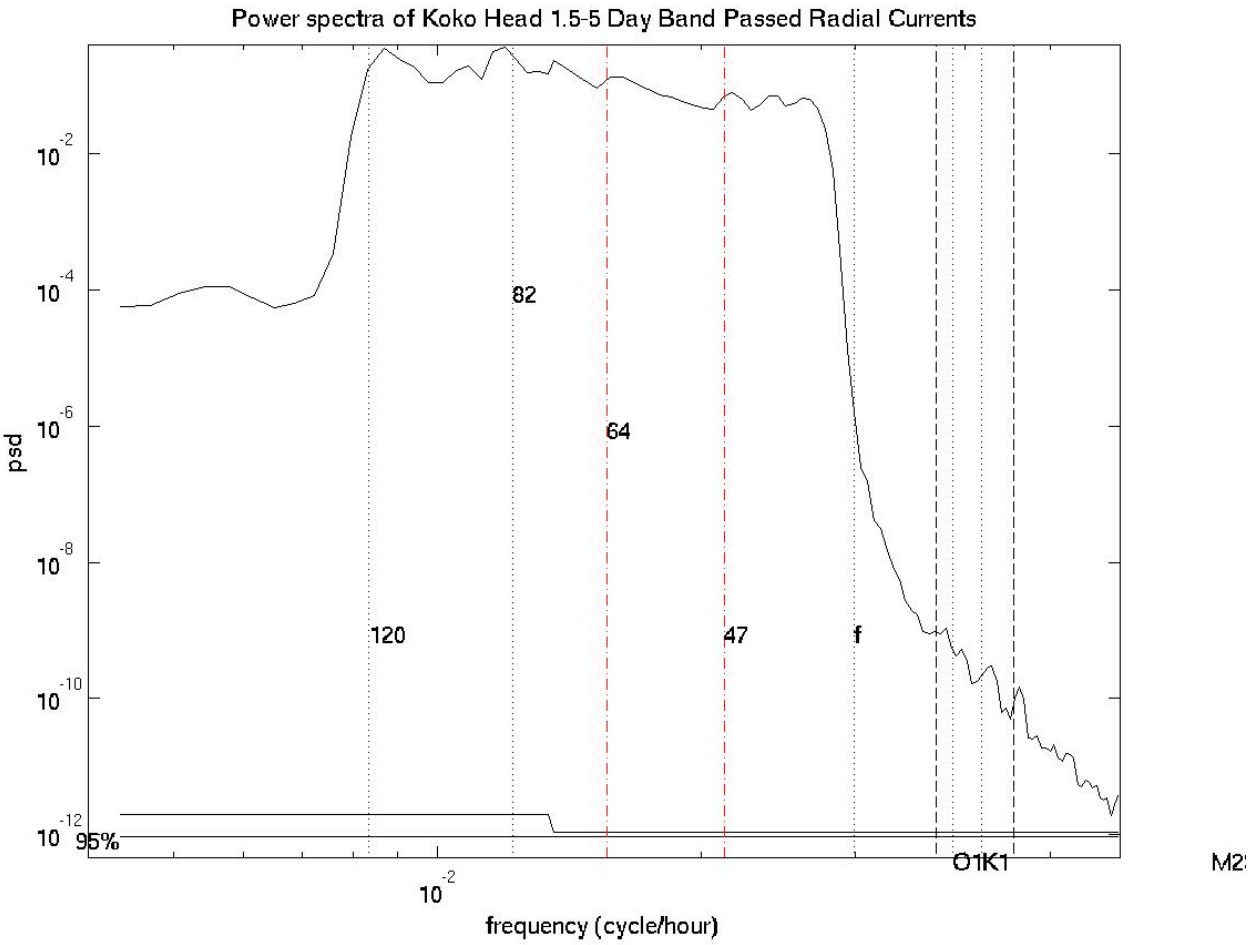

Figure 4.2: Spatially averaged power spectra for Koko Head band passed (1.5 – 5 day cut off periods) radial currents. 95% confidence interval indicated with thin black line at bottom, narrow at higher frequencies with increased degrees of freedom selected for higher frequencies. Dotted and dashed lines indicate cut off periods (~f and 5 days) and diurnal tidal band. Red dot-dashed lines indicate subinertial island trapped frequencies of interest for Maui island group (1/64h) and Oahu (1/47h)

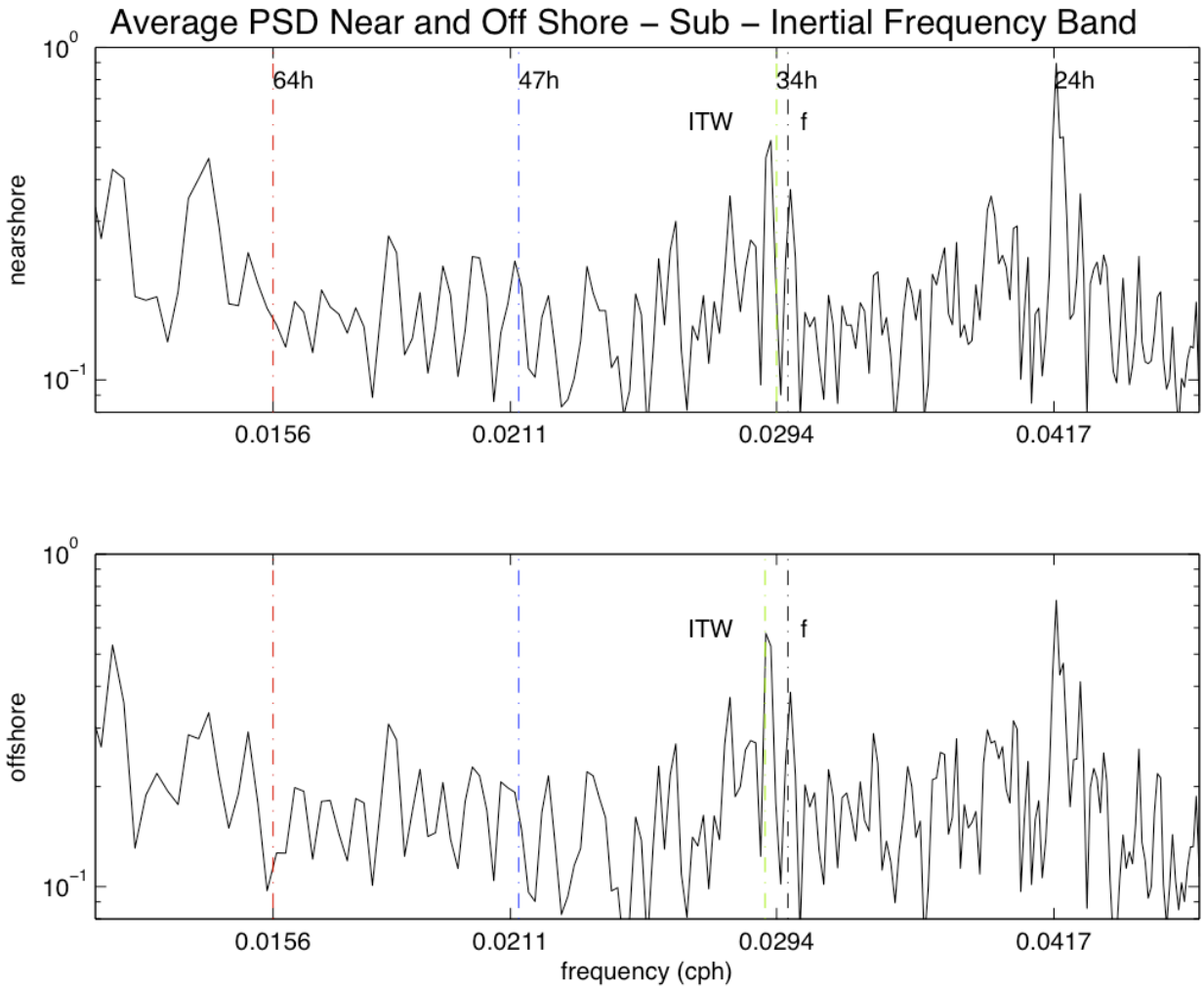

Figure 4.3: Spatially averaged power spectra for Koko Head near-shore (top) and off-shore (bottom) areas delineated by 21N. Dotted vertical lines indicate ITW and inertial frequencies (Red - 1/64h, Blue - 1/47h, Green - 1/34.5h, Black – 1/f).

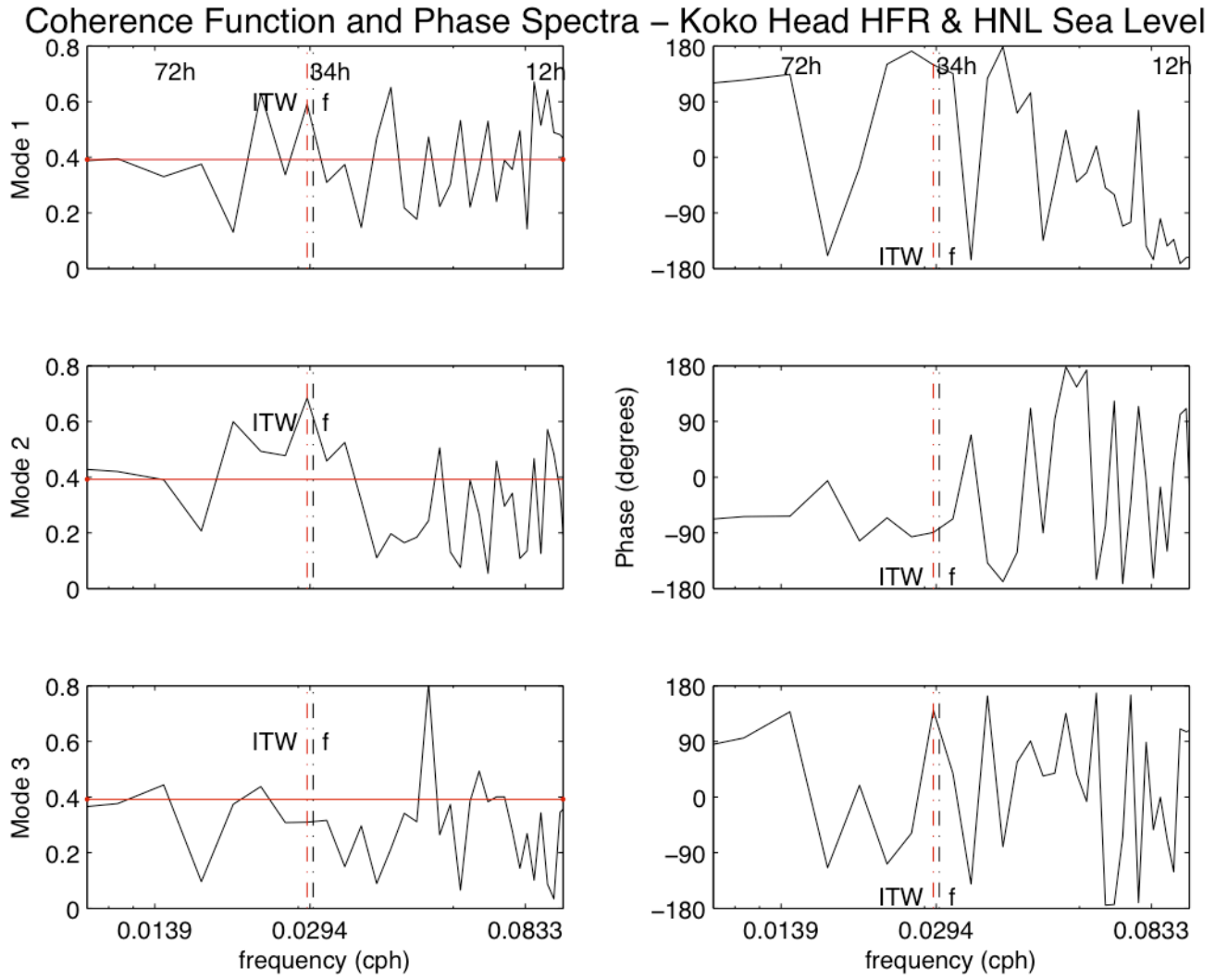

Figure 4.4: Coherence function (left) and phase spectra (right) for lowest three EOF temporal modes from 1 – 2.5 day band passed radial currents with detided Honolulu hourly sea level record. 95% confidence interval for coherence indicated with red horizontal line. Dotted vertical lines show near-inertial island trapped wave frequency (red) and inertial frequency (black).

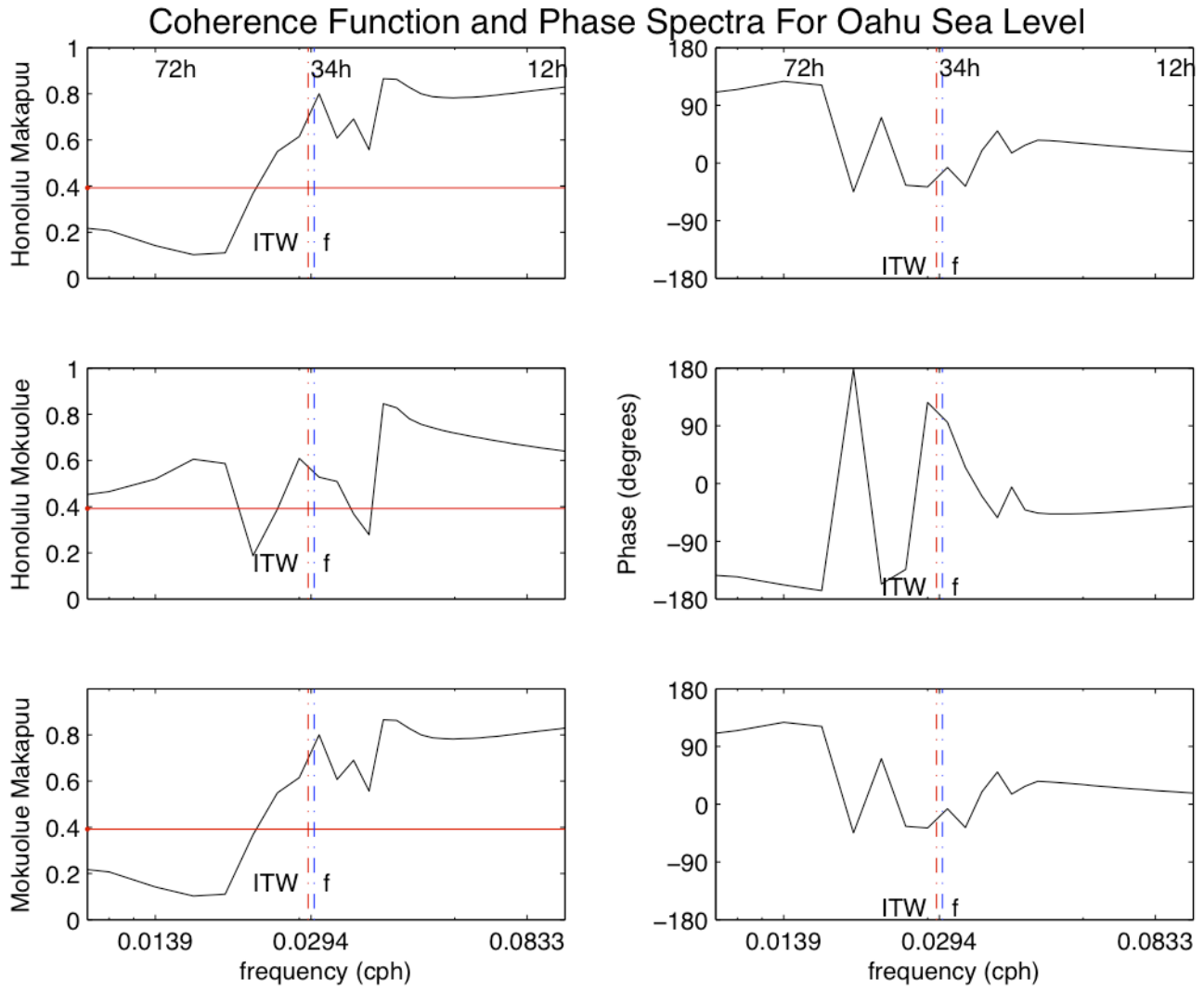

Figure 4.5: Coherence function (left) and phase spectra (right) between band passed (1 - 2.5 day cut off period) Oahu sea level stations. 95% confidence interval for coherence indicated with red horizontal line. Dotted vertical lines show near-inertial island trapped wave frequency (red) and inertial frequency (blue).

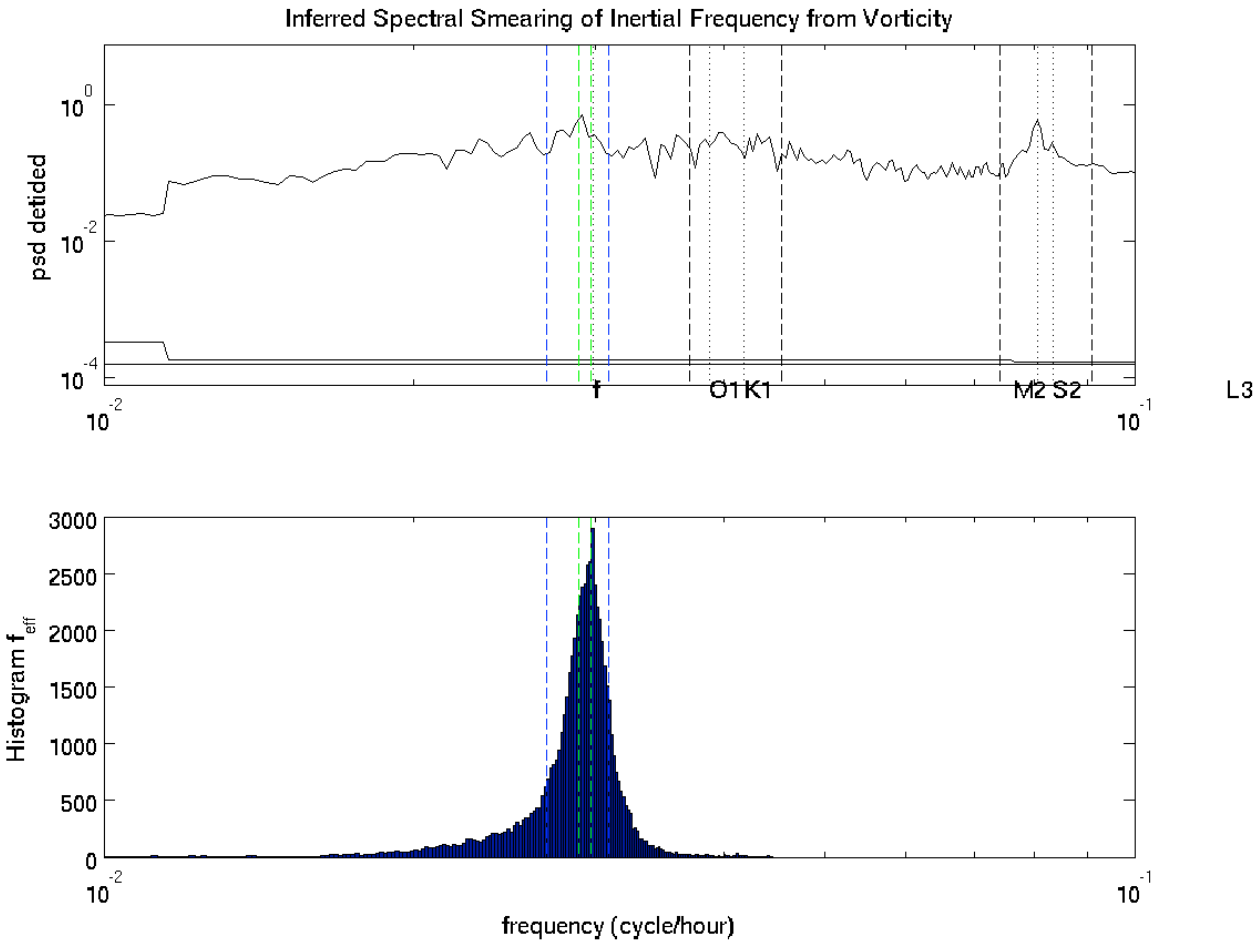

Figure 4.6: Spatially averaged and detided power spectra for Koko Head HFR (top) with histogram of effective inertial frequency histogram (bottom). Dashed black lines for top figure identify semi-diurnal and diurnal tidal bands. Black dashed lines are labeled with the respective tidal constituent or inertial frequency (f). Green dashed lines indicate the limits of the 40 and 60 quantile values from the effective inertial frequency distribution. Blue dashed lines indicate the limits of the 15.8 and 84.1 quantile values from the effective inertial frequency distribution.

Chapter 5

Mamala Bay Tidal Observations and Models

5.1 Mamala Bay Tidal Dynamics

Baroclinic tides are generated when the dominant semi-diurnal barotropic tide traverses steep bathymetry near Kaena Ridge and Makapuu Point (Wunch, 1975; Merrifield et al. 2001). Coherent propagation of the lower modes of this internal tide is apparent over thousands of kilometers north and south of these generation zones in altimetric data (Ray et al., 1996). In Mamala Bay internal tides exhibit dramatic temporal variation attributed to stratification changes and advection by mesoscale flow (Alford et al., 2006). Oppositely traveling internal tidal signals from Makapuu Point and Kaena Ridge are most commonly dominated by the westward moving internal tide from Makapuu. However at times when their intensity is approximately equal a partially standing internal wave can develop (Alford et al., 2006; Martini et al., 2007). Despite deterministic forcing, tidal expressions in Mamala Bay are highly complex due to interference from these energetic internal tides and interaction with mesoscale flow.

HFR observations show semi-diurnal tides are the most energetic super-inertial signal. Numerical simulations of regional tidal patterns exhibit slightly varying characteristics of the dominant M2 semi-diurnal constituent. Princeton Ocean Model (POM; Carter, 2008), Primitive Equations Z-coordinate-Harmonic Analysis Tides (PEZ-HAT; Zaron 2008) and Regional Ocean Model System (ROMS; Powell) simulated M2 amplitude and phase characteristics are compared to show the degree of variation in existing models and differences from harmonic analysis of radial currents collected from Koko Head HFR. Observations of the incoherent portion of the semi-diurnal tide are presented.

5.2.1 Numerical Models

Tidal characteristics generated by three models were used for comparison with observed patterns. All models have been validated with altimetry, tidal records and other moored observations. (Carter et al., 2008; Zaron and Egbert, 2007)

POM is a three-dimensional, sigma coordinate, primitive equation model with a 2.5 turbulence closure scheme used in this case to investigate tidal processes. The model is forced by M2 tidal elevation at the lateral boundaries, integrated for 18 tidal cycles, the last 6 of which are used to generate tidal harmonics (Carter et al., 2008). Stratification for the simulation was based on the ten year Hawaiian Ocean Time Series (HOT) mean. High resolution experiments (~1 km horizontal grid spacing) were used to generate a tidal energy budget for the main Hawaiian Island region. In these simulations, baroclinic energy generated in the vicinity of Makapuu point was steered through the Ka'iwi Channel around the south shore of Oahu into Mamala Bay or was dissipated along the edges of Penguin Bank. Baroclinic tides generated along Kaena Ridge were less significant within Mamala Bay.

PEZ-HAT is a data-assimilating, three-dimensional, z-coordinate primitive equation model with specified constant viscosity and diffusivity parameters (Zaron and Egbert, 2006). Its structure is founded on the Geophysical Fluid Dynamics Laboratory Modular Ocean Model (GFDL MOM3, Pacanowski and Griffies (1999)) and includes software for implementing astronomical tidal forcing, open boundary conditions and harmonic analysis of the solutions (Zaron et al. 2009). Forcing is generated from the normal component of barotropic tidal current on the open boundaries, allowing elevation to fluctuate. Integration is carried through 14 tidal cycles where harmonics are generated over the last 3. To assimilate the model obtains an estimate of tidal fields that minimizes the weighted sum of squared data and model residuals. The observations are weighted with the inverse of the nominal observation error and model dynamics are weighted with the inverse of a plausible estimate of the model forcing (Zaron et al., 2009). HFR tidal observations during the Hawaiian Ocean Mixing Experiment (HOME) were assimilated to PEZ-HAT at a 2 km grid spacing. Stratification was specified

to match the mean from HOT during the HOME HFR deployment.

ROMS is a data assimilating, free surface, terrain following vertical S coordinate, terain following orthogonal curvilinear coordinate in the horizontal, primitive equation model using the Generic Length Scale two equation turbulence closure scheme. The Hawaii Oahu Grid (HIOG) investigated is a nested child to the 4 km horizontal grid spacing Hawaiian Islands Grid (HIIG). HIOG resolution is 1.1 km horizontal spacing and 30 vertical layers. Tidal elevation and other satellite inputs are forced at the boundary of the parent grid. Solutions for HIIG are imposed at the boundary of HIOG. Weather Research and Forecasting (WRF) model produces atmospheric forcing across the domain. Modeled surface currents are archived every three hours for the period investigated (September 1, 2009 – December 31, 2009). T-tide harmonic analysis of ROMS time series provided tidal characteristics for the ten major constituents in the observations.

5.2.2 Model Comparison

Tidal ellipses are a compact method used to describe tidal current variance using major and minor axes (A_{maj} and A_{min}), inclination and phase. The axes describe the magnitude of the current in 2 orthogonal directions, inclination provides orientation for the axes and phase indicates time lag from Greenwich when the time vector passes the northern semi-major axis.

Tidal ellipses can be represented using phasors, ellipse components, or as in the POM and PEZ-HAT model outputs - U and V phase and amplitude. To directly compare these model outputs with observed radial characteristics projection into the radial reference frame is required. As observed from Koko Head, the radial tidal amplitude is the magnitude of the vector intersecting the current ellipse radially away from the site (Figure 5.1). Phase is defined as the time lag corresponding with the maximum outward current. When using tidal characteristics expressed in U and V components of amplitude and phase, it is easy to see limiting cases along principle coordinates. For example, at 180°T

the HFR measures only the V component of the current: $V = U_R$ and $U = 0$. Therefore, the tidal amplitude observed along that bearing is attributed completely to the harmonic analysis of the meridional current. The following expressions provides a more general relation for projecting phase:

$$A_1 = U_a \cos(\theta) \qquad A_2 = V_a \sin(\theta) \tag{5.1}$$

$$\phi_1 = U_p \qquad \phi_2 = V_p \tag{5.2}$$

Where U_p and V_p are U and V phases and U_a and V_a are U and V amplitudes. The projected amplitude and phase then can be computed as:

$$A_{proj} = \sqrt{(A_1^2 + A_2^2 + 2\,A_1\,A_2 \cos(\phi_1 - \phi_2))} \tag{5.3}$$

$$P_{proj} = \arctan[(A_1 \sin(\phi_1) + A_2 \sin(\phi_2)) / (A_1 \cos(\phi_1) + A_2 \cos(\phi_2))] \tag{5.4}$$

Comparison of currents in a single dimension, be it radial or cartesian, eliminates a potential phase ambiguity when major and minor axes are nearly equal in magnitude. If using vector representation, choosing the wrong major axis when $A_{maj} \approx A_{min}$ could result in an unintentional 90 degree phase shift. An example of this ambiguity is the apparently circular ellipse in the southern domain of figure 5.1. Therefore while comparison of modeled and observed tidal characteristics requires projection, the stability of the single coordinate comparison is greater than combined vector amplitudes and phases.

5.3 Observational Analysis

When conducting a least squares fit, more weight is given to large departures of the data from the modeled parameter than to small departures. In order to minimize impacts of low frequency variability on the tidal least squares fit, high pass filtering was necessary. Gaps in data made interpolation necessary prior to filtering. To prevent interpolation between tidal crests and troughs, the dominant semi-diurnal tide was removed locally with T-tide over 2-day sliding windows when at least 50% of the data was present. Small gaps in data were linearly interpolated in the residual record. The

interpolated residual record was low passed with a 2-day cutoff period and subtracted from the original record, resulting in a high passed record for tidal analysis.

T-tide was used to estimate the phase, amplitude and associated 95% confidence intervals of the observed M2, S2, N2, L2, K1, O1, Q1, M3, M4 and S4 tidal constituents. The record length (T) was sufficient to satisfy the Rayleigh criteria (R), which was set to 1, for all constituents. $(|\Delta f|T \geq R)$

For point-by-point comparison, all modeled and observed characteristics were re-gridded to the PEZ-HAT 2-km horizontal grid spacing.

5.4 Comparison of Tidal Characteristics

Semi-diurnal tides are an order of magnitude more energetic than other superinertial currents (Figure 5.2). Peaks at M2 and S2 are the most significant with minor contributions from other semi-diurnal constituents. Distinct O1 and K1 peaks are apparent. Higher harmonics of semi-diurnal constituents also display statistically significant peaks. Even after removing the coherent tidal component as identified by the least squares fit, the semi-diurnal tide band remains the dominant peak due to incoherent tidal energy. A broad diurnal peak in the de-tided spectra between K1 and O1 is also present.

Observed and modeled M2 phase and amplitude characteristics are plotted in figures 5.3 and 5.5. Modeled M2 phase and amplitude minus observed phase and amplitude are shown in figures 5.4 and 5.6.

All three models show similar phase to the observations along Oahu's south east shore and along the north and south shelf to Penguin Bank. The three models show a small region of phase lag west of Pearl Harbor and a larger area of phase lead extending from Barber's Point south along the western area. POM shows a small spatial phase fluctuation at the western tip of Penguin Bank.

Amplitude differences from the observations show that POM and PEZ-HAT over estimate the

magnitude near shallow bathymetry except for the area near Koko Head which is under estimated by PEZ-HAT. ROMs underestimates the amplitude near shallow features but accurately reproduces the observations in the Ka'iwi channel area.

All models generally emulate the M2 characteristics observed but the smaller scale features in POM are exaggerated compared to the observations. Phase difference and amplitude ratio histograms show peaks centered near zero for all models (Figure 5.7 and 5.8). Large tails present on the histograms however indicate level of agreement is moderate. The scatter plot of modeled M2 amplitude plotted against observed amplitude shows that POM most closely matches observations (Figure 5.9)

5.5 Discussion

Tidal trends observed by HFR current meters collected during HOME were compared to POM and PEZHAT, for leeward Oahu where general agreement between the modeled phases and observations were found (Chavanne, 2007). Observed strong temporal variability in tidal characteristics was attributed to interference between other tidal constituents and interactions with mesoscale currents.

Minor differences between models and observations are presumed to be due to model assumptions or limitations. Physical processes excluded or simplified by the models are the likely source of the differences in the tidal characteristics.

POM has been used widely to show tidal dynamics for region (Merrifield et al., 2001, Merrifield and Holloway, 2002; Eich et al., 2004; Martini et al, 2007, Carter et al., 2008). Previous modeling efforts have shown a high degree of sensitivity to grid spacing. POM simulation evaluated herein were based on high resolution (~1 km) grid spacing, and may account for some of the variation from ROMS (1.1 km) and PEZ-HAT (~2 km).

Both POM and PEZ-HAT (prior to assimilation) simulations are conducted in an otherwise

quiescent ocean. Advection by mean and mesoscale flow is therefore omitted, likely preventing realistic variability in baroclinic portion of the tide. However, residual values resulting from data assimilation in PEZ-HAT may emulate mesoscale flow and therefore may reflect mesoscale dynamics.

Stratification within the domain is dynamic with seasonality. HOT 10 year mean, HOT mean during HOME HRF deployment and glider observations from spring 2010 near Ka'iwi channel temperature, salinity and buoyancy profiles are plotted in figure 5.10. Glider observations show stronger stratification which would suppress the surface expression of the baroclinic tide.

Weaker stratification allows stronger surface expression of the baroclinic tide. Advection and refraction of internal tidal features by the mesoscale smears out the baroclinic tide. Small scale features exhibited in the POM simulation but absent from the other models are likely primarily due to the weaker stratification in the 10 year HOT mean and absence of background flow. Mesoscale flow is explicitly expressed in ROMS and implicit in PEZ-HAT after data assimilation.

Observed ratio of the average semi-diurnal power spectra for tidal currents and residual currents is shown in figure 5.11. Semi-diurnal frequency band was defined as:

$$\left[N2 + \frac{1}{T} > semi - diurnal > L2 - \frac{1}{T} \right] \qquad 5.5$$

This comparison of coherent to incoherent semi-diurnal tidal energy shows coherent energy is dominant near shallow bathymetry as expected. Incoherent energy is strong in areas where model characteristics differed from observations such as near Barber's Point, along western portion of domain and at western flank of Penguin Bank. The incoherent portion of the tide is presumably attributable to the surface expression of the internal tide generated nearby at Makapuu Point then topographically steered to the areas where incoherent energy is dominant. Figure 5.12 is the spatial distribution of incoherent semi-diurnal energy density and is assumed to be representative of internal tides. Isolation

of the regions of elevated energy density to deeper areas of the domain support the signal being due to internal tides. Furthermore, the western beam near Barber's Point very closely coincides with beams identified by Chavanne in a similar analysis of internal tides evident in the HOME HFR deployment (figure 5.13).

5.6 Conclusion

Surface radial tidal currents in Mamala Bay were isolated from an HFR at Koko Head and were compared to modeled tidal currents from ROMS, POM and PEZHAT. Modeled tidal features generally mimicked the observations. Model specifications such as stratification and physical simplifications such as omission of back ground flow are likely responsible for the minor differences between the simulations. Observed incoherent semi-diurnal tidal energy is most significant in deeper areas where the modeled characteristics differed from observations. With general agreement between the modeled and observed tides, confidence is improved in both the observations and the models.

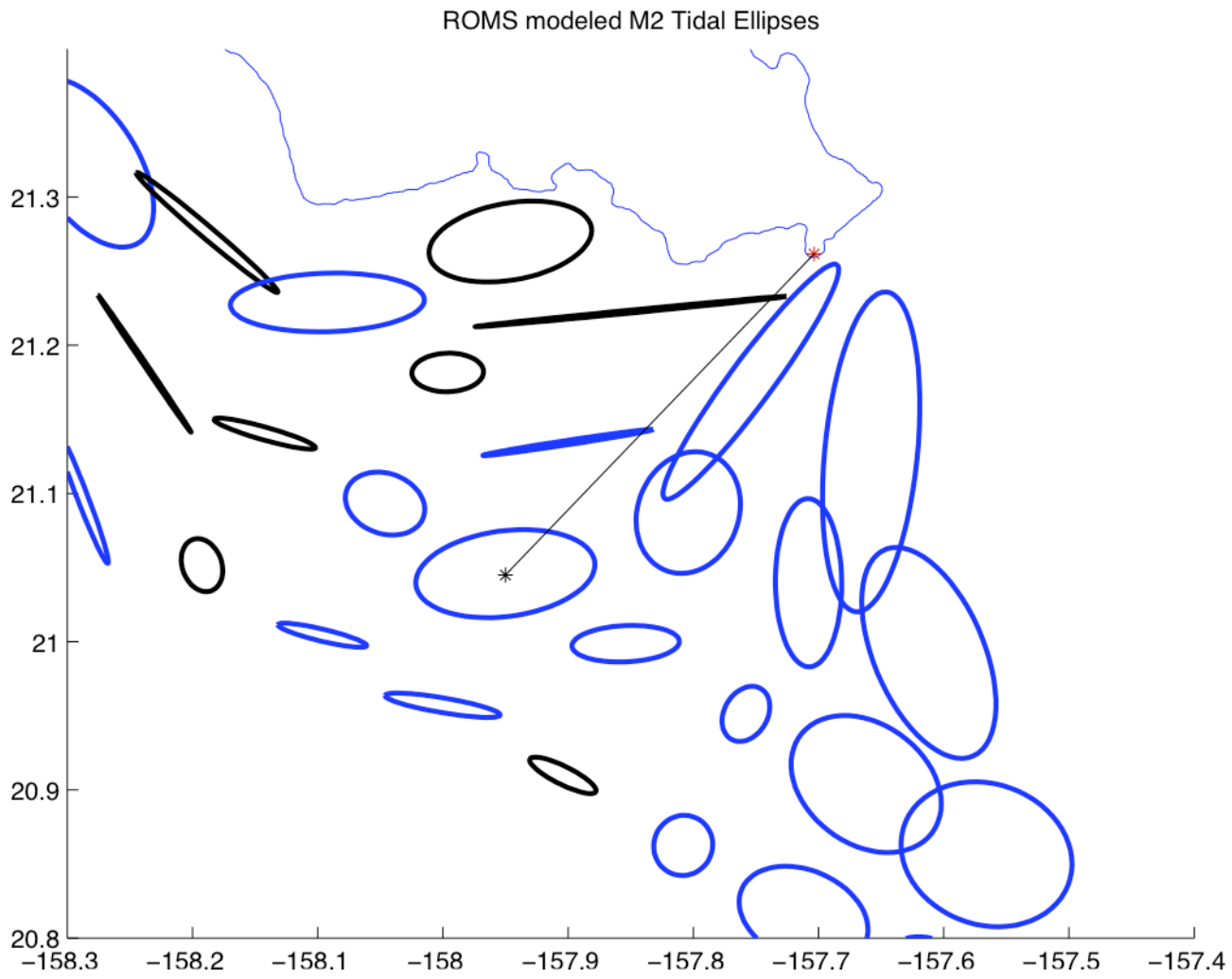

Figure 5.1: ROMS modeled M2 tidal ellipses. Black ellipses represent counter clockwise and blue represent clockwise rotation. Koko Head location noted with red asterisk. Thin black line from Koko Head to center of tidal ellipse provides an example of tidal characteristics observed in radial projection.

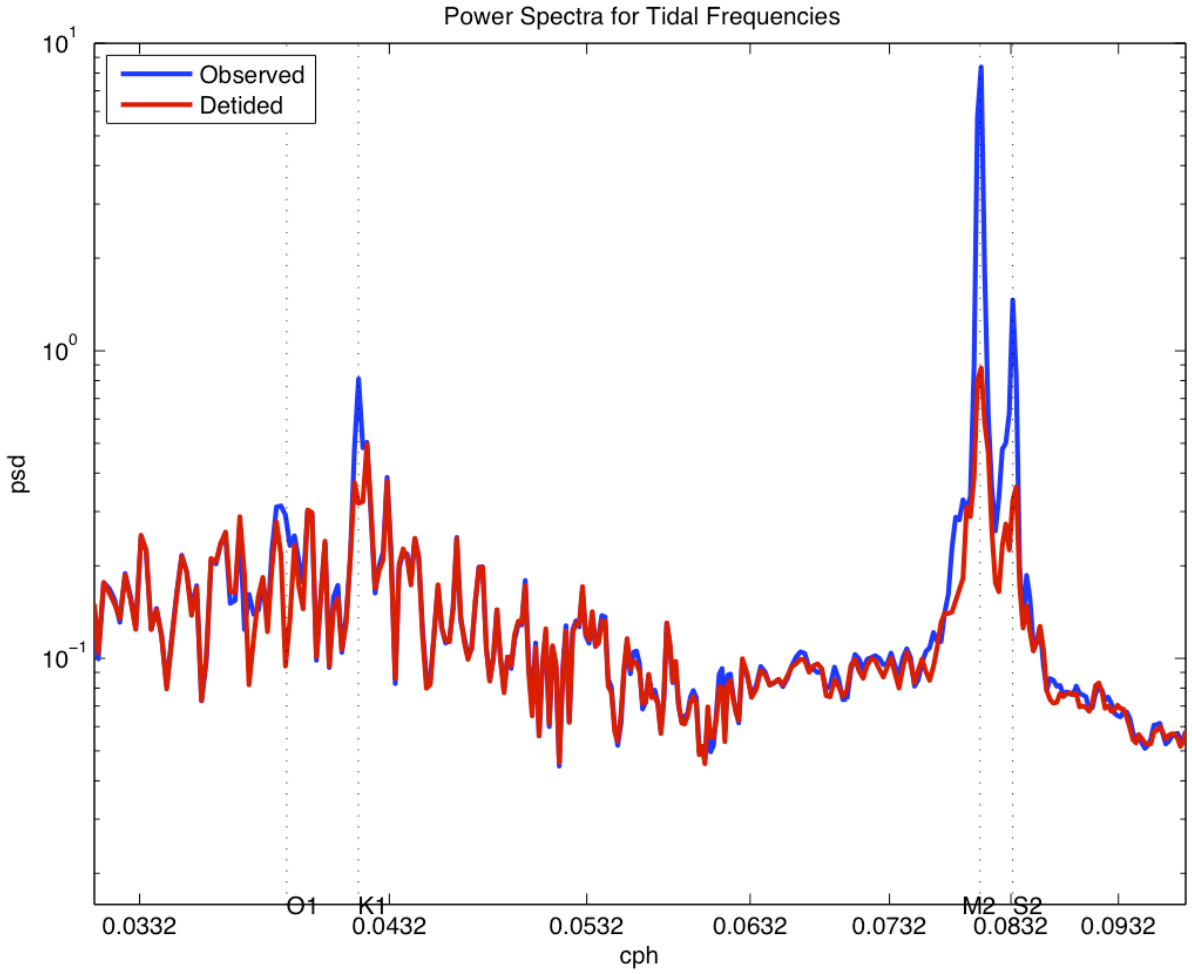

Figure 5.2: Spatially averaged power spectra for interpolated radial currents and detided interpolated radial currents. 95% confidence interval indicated with thin black line at bottom, narrow at higher frequencies with increased degrees of freedom selected for higher frequencies. Vertical dotted and dashed black lines indicate major tidal constituents and inertial frequency.

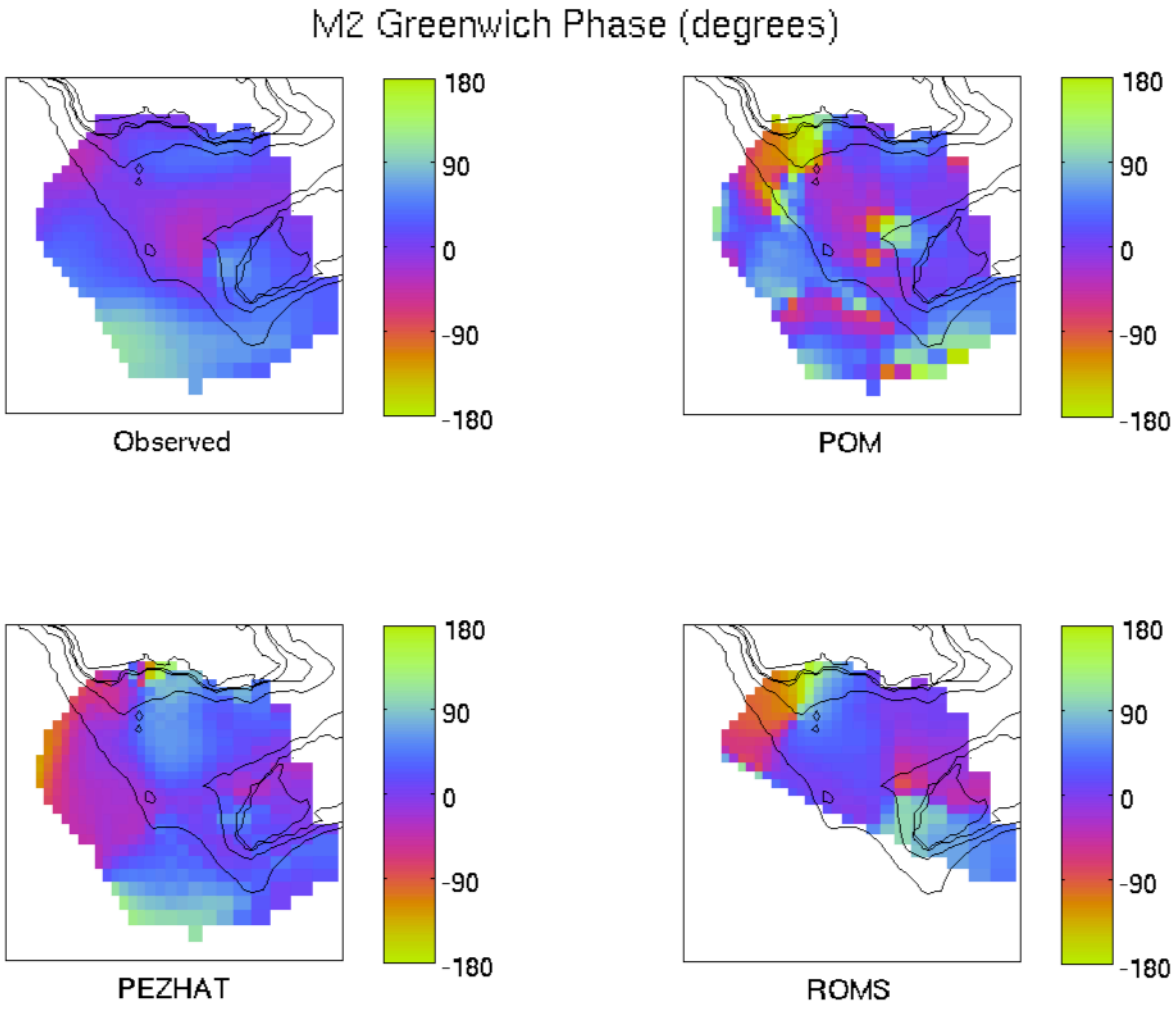

Figure 5.3: Observed and model projected M2 tidal phase.

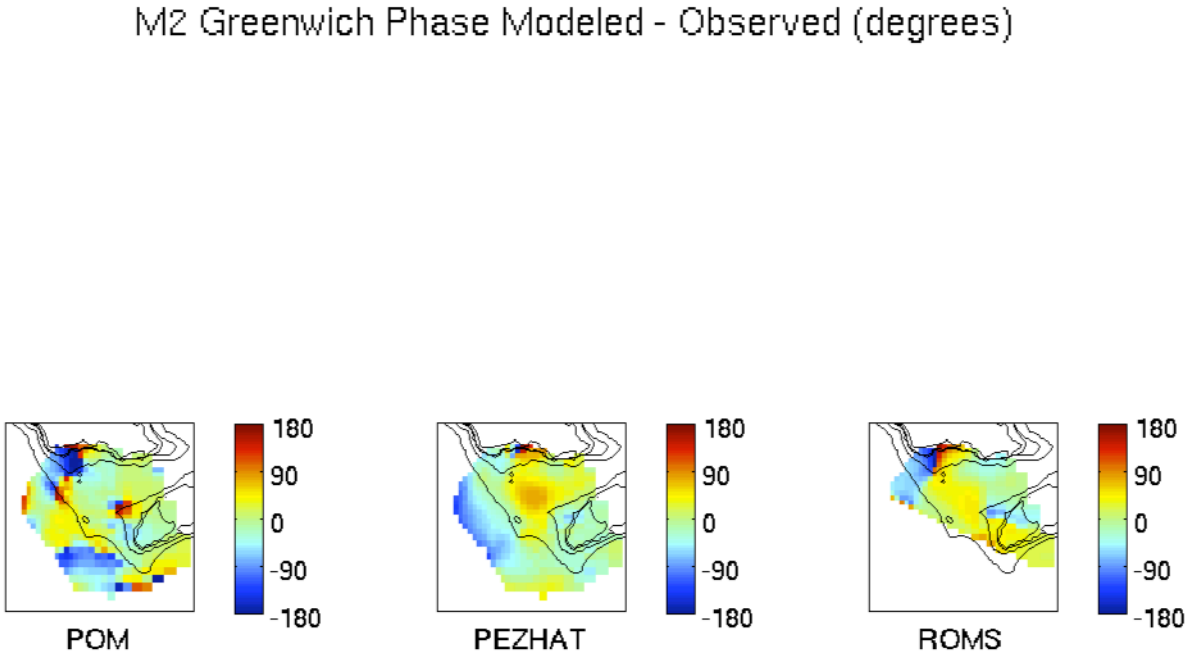

Figure 5.4: M2 phase difference, observed minus modeled.

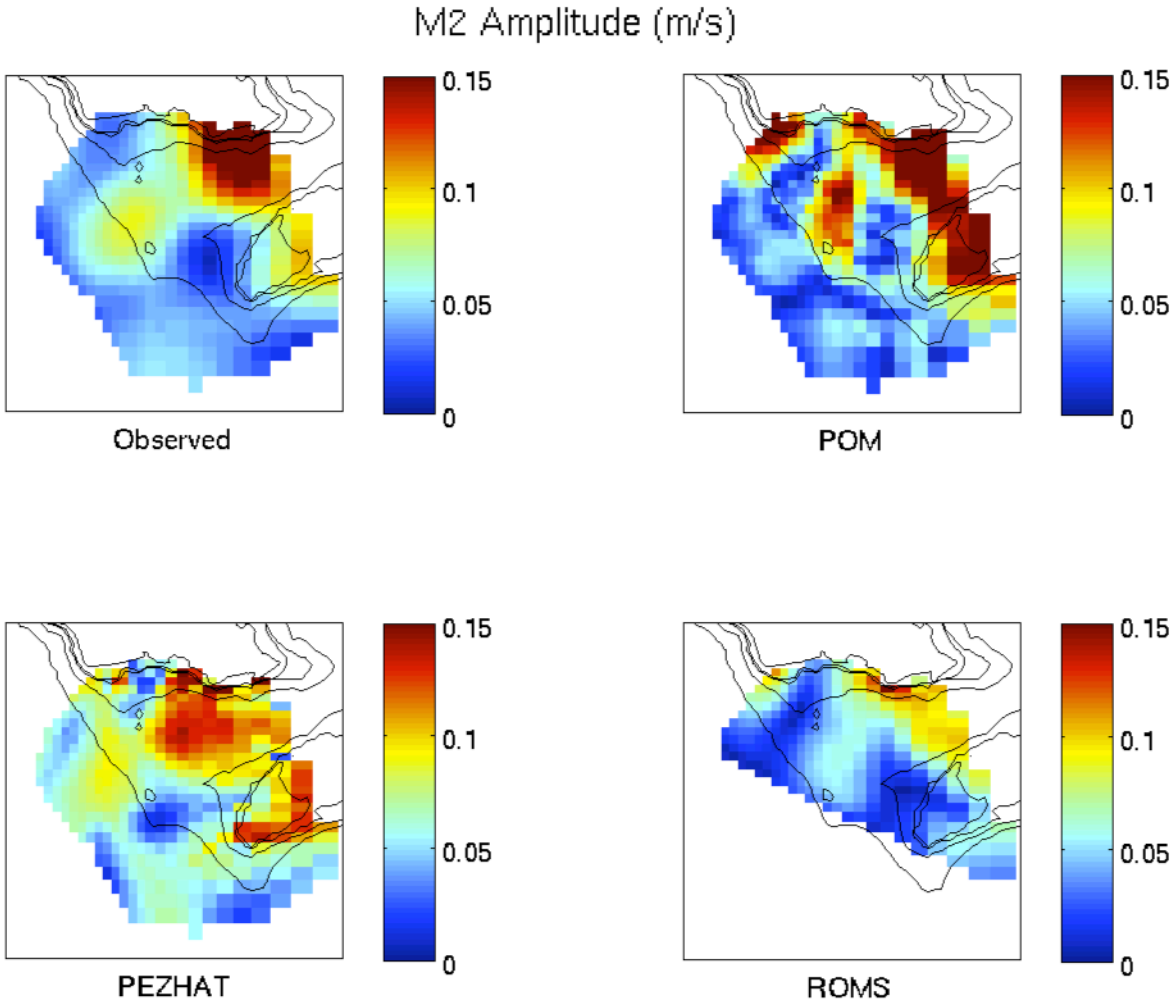

Figure 5.5: Observed and model projected M2 tidal amplitude.

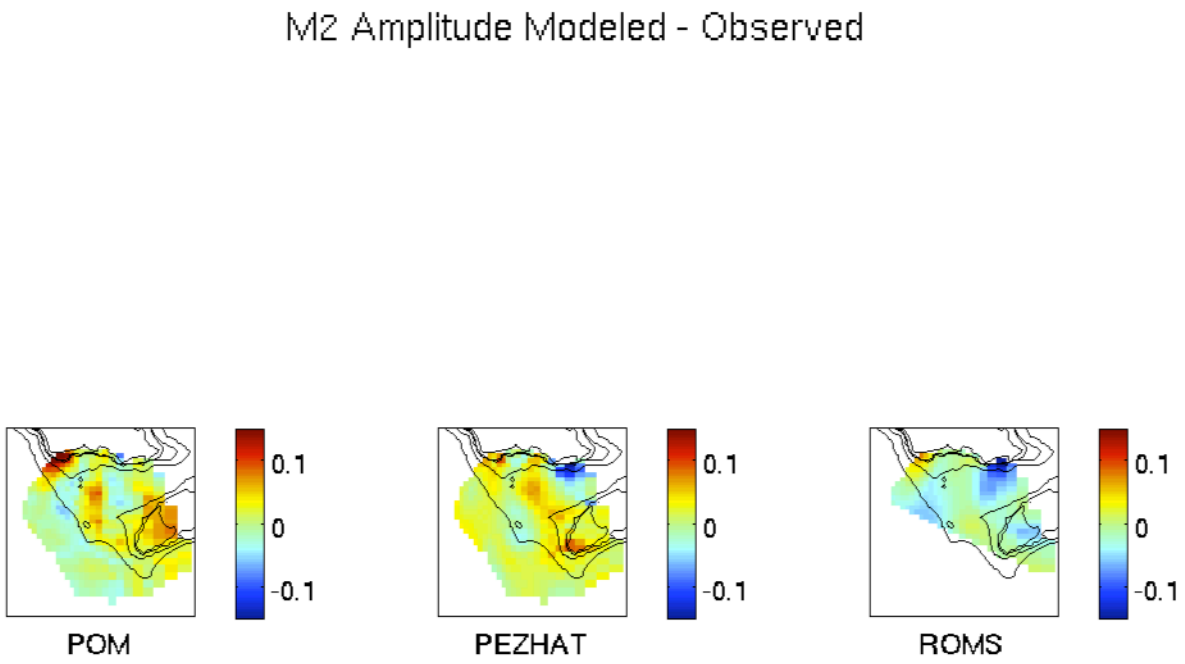

Figure 5.6: M2 amplitude difference, observed minus modeled.

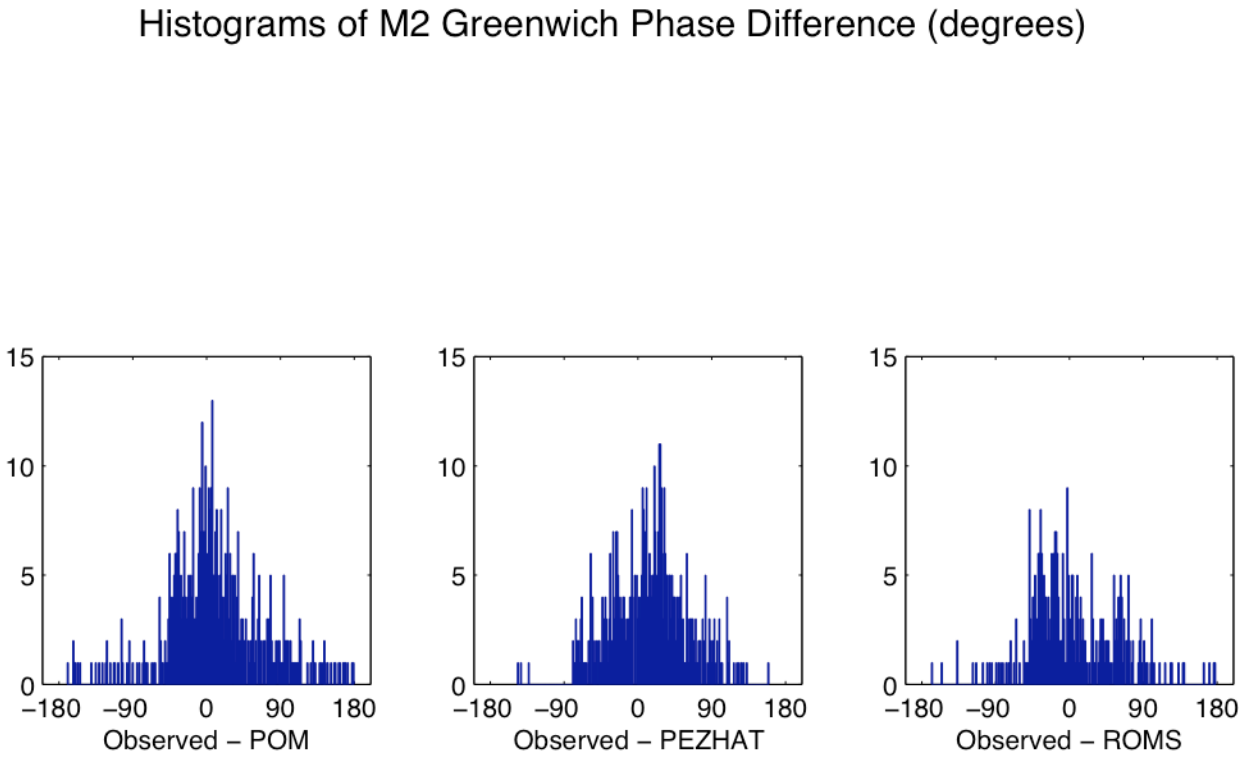

Figure 5.7: Histograms of observed M2 phase – modeled M2 phase.

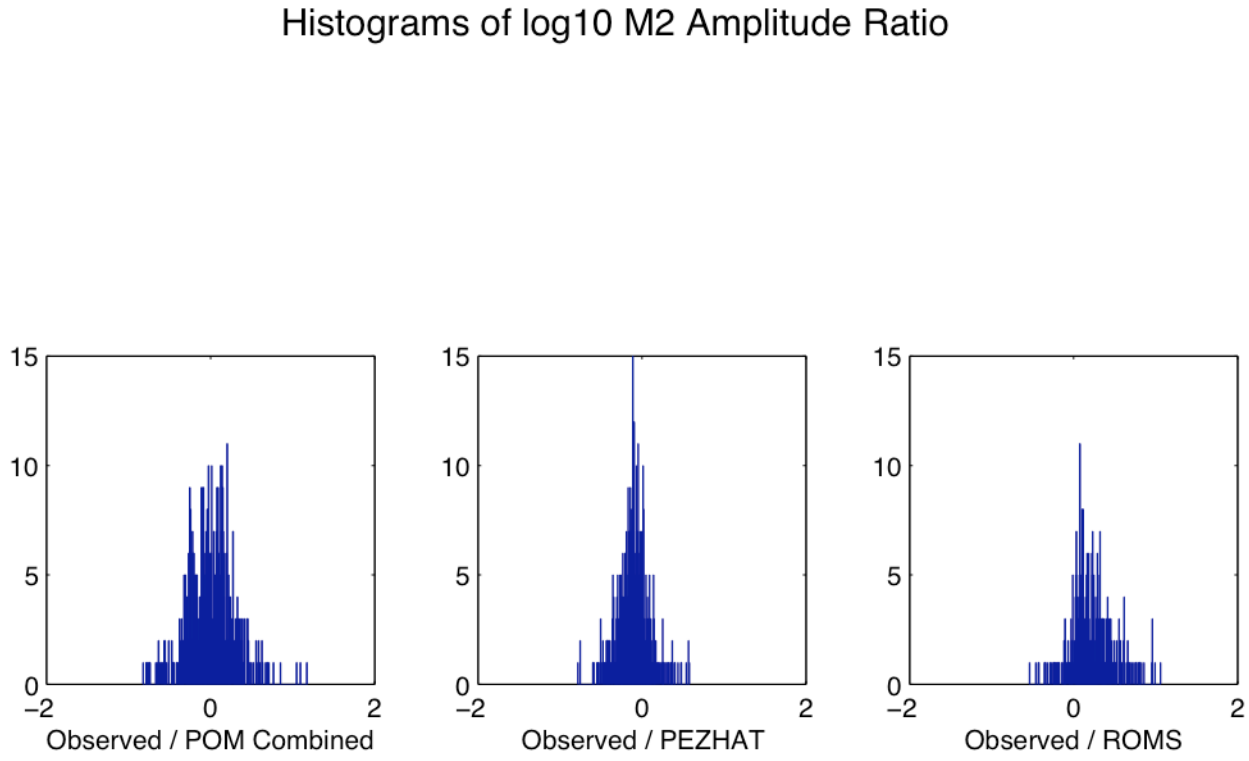

Figure 5.8: Histograms of $10 \log_{10} \frac{observed\ M2\ Amplitude}{modeled\ M2\ Amplitude}$

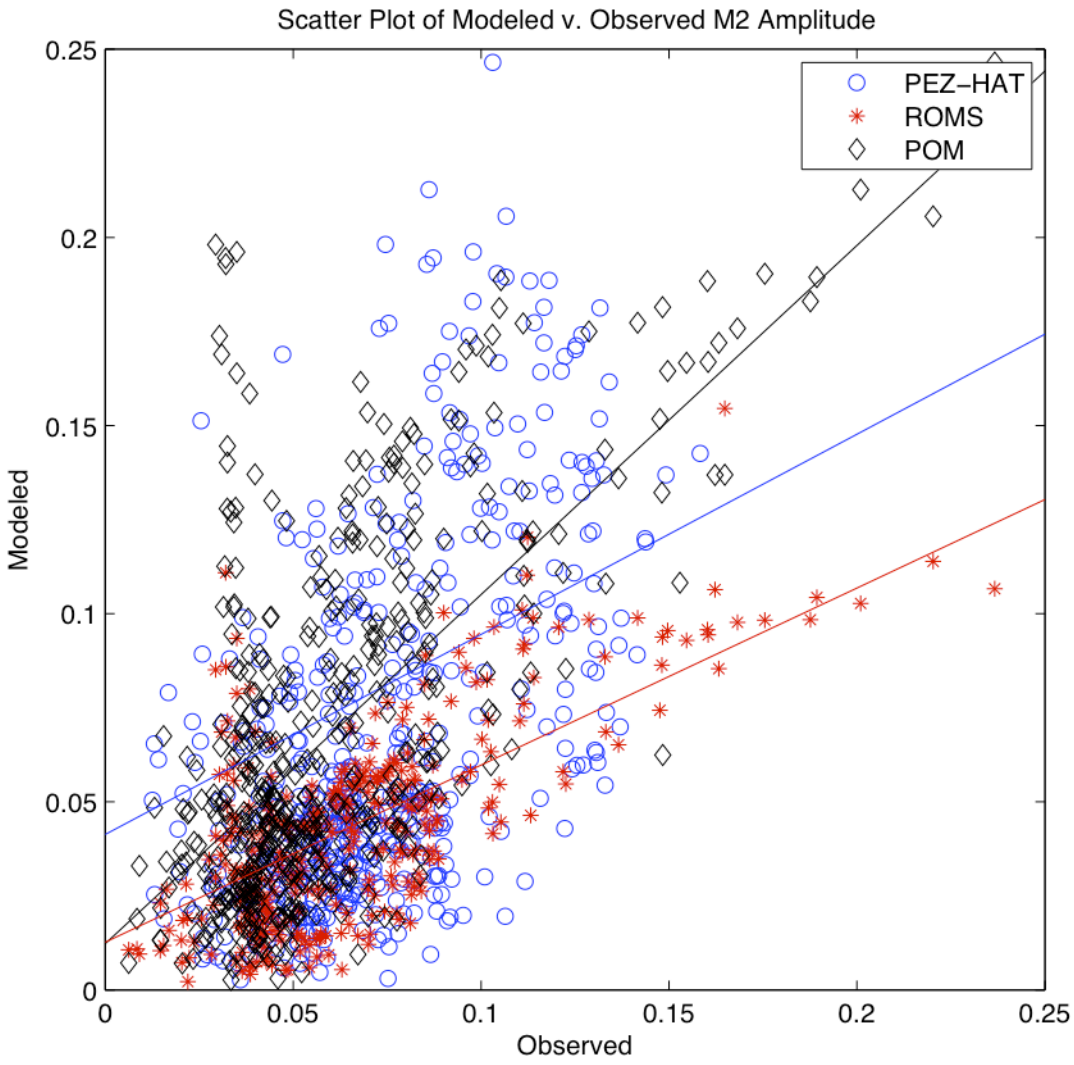

Figure 5.9: Scatter plot of M2 modeled amplitude v. observed amplitude.

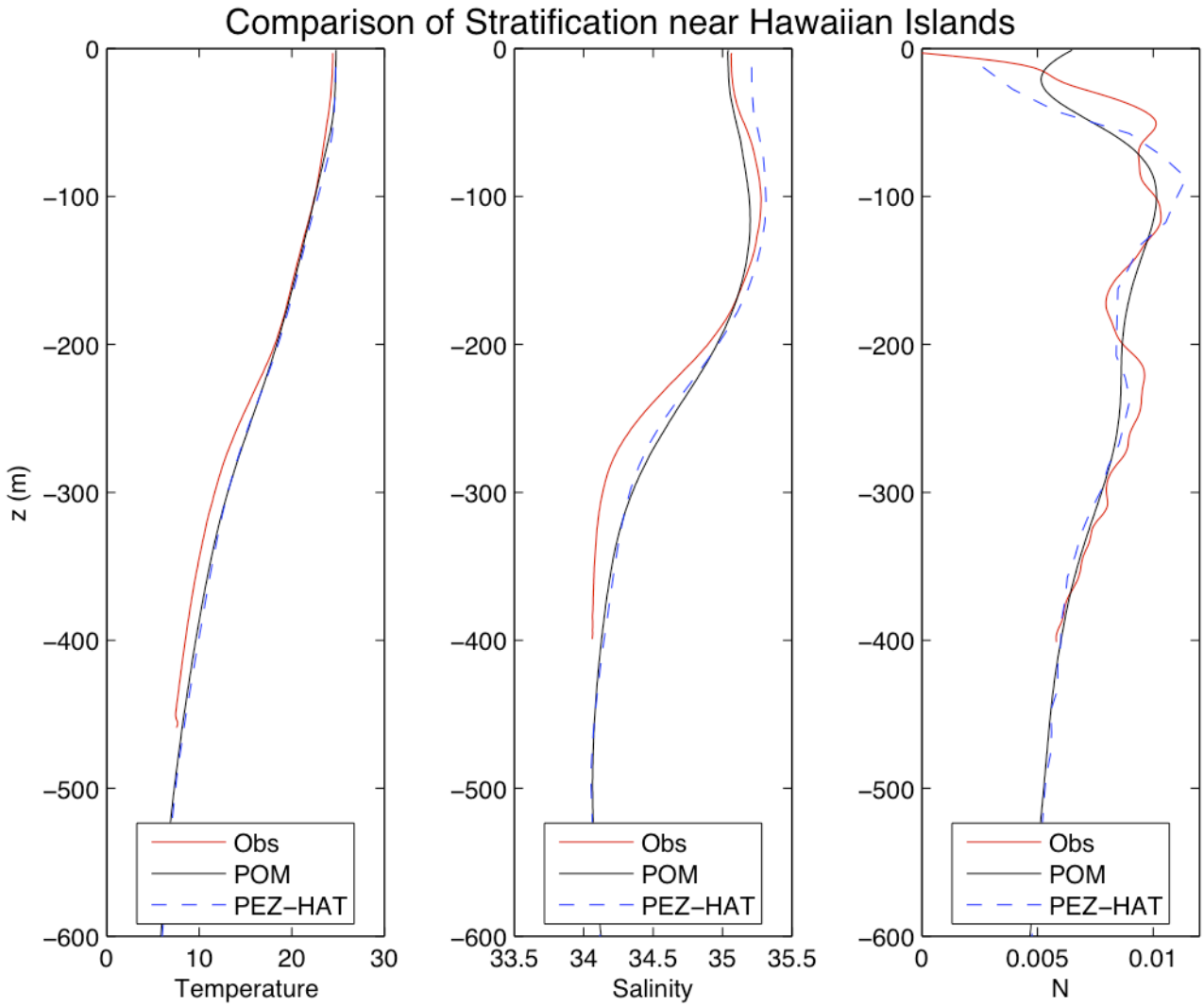

Figure 5.10: HOT 10 year mean, HOT mean during HOME HFR deployment and spring 2010 (April and May 2010) mean glider temperature, salinity and buoyancy profiles. Glider data courtesy of Glenn Carter.

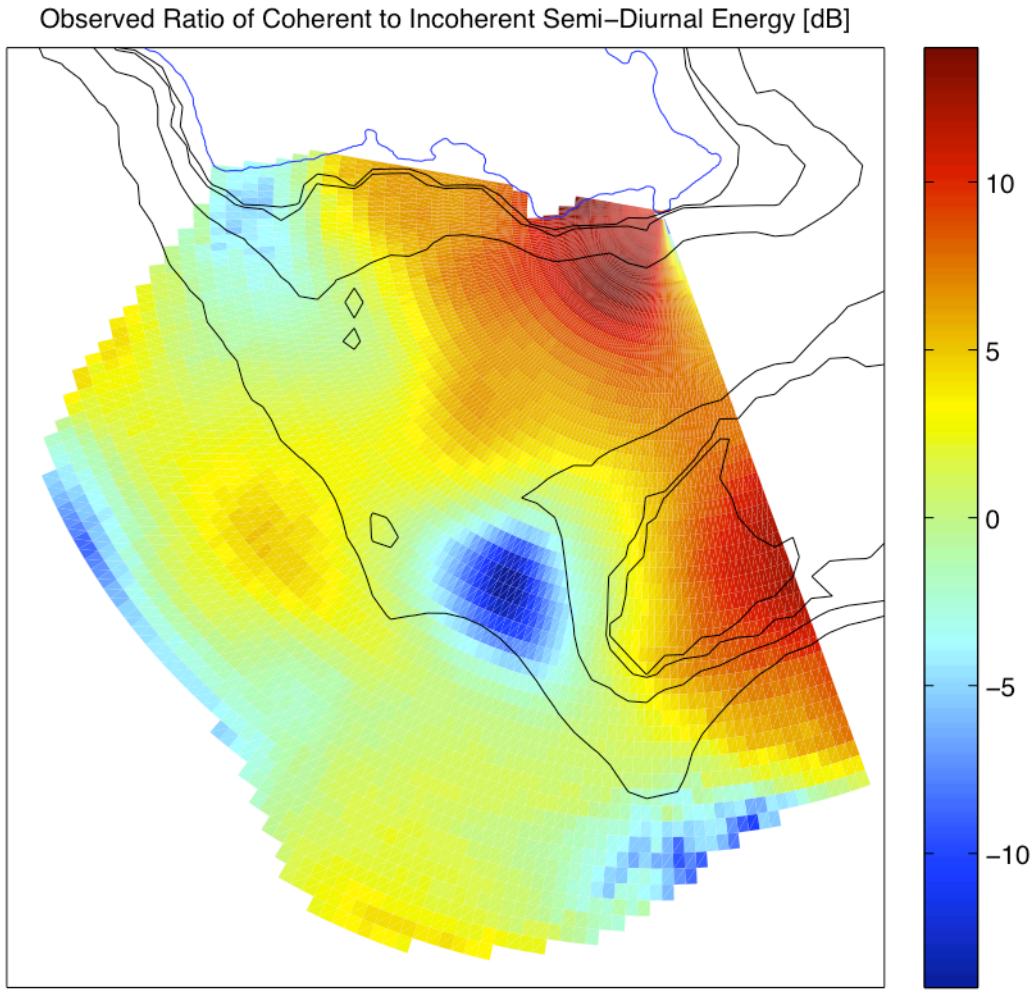

Figure 5.11: Ratio of coherent to incoherent semi-diurnal tides as observed in radial current record.

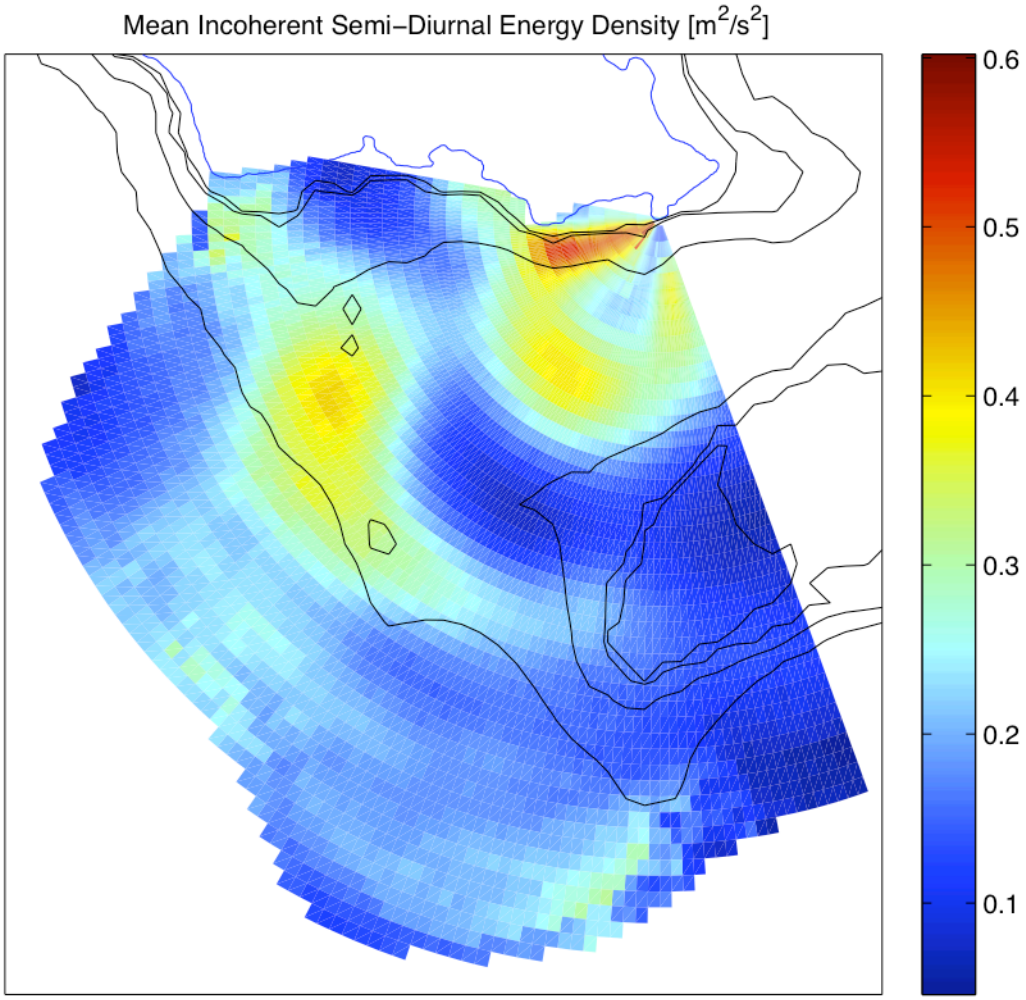

Figure 5.12: Incoherent semi-diurnal tidal energy density as observed in radial current record.

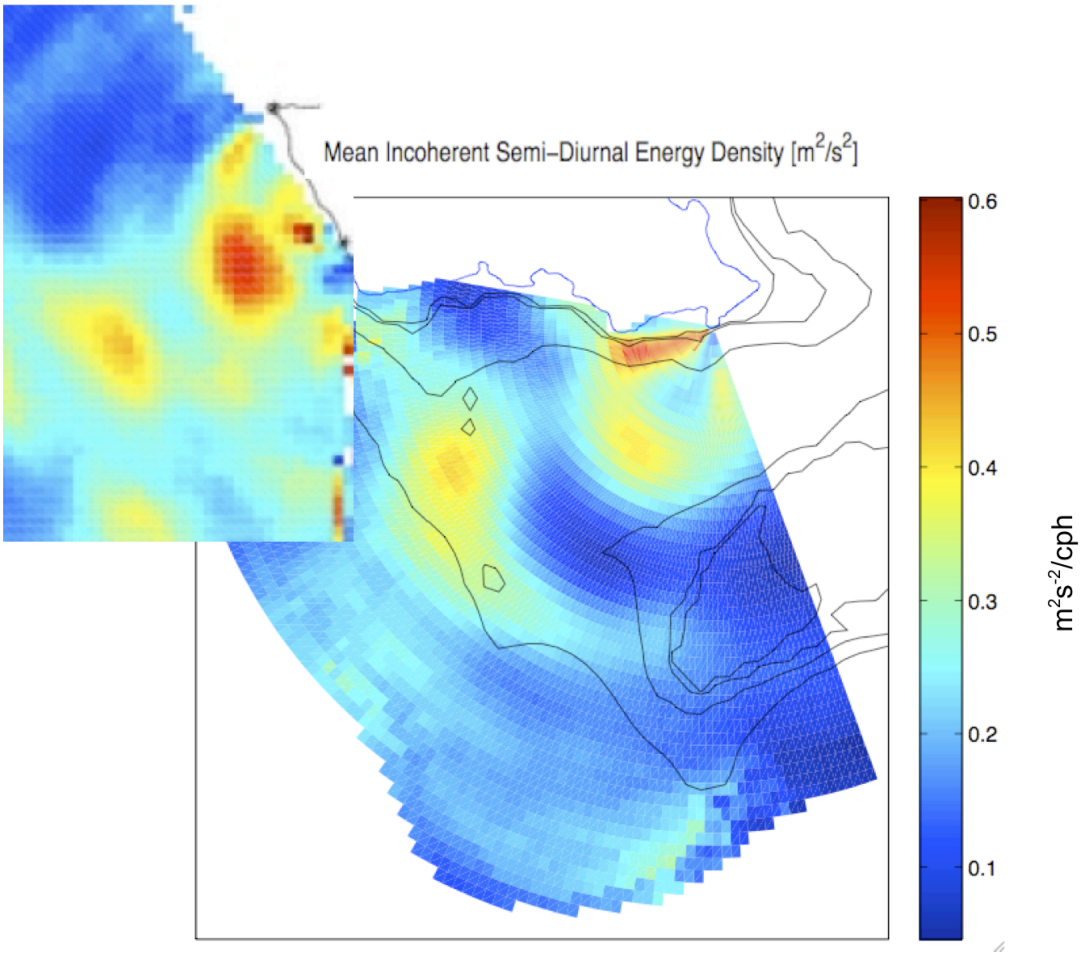

Figure 5.13: Same as figure 5.12 except with portion of a figure from a parallel analysis of currents west of Oahu during HOME by C. Chavanne overlaid.

Chapter 6

Detection of Tsunamis

6.1 Tsunami Overview

Large earthquakes present a grave risk to lives and property near tectonically active areas. The Pacific basin, ringed with active margins and volatile subduction zones, is particularly susceptible to these naturally occurring disasters. When earthquakes occur at the sea floor, or result in an under water landslide, tsunamis may be triggered. The most notorious event in the recent past was the December 26, 2004 Indian Ocean tsunami triggered by a 9.0 magnitude earthquake near Sumatra, Indonesia (Merrifield et al., 2005). The ensuing tsunami killed nearly 300,000 people and left many coastal communities through Indonesia, Thailand, Sri Lanka and other surrounding areas destroyed (Tiampo et al., 2008).

Prior to establishment of the Deep Ocean Assessment and Reporting of Tsunamis (DART) network it was hypothesized that an incoming tsunami's period, wave height and direction of propagation could be detected by an HFR, providing warning prior to its arrival (Barrick, 1979). As a tsunami approaches a coastline from the open ocean it will encounter shallower water that decreases its speed of propagation. During this shoaling process, the tsunami's period remains fixed while its wavelength decreases causing an increase in amplitude. The current fluctuation induced by the increased orbital velocity is what could potentially be detected (Barrick, 1979).

While no HFR current meters have actually recorded a tsunami approaching shore, simulations have been conducted to evaluate this hypothesis (Lipa et al., 2006; Dzvonkovskaya et al., 2009). The simulations consist of superimposing currents excited by a modeled tsunami with observed currents at various theoretical and existing HFR sites. This approach shows that the currents can be significant

enough to be detected by HFRs.

The September 2009 Samoan and February 2010 Chilean tsunamis provided opportunities to evaluate the tsunami detection capability of HFR current meters. The following chapter presents an analysis of available pressure sensors to characterize the tsunami events, estimate the magnitude of currents potentially excited and HFR current observations during the events.

On September 29, 2009, a magnitude 8.0 earthquake at the ocean floor near the Tonga trench generated a tsunami that shortly thereafter hit the Samoan and Tongan islands (NOAA, Pacific Tsunami Warning Center). The ensuing disturbance caused the most damage in Pago Pago, American Samoa and around the islands of Western Samoa where 192 residents were killed and several villages were swept into the sea. The maximum run-up height of 16.3 meters was recorded in Pago Pago, American Samoa (NOAA, Pacific Tsunami Warning Center).

On February, 27 2010 a magnitude 8.8 earthquake occurred off the south west Chilean coast about 230 km to the south of where the 1960 magnitude 9.5 earthquake triggered the infamous 10+ meter tsunami in Hilo. The greatest degree of damage from this earthquake resulted in nearby Chilean communities caused 521 deaths, thousands injured as well as widespread collapse of bridges and buildings. While the resulting tsunami put the Pacific basin in warning mode, the actual impact of the tsunami was minimal (except in Chile). The largest amplitude recorded, 11.2 meters, was 63 km from the epicenter in Talcahuano, Chile. (NOAA Satellite and Information Service, National Geophysical Data Center).

6.2 Instruments, Methods and Discussion

In 2008 NOAA completed deployment of a network of 39 DART stations in areas where destructive tsunamis have historically been generated. Each station consists of a bottom mounted pressure sensor that broadcasts its readings to a buoy on the surface via an acoustic modem. Data is then transmitted via satellite link to the Hawaii and Alaska Tsunami Warning Centers in near realtime.

The sensors are designed to continually provide 15 minute running mean readings under normal conditions. If anomalous changes in sea surface height are detected, the pressure gauge will automatically switch into a 1 minute or 15 second recording mode (Milburn et al., 1996). Data from the DART stations near Samoa, Tonga, Saipan, French Polynesia, Hawaii and Peru were investigated to characterize the tsunamis in open ocean.

DART observations do not occur at regular intervals in time so the record was adjusted to a regular interval of 1 minute observations. Gaps in data were linearly interpolated. Low frequencies were removed from DART and tidal records by decimating to hourly observation periods and resampling back to original time grid. Residual time series were generated by subtracting the decimated time series from the original record (figures 6.1 and 6.2).

Power spectra of the residual DART records over 3 hour segments sliding every 1.5 hours was computed to show the dominate period of the oscillation through the Chilean event. The mean energy density over the frequency bands corresponding 4-10, 10-15 and 15-40 minute periods are presented as a time series (figure 6.3).

Since the DART buoy near Hawaii malfunctioned during the event, the amplitude of the tsunami in open ocean must be estimated by observations at other stations. Using a inverse distance weighted average, the magnitude of the Samoan tsunami was estimated to be ~ 15.1 cm when approaching Hawaii. DART residual time series amplitude from the Chilean event was consistently larger than the Samoan tsunami for all stations. The Honolulu buoy was operational and measured oscillations of 35 cm, undoubtedly more significant than estimates for the Samoan event. Investigation of the power spectral density through time shows that the dominant signal observed by the buoy near Hawaii was in the 4-10 minute period band.

Assuming wave amplitude and dominant period from the DART data represent the tsunami's characteristics when it reached Hawaii, the manipulation equations in appendix C can be used to

predict the theoretical currents excited as the wave encounters shallower water. For the Samoan and Chilean tsunamis, currents of ~5 cm/s and ~12 cm/s are predicted.

While currents of 5-12 cm/s are well within the HFR's detection limits under normal operating conditions, the high frequency nature of tsunami waves must be considered. Velocity precision for the HFR follows the relationship:

$$precision = \frac{c}{fT} \qquad 6.1$$

where c is the speed of light, f is frequency and T is averaging time. This curve is show in figure 6.4 and precision for normal operation mode and each tsunami event is annotated. Based on the observed period and predicted current magnitude of each event, both tsunamis falls outside of the detection limits of the HFR.

The Koko Head HFR was active for both tsunami events. In normal operating mode data is continually collected over 12 minute intervals every 15 minutes. During the remaining 3 minutes direct path and other calibrations are conducted. The HFR was in normal operation mode during the Samoan tusnami event. During the Chilean tsunami settings were adjusted to increase radial resolution to 600 m (compared to 1.5km) and the recording mode was adjusted to continually collect and record data.

Typical output from the HFR is the radial current averaged over the observation period. In attempt to mitigate potential aliasing of the higher frequency tsunami signal, K.-W. Gurgel developed a subsampling program that allows analysis of the raw current data averaged over shorter periods. For investigating the Samoan event, the data was subsampled at 90 second periods then subsampled again to 45 second observations for synchronous comparison with the two minute sampling Makapuu pressure gauge. The resampled record was high passed by subtracting the corresponding twelve minute averaged sample. The resulting record contained series of fifteen 45 second samples followed by 3.75 minute data gaps. An analogous resampling and high pass routine was conducted on the Makapuu

pressure sensor.

6.3 Numerical Analysis

Due to the small magnitude and short period of the tsunami events in Hawaii, inspection of the data directly did not show evidence for detection of the tsunami. In attempt to amplify any evidence of the tsunami detected by the HFR, averaging methods to isolate the signal were conducted.

Assuming the currents excited within the domain fluctuated at the same frequency as the sea level deviations, a complex demodulation using the the oscillation of the Makapuu pressure sensor as a clock was conducted for the Samoan tsunami. Analysis for the Chilean event is pending modifications of the analysis routine to handle the setting differences employed. A normalization factor to ensure only the phase of the pressure sensor affected the complex demodulation was used:

$$n = \sqrt{P^2 + imag(hilbert(P))^2} \tag{6.2}$$

where P is the magnitude of the high passed pressure record. Currents in and 90° out of phase with the pressure sensor were isolated by multiplying the normalized pressure record or its hilbert transform by the high passed current record.

$$CUr = \frac{P}{n} * Ur \tag{6.3}$$

$$SUr = \frac{hilbert(P)}{n} * Ur \tag{6.4}$$

Ur is radial current. The preceding C and S signify the in and out of phase components of the current. Variance of the 2 phase dependent parts of the current record was computed as:

$$VUr = |(CUr * i\,SUr)| \tag{6.5}$$

Spatial average of high passed and complex demodulated variance during the Samoan is shown in figure 6.5. A similar complex demodulation procedure was conducted using a fixed frequency of 1/9 minutes, corresponding to the dominant period apparent in the Makapuu pressure record and Honolulu

DART buoy. The fixed frequency complex demodulation did not reveal a significant difference in variance following the event.

6.4 Conclusion

Available DART records were analyzed to characterize the open ocean period and amplitude for the Samoan and Chilean tsunamis. Theoretical induced current magnitudes resulting from the events were computed to be outside the detection limits of the HFR. Sub-sampling and complex-demodulation analysis of the Samoan event event does not reveal a disturbance attributable to the tsunami. Analysis of the Chilean tsunami pends.

While HFRs have been hypothesized and advertised as being capable of detecting tsunami events, their effectiveness is dependent on low ambient electromagnetic noise levels and a significant signal for detection. Had the tsunami's amplitudes been larger or periods longer the probability of detecting them in the HFR record would have been improved.

Reliance on an HFR network to characterize tsunamis or provide advance warning is not recommended. Pressure sensing DART buoys provide a fast, reliable and relatively inexpensive way to detect tsunamis across ocean basins.

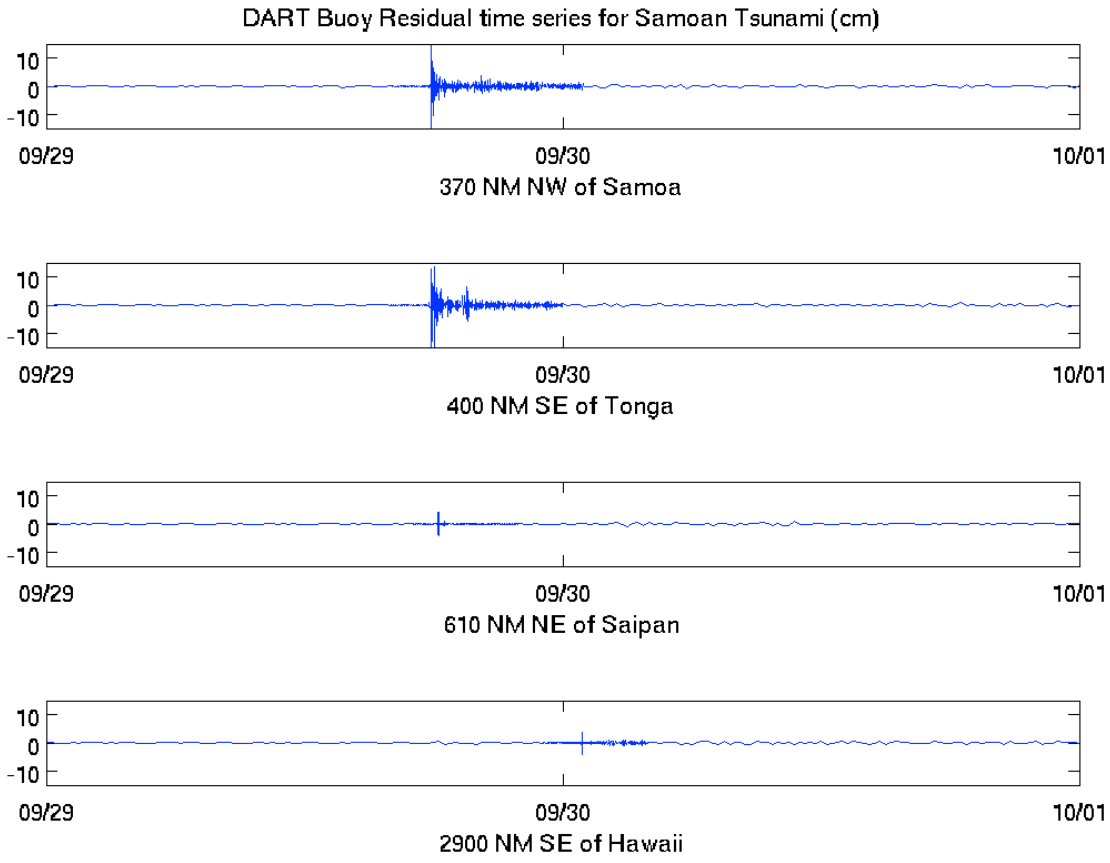

Figure 6.1: Residual pressure record from DART buoys during Samoan tsunami event (cm).

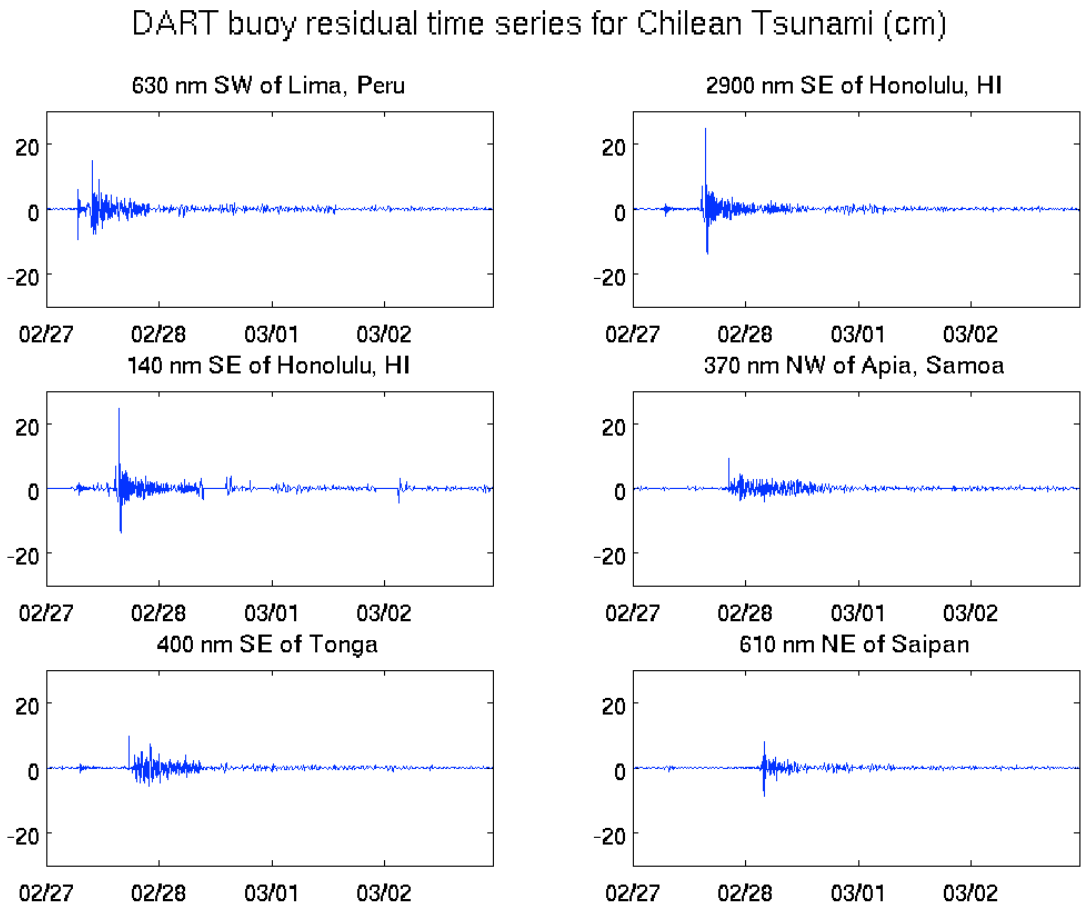

Figure 6.2: Residual pressure record from DART buoys during Chilean tsunami event (cm).

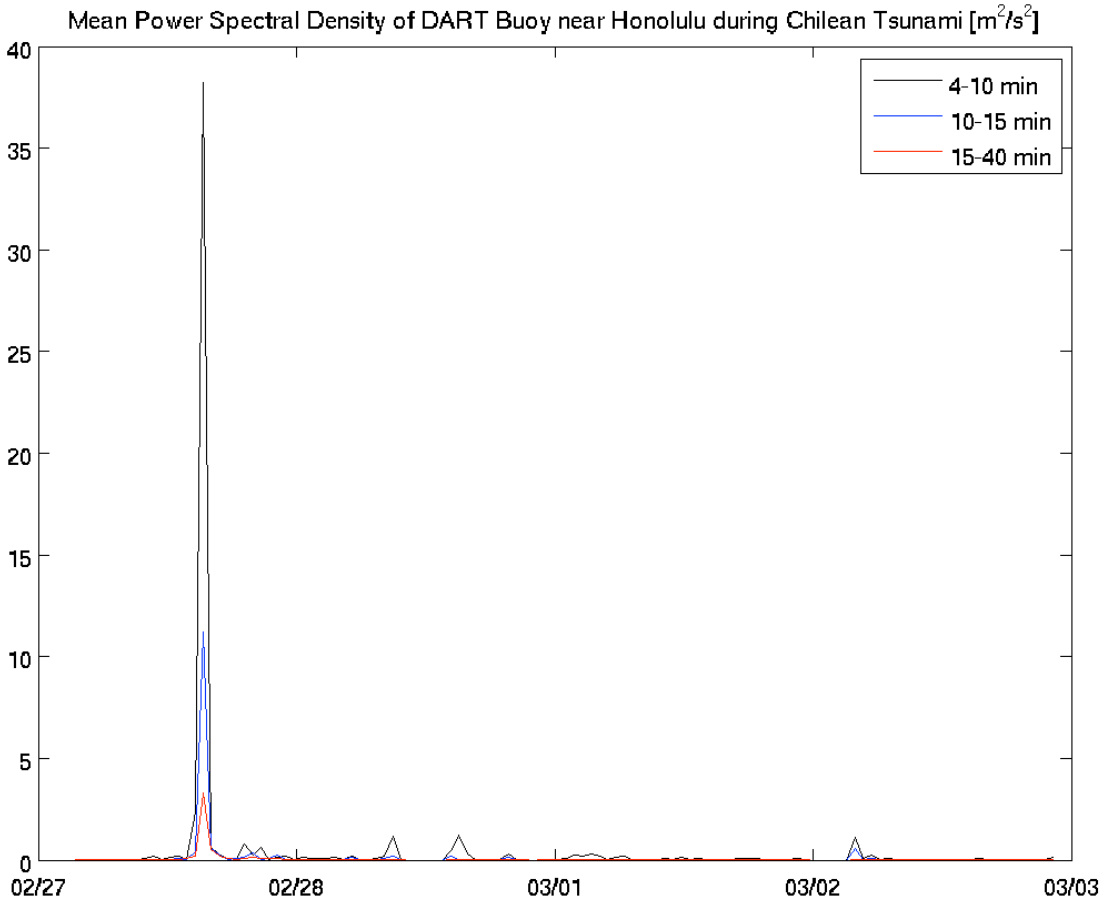

Figure 6.3: Mean energy for high frequencies from Honolulu DART buoy during arrival of Chilean tsunami (m^2/s^2).

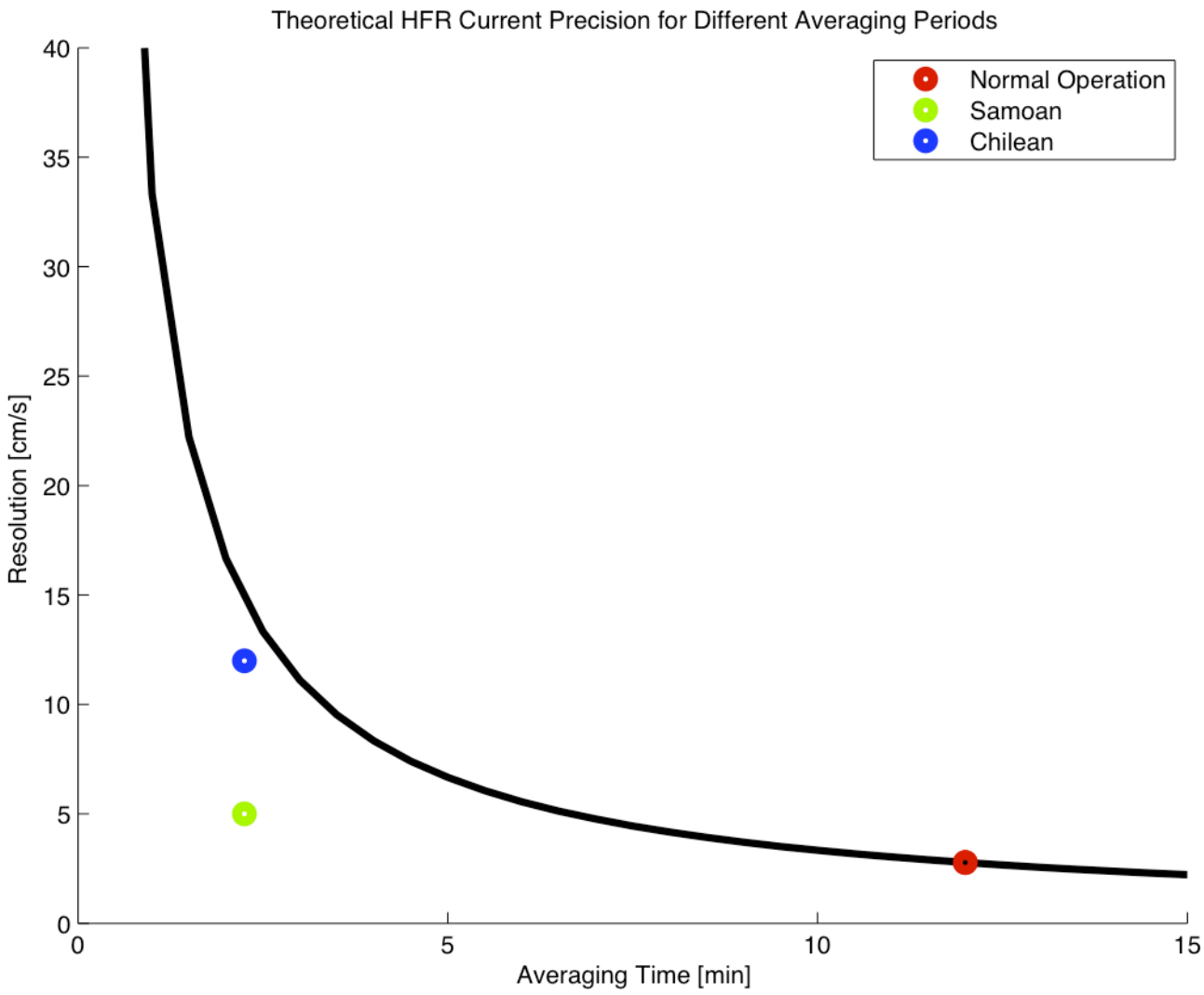

Figure 6.4: Theoretical HFR precision for different averaging periods.

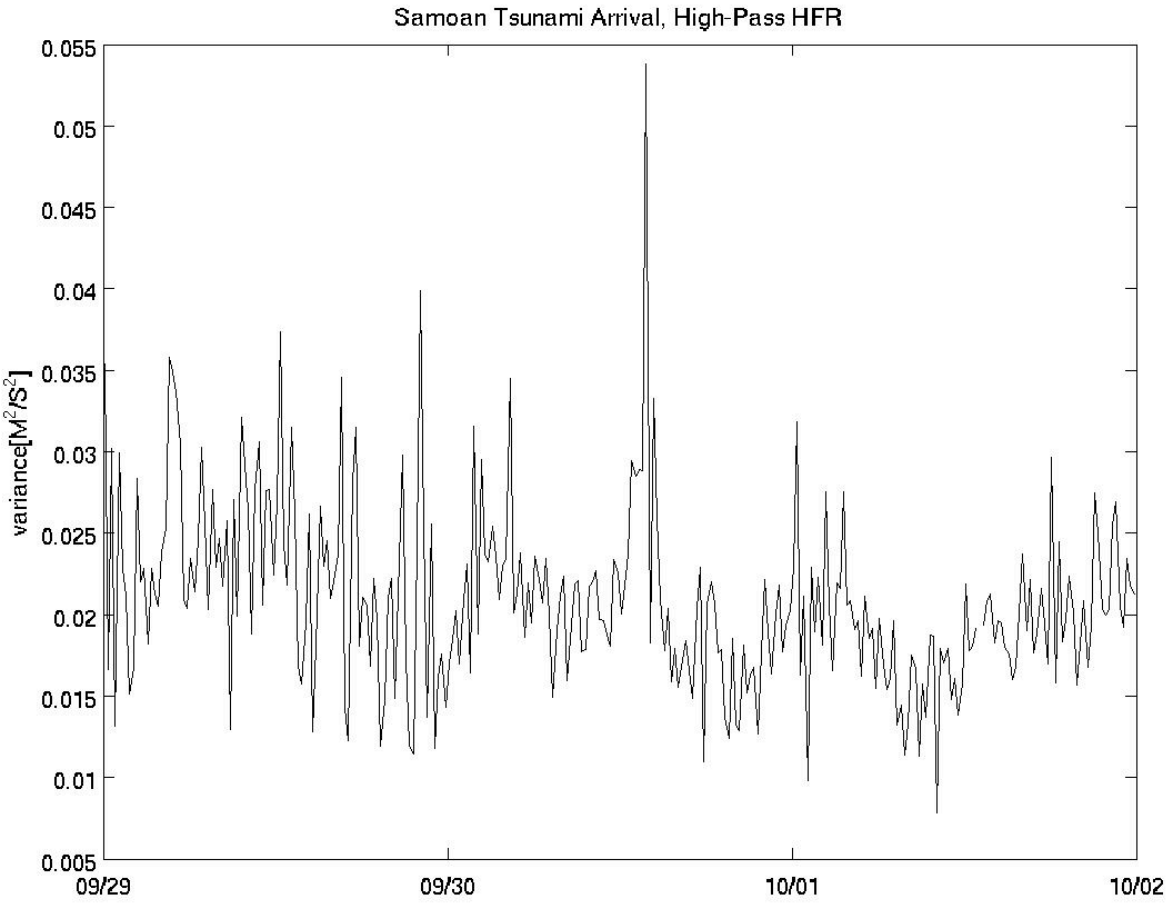

Figure 6.5: High-passed, complex demodulated, spatial average of HFR variance during Samoan tsunami event (m^2/s^2).

Chapter 7

Conclusions

Complex dynamics south of Oahu were observed with radial current data from a lone HFR atop Koko Head on Oahu's south east shore.

At lower frequencies the geostrophic approximation allows solution of the two dimensional stream function and vector currents. Vector current features show areas of enhanced vorticity and strain as well as a possible eddy generation zone down stream of Penguin Bank. Vorticity and strain plots can be used to identify areas of interest for pending drifting buoy deployments. As a validation of the vector current generation technique, inferred low frequency currents can be compared with vectors generated by the two sites following the activation of the Barber's Point HFR. Similarly, an analogous comparison could be done from the HOME HFR data between Kaena Point and Ko'olina sites.

ITW signals near Oahu require a longer time series for isolating the gravest mode. Two-site generated vector currents may permit isolation and removal of inertial motions, leaving a residual record for ITW investigation.

Deterministic processes such as tides are largely explained with a single dimension. Modeled tides generally agree with observed radial tidal characteristics. Extending radial observation of tides to future sites can provide a valuable data set for comparison with and assimilation into models.

Detecting high frequency signals associated with a tsunami is dependent on signal strength and very precise settings on the HFR. Development of a tsunami detection mode with continuous acquisition, similar to the settings employed during the Chilean tsunami, may improve the probability of capturing such a signal. However, precision of the HFR is not high enough to detect short period and small events such as the Samoan tsunami.

With the capacity of HFRs at detecting tides and low frequency curretns shown, activation of deployment locations without complimentary sites is supported. Activation of future sites such as the secondary array at Koko head and reactivation of the Kaena Point site should be pursued. With the planned and existing sites activated, low frequency trends and tidal patterns could be mapped for nearly half of O'ahu's circumference. Tidal patterns collected can be used to further refine models and provide indications of the complex internal tide generation at Kaena Ridge and Makapuu point. Seasonal trends, vorticity and strain can be incorporated into Coast Guard search and rescue planning and pollution response operations.

Appendix A

Beamforming Calibration

On March 9, 2010 a shipboard beamforming calibration was conducted with the assistance of local U.S. Coast Guard. The USCGC KISKA, equipped with a 10-W continuous sinusoidal transmitter, traveled on reciprocal arcs 10 nautical miles away from Koko Head. Two GPS receivers recorded the ships location every two seconds for geographic reference. The calibration was aborted at a bearing of 160°T from Koko Head (corresponding with the easterly extent of the HFR footprint) due to unfavorable wind and sea conditions causing ~15 degree pitches and excessive rolls. The path the ship followed is shown in figure A.1. An equivalent calibration was conducted with the assistance of Sector Honolulu's Vessel Boarding and Security Team aboard a 25' safe boat on March 24, 2010.

Beamforming is combining multiple omni-directional signals, from receivers separated in space, to yield a single directional signal. Consider a complex electro-magnetic (EM) wave incident on multiple receiving antennas. The measured signal follows the wave equation:

$$A(x) = e^{i(k \cdot x - wt)} \qquad \text{A.1}$$

where A is typically measured voltages for each antenna at vector position **x**. The frequency w and time t of the measurements are known. The EM wavenumber $k_0 = |k|$ is also known. The unknown is the direction of the EM wavevector **k**. The vector dot product $k \cdot x$ describes the phase of the incident wave. Thus the unknown direction of an incident EM wave can be determined from the relative phases of the measured signal A(**x**). Likewise, the measured signals can be beamformed in a desired direction:

$$A_B = \sum A(x) e^{i(k_B * x)} \qquad \text{A.2}$$

where k_B is the wavevector from the desired incident direction with wavenumber k_0 . The summation creates an interference between the signals; those in the desired direction will be constructive, other directions will be destructive.

By controlling the relative phases of summed signals, incidence angle of the signal transmitted by the ship was determined. Prior to any adjustments in the HFR configuration the correlation between the orientation of the ship, as determined by GPS and as inferred from beamforming, was very poor (figure A.2).

Analysis of the phase (conducted by Tyson Hilmer) during the ship calibration led to the discovery during hardware adjustments cable leads between components were inadvertently swapped. Additionally, two cable leads from the antenna were swapped because a label had been damaged. The improper reconnection caused the antennae to be processed in the wrong order resulting in insensible beamforming. After examination of relative phase a proper order of antenna was determined. With the antennae re-ordered, correlation between the beamformed and GPS incident angle was vastly improved (figure A.3). All data was re-processed with the proper antenna ordering.

To assess the beamforming performance of the receive array the sum of the energy from all angles received across all angles steered was computed and compared to theoretical beamforming (figure A.4). While minor side lobes are apparent, the energy is primarily focused in the steered direction resulting in effective concentration of the beam.

During the calibration the transmit array was switched to a receive mode to allow beamforming to be assessed as well (figure A.5). The main lobe of the transmit array is projected towards Mamala Bay as intended.

The ability to differentiate direction is less effective at Kaka'ako than Koko Head due to the shorter array (figure A.6). With angles steered further than ~30-45° from the normal, energy is spread over a large directional range. Kaka'ako is primarily intended to constrain cross-shore vector currents

along the baseline between Koko Head and Barber's Point and will adequately fulfill this intent. However, with the very small area of overlap between Kaka'ako with Koko Head alone, vector currents were not rigorously investigated.

The ship calibration highlighted an error in the hardware configuration that was corrected and data reprocessed. The beamforming performance closely mimics theoretical values, lending credit to the analysis contained in this work.

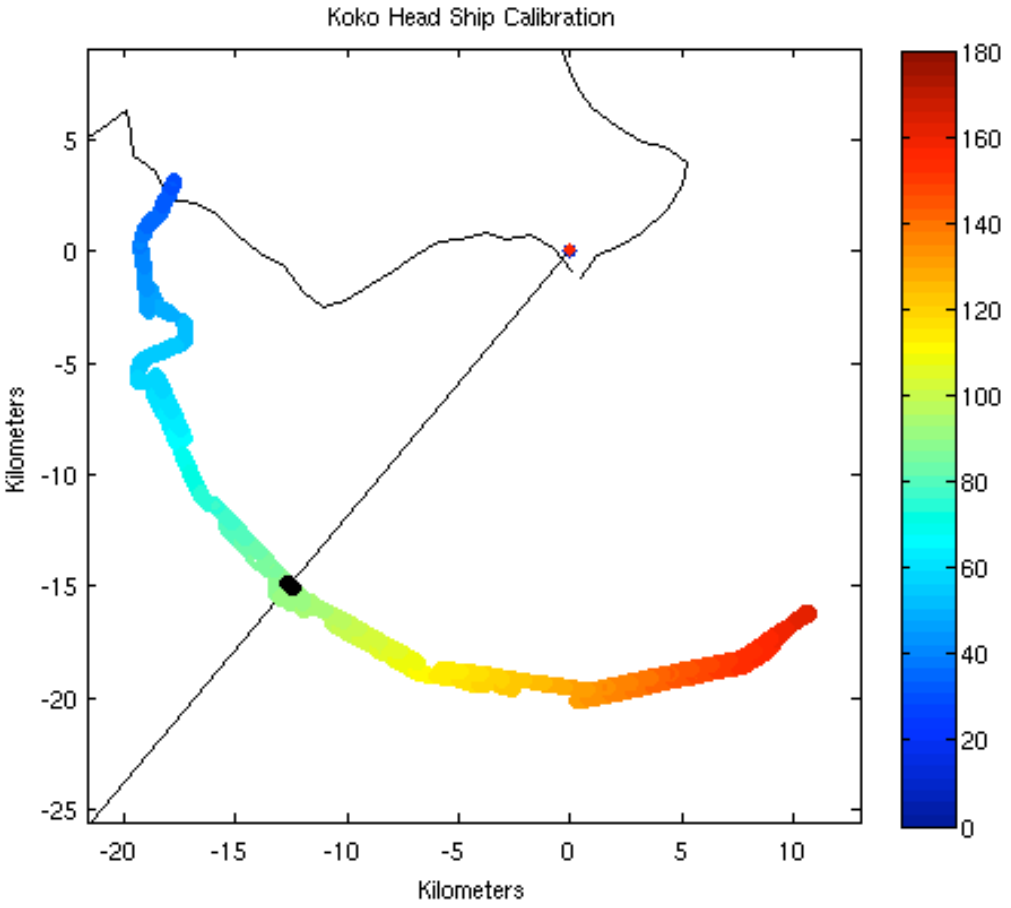

Figure A.1: GPS track of CGC KISKA during beamforming calibration for Koko Head. Color contour shows relative angle of ship from receive array with the thin black line indicating orthogonal.

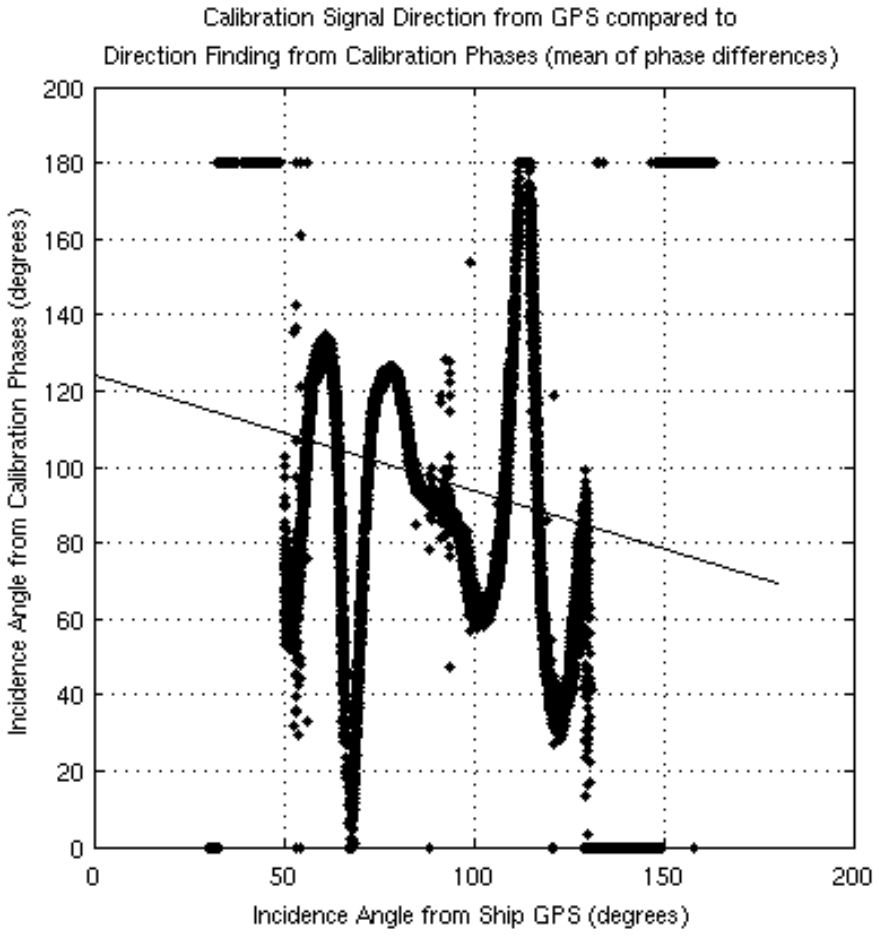

Figure A.2: Scatter plot of incidence angle of signal inferred by Koko Head HFR and actual incidence angle from GPS record during ship calibration prior to antenna reordering.

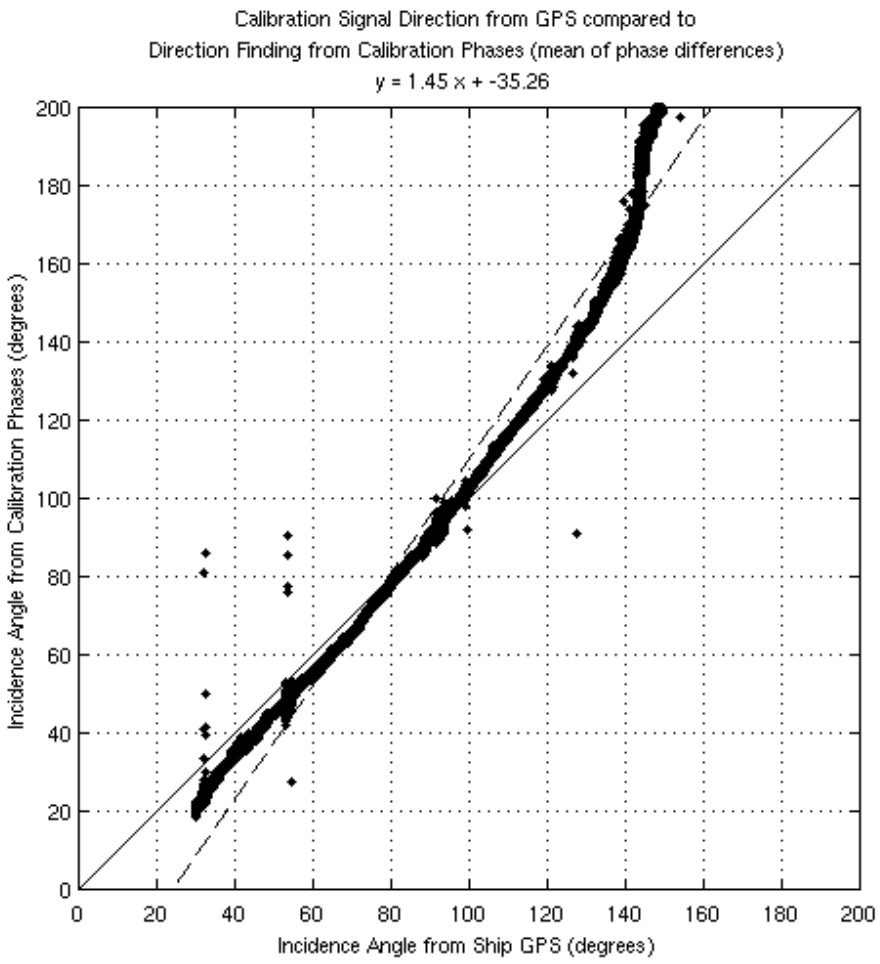

Figure A.3: Scatter plot of incidence angle of signal inferred by Koko Head HFR and actual incidence angle from GPS record during ship calibration after antenna reordering.

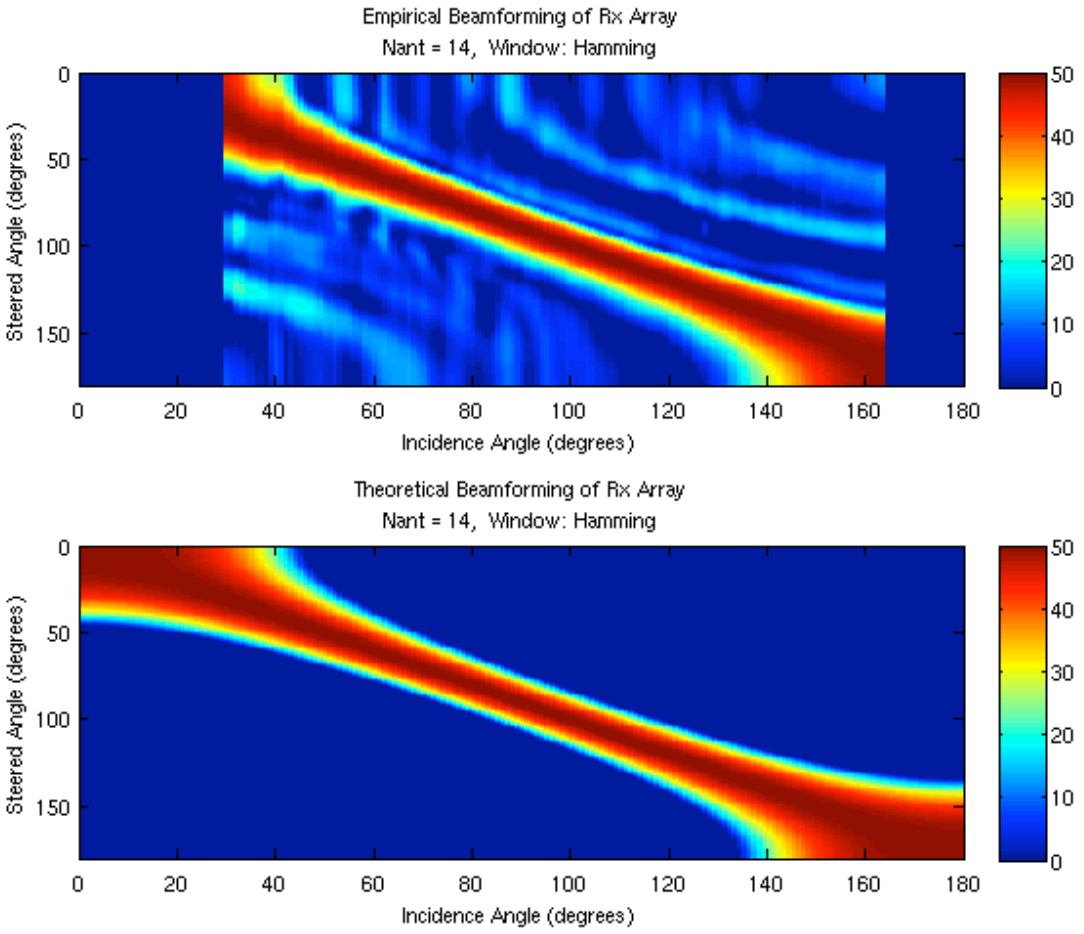

Figure A.4: Contour of empirical and theoretical beamforming performance by Koko Head receive array.

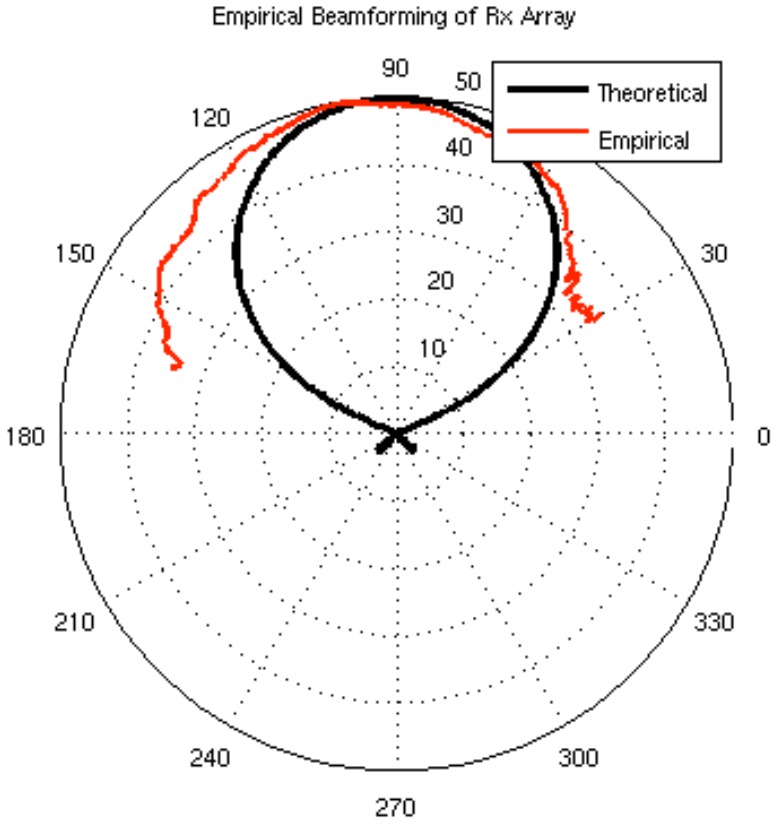

Figure A.5 Beamforming assessment of Koko Head transmit array from ship calibration.

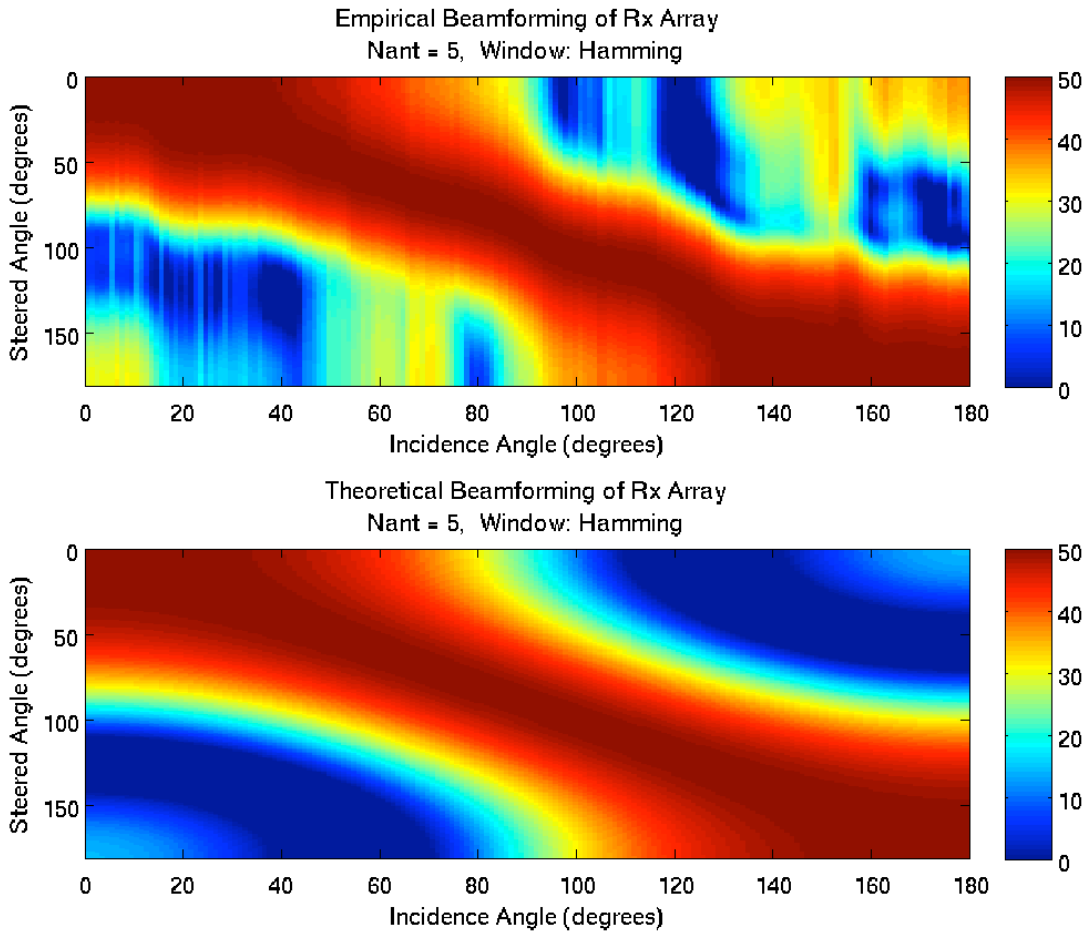

Figure A.6: Contour of empirical and theoretical beamforming performance by Kaka'ako receive array.

Appendix B

Decomposition of Velocity Gradient Tensor in Polar Coordinates

As shown by Futch (2010) the velocity gradient tensor can be broken down into two main components: an antisymmetric part, representing vorticity, and a symmetric part, representing irrotational deformation.

The antisymmetric part, $\zeta_{T'}$ is one half of the difference between the velocity gradient tensor and its transpose. The velocity gradient tensor in polar coordinates is:

$$T' = \begin{bmatrix} \frac{\partial u_r}{\partial r} & \frac{\partial u_\theta}{\partial r} \\ \frac{1}{r}\left(\frac{\partial u_r}{\partial \theta} - u_\theta\right) & \frac{1}{r}\left(\frac{\partial u_\theta}{\partial \theta} - u_r\right) \end{bmatrix} \quad \text{B.1}$$

where r indicates radial direction and θ indicates rotation. Solving for the antisymmetric part:

$$\zeta_{T'} = \frac{1}{2}(T' - T'^{T}) = \frac{1}{2}\begin{bmatrix} \frac{\partial u_r}{\partial r} & \frac{\partial u_\theta}{\partial r} \\ \frac{1}{r}\left(\frac{\partial u_r}{\partial \theta} - u_\theta\right) & \frac{1}{r}\left(\frac{\partial u_\theta}{\partial \theta} - u_r\right) \end{bmatrix} - \begin{bmatrix} \frac{\partial u_r}{\partial r} & \frac{1}{r}\left(\frac{\partial u_r}{\partial \theta} - u_\theta\right) \\ \frac{\partial u_\theta}{\partial r} & \frac{1}{r}\left(\frac{\partial u_\theta}{\partial \theta} - u_r\right) \end{bmatrix} \quad \text{B.2}$$

$$\begin{bmatrix} 0 & \frac{\partial u_\theta}{\partial r} - \frac{1}{r}\left(\frac{\partial u_r}{\partial \theta} - u_\theta\right) \\ \frac{-\partial u_\theta}{\partial r} + \frac{1}{r}\left(\frac{\partial u_r}{\partial \theta} - u_\theta\right) & 0 \end{bmatrix} \quad \text{B.3}$$

with eigenvalues $\lambda_{1,2} = \pm i\zeta$. The flow is circular and traps particles. For an irrotational flow $\zeta = 0$.

The symmetric part of the velocity gradient tensor, $\eta_{T'}$, representing irrotational deformation, is one half of the sum of the velocity gradient tensor and its transpose:

$$\eta_{T'}=\frac{1}{2}(T'+T'^{T})=\frac{1}{2}\begin{bmatrix}\frac{\partial u_r}{\partial r} & \frac{\partial u_\theta}{\partial r}\\ \frac{1}{r}(\frac{\partial u_r}{\partial \theta}-u_\theta) & \frac{1}{r}(\frac{\partial u_\theta}{\partial \theta}-u_r)\end{bmatrix}+\frac{1}{2}\begin{bmatrix}\frac{\partial u_r}{\partial r} & \frac{1}{r}(\frac{\partial u_r}{\partial \theta}-u_\theta)\\ \frac{\partial u_\theta}{\partial r} & \frac{1}{r}(\frac{\partial u_\theta}{\partial \theta}-u_r)\end{bmatrix} \quad \text{B.4}$$

$$\begin{bmatrix}\frac{\partial u_r}{\partial r} & \frac{1}{2}(\frac{\partial u_\theta}{\partial r}+\frac{1}{r}(\frac{\partial u_r}{\partial \theta}-u_\theta))\\ \frac{1}{2}(\frac{\partial u_\theta}{\partial r}+\frac{1}{r}(\frac{\partial u_r}{\partial \theta}-u_\theta)) & \frac{1}{r}(\frac{\partial u_\theta}{\partial \theta}+u_r)\end{bmatrix} \quad \text{B.5}$$

The symmetric part can be further decomposed into an isotropic divergence, $\mathrm{Tr}(\eta_{T'})$ and a non-divergent strain, $\eta'_{T'}$. The isotropic divergence is:

$$Tr(\eta_{T'})=\frac{\partial u_r}{\partial r}+\frac{1}{r}(\frac{\partial u_\theta}{\partial \theta}+u_r) \quad \text{B.6}$$

while the non-divergent strain is:

$$\eta'_{T'}=\eta_{T'}-Tr(\eta_{T'})\delta_{12}/2 \quad \text{B.7}$$

$$\begin{bmatrix}\frac{\partial u_r}{\partial r} & \frac{1}{2}(\frac{\partial u_\theta}{\partial r}+\frac{1}{r}(\frac{\partial u_r}{\partial \theta}-u_\theta))\\ \frac{1}{2}(\frac{\partial u_\theta}{\partial r}+\frac{1}{r}(\frac{\partial u_r}{\partial \theta}-u_\theta)) & \frac{1}{r}(\frac{\partial u_\theta}{\partial \theta}+u_r)\end{bmatrix}-\begin{bmatrix}\frac{1}{2}(\frac{\partial u_r}{\partial r}+\frac{1}{r}(\frac{\partial u_\theta}{\partial \theta}+u_r)) & 0\\ 0 & \frac{1}{2}(\frac{\partial u_r}{\partial r}+\frac{1}{r}(\frac{\partial u_\theta}{\partial \theta}+u_r))\end{bmatrix} \quad \text{B.8}$$

$$\frac{1}{2}\begin{bmatrix}\frac{\partial u_r}{\partial r}-\frac{1}{r}(\frac{\partial u_\theta}{\partial \theta}+u_r) & \frac{\partial u_\theta}{\partial r}+\frac{1}{r}(\frac{\partial u_r}{\partial \theta}-u_\theta)\\ \frac{\partial u_\theta}{\partial r}+\frac{1}{r}(\frac{\partial u_r}{\partial \theta}-u_\theta) & \frac{-\partial u_r}{\partial r}+\frac{1}{r}(\frac{\partial u_\theta}{\partial \theta}+u_r)\end{bmatrix}=\frac{1}{2}\begin{bmatrix}\sigma_1 & \sigma_2\\ \sigma_2 & -\sigma_1\end{bmatrix} \quad \text{B.9}$$

with eigenvalues $\lambda_{1,2}=\pm(\sigma_1^2+\sigma_2^2)^{1/2}$. Since $\eta'_{T'}$ is non-divergent, its trace is zero, and it represents non-divergent strain only.

Since constructing vector currents was only possible by assuming the flow was non-divergent the only the strain was investigated and is illustrated in Chapter 3.

Appendix C

Estimation of Current Magnitude Excited by Tsunami Events

The mathematic manipulation contained within this section is based on Chapter 4 notes from University of Hawaii's OCN 660 Waves I notes (Luther).

A typical tsunami propagating in the open ocean has $\lambda >> D$ so is constrained by water depth. Long gravity waves are non-dispersive or independent of wave number.

$$c_\eta = \sqrt{(g\, H_0)} \qquad \text{C.1}$$

where c is phase speed, η represents the surface displacement, g is acceleration due to gravity and H_0 is depth. Assuming surface gravity waves are independent of density fluctuations and that water is incompressible, the momentum and continuity equations combine to produce the Laplace equation.

$$\nabla^2 p' = 0 \qquad \text{C.2}$$

where p' represents pressure perturbations. The free surface between the water and atmosphere can be represented by η which is a function of space and time. To establish a boundary condition at the water's surface, the pressure of the atmosphere and ocean must be equal at $z = \eta$. The vertical velocity at the surface is the material derivative of η.

$$w(x, y, z, t) = \frac{D\eta}{Dt} \qquad at\ z = \eta \qquad \text{C.3}$$

$$p^*_{ocean} = p_{atmosphere}\ at\ z = \eta \qquad at\ z = \eta \qquad \text{C.4}$$

The average pressure at the ocean's surface and the perturbations of pressure in space and time are the components of p^*.

$$p^*_{ocean} = p_0(z) + p'(x, y, z, t) \qquad \text{C.5}$$

A taylor series expansion at the surface where z=0, application of the hydrostatic relation and linearization the boundary conditions lead to:

$$p_0(0)+p'(x,y,0,t)-\rho_0(0)\,g\,\eta=p_{atmosphere} \qquad \text{C.6}$$

$$w(x,y,0,t)=\eta_t \qquad \text{C.7}$$

Subscripts will denote partial derivatives here forward. The time derivative of (C.6) with (C.7) substituted for η_t becomes:

$$p'_t-\rho_0\,g\,w=0 \qquad at\ z=0 \qquad \text{C.8}$$

The vertical momentum equation is:

$$w_t=\frac{-p'_z}{\rho_0} \qquad \text{C.9}$$

The time derivative of (C.8) with (C.9) substituted for w_t becomes:

$$p'_{tt}+g\,p'_z=0 \qquad at\ z=0 \qquad \text{C.10}$$

Applying the condition that there is no vertical velocity at the sea floor to (C.9) leads to:

$$w_t=-p'_z=0 \qquad at\ z=-H \qquad \text{C.11}$$

Equations (C.10) and (C.11) are the boundary conditions to be applied to Laplace's governing equation (C.2). Considering a solution that is periodic in one horizontal dimension and time and that is dependent on depth.

$$p'(x,z,t)=\Pi(z)e^{i(kx-\omega t)} \qquad \text{C.12}$$

Using (C.12), equation (C.2) admits the solution:

$$\Pi_{zz}-k^2\Pi=0 \qquad \text{C.13}$$

Assuming that

$$\Pi(z)=A\,e^{kz}+B\,e^{-kz} \qquad \text{C.14}$$

apply boundary conditions to solve for A and B. Using equations (C.12) and (C.14):

$$p' = (A e^{kz} + B e^{-kz}) e^{i(kx - \omega t)} \quad \text{C.15}$$

Boundary condition from equation (C.11) reveals:

$$\Pi_z = 0 \quad \text{C.16}$$

$$kAe^{kz} - kB^{-kz} = 0 \quad \text{C.17}$$

$$Ae^{2\mathrm{kz}} = B \quad \text{C.18}$$

Substituting (C.18) for B in (C.14):

$$\Pi(z) = Ae^{kz} + Ae^{-2\mathrm{kH}_0} e^{-kz} \quad \text{C.19}$$

Rearranging shows:

$$\Pi(z) = A e^{-kH_0} [e^{k(z+H_0)} + e^{-k(z+H_0)}] \quad \text{C.20}$$

$$\Pi(z) = A e^{-kH_0} \cosh(k(z+H_0)) \quad \text{C.21}$$

Where $A e^{-kH_0}$ can be considered a constant A. A representation of surface displacement can be expressed as:

$$\eta = a \cos(kx - \omega t) \quad \text{C.22}$$

Using (C.22) with the boundary conditions, A is related to amplitude of surface displacement by:

$$A = \frac{\rho_0 a g}{\cosh(kH_0)} \quad \text{C.23}$$

Using the real portion of p', (C.12), (C.21) and (C.23) combine as:

$$p' = \frac{\rho_0 a g}{\cosh(k H_0)} \cosh[k(z+H_0)] \cos(kx - wt) \quad \text{C.24}$$

Integrating the horizontal momentum equation with respect to time will provide horizontal velocity.

$$\int_0^t u_t \, dt = \int_0^t \frac{\frac{-\partial p'}{\partial x}}{\rho_0} dt \quad \text{C.25}$$

$$\int_0^t \frac{\partial p'}{\partial x} dt = \frac{-k \rho_0 g a}{\omega} \frac{\cosh(k(z+H_0))}{\cosh(k H_0)} \cos(kx - \omega t) \quad \text{C.26}$$

$$u = \frac{kga}{\omega} \frac{\cosh(k(z+H_0))}{\cosh(k\,H_0)} \cos(kx - \omega t) \qquad \text{C.27}$$

In Chapter 6, the Samoan and Chilean tsunami characteristics were estimated using available DART buoy data. Due to the outage of the Honolulu DART buoy during the Samoan event values had to be approximated. Using these characteristics the expected current excited from encountering a shallow shelf (60 meters) from open ocean depths (4000 meters) were computed. Values are summarized in Table C.1.

	Open Ocean Period	Open Ocean Amplitude	Expected Current at Penguin Bank
Samoan	~10 min	~ 15 cm	~5 cm/s
Chilean	~10 min	35 cm	~12 cm/s

For both events, only radial data from Koko Head was investigated. Considering the direction of propagation and the geographic orientation Penguin Bank to Koko Head HFR, a significant portion of the expected current would align in the radial component.

References

Alford, M. H., M. C. Gregg, and M. A. Merrifield. 2006. Structure, Propagation, and mixing of energetic Baroclinic Tides in Mamala Bay, Oahu, Hawaii. American Meteorological Society. 36. 997 – 1018.

Barrick, D. E. 1979. A Coastal Radar System for Tsunami Warning. Remote Sensing of Environment. 8, 353-358.

Beckenbach, E., and L. Washburn. 2004. Low-frequency waves in the Santa Barbara Channel observed by high-frequency radar. Journal of Geophysical Research. 109. C02010.

Carter, G. S. and M. C. Gregg. 2006. Persistent Near-Diurnal Internal Waves Observed above a Site of M2 Barotropic-to Baroclinic Conversion. Journal of Physical Oceanography. 36. 1136 – 1147.

Carter, G. S., M. A. Merrifield, J. M. Becker, K. Katsumata, M. C. Gregg, D. S. Luther, M. D. Levine, T. J. Boyd, and Y. L. Firing. 2008. Energetics of M2 Barotropic-to-Baroclinic Tidal Conversion at the Hawaiian Islands. American Meteorological Society. 38. 2205 – 2223.

Chavanne, C. 2007.Observations of the Impact of Mesoscale Currents on Internal Tide Propagation. PhD dissertation, School of Ocean and Earth Sciences and Technology, University of Hawaii at Manoa.

Chavanne, C. I. Janekovic, P. Flament, P.-M. Poulain, M. Kuzmic, and K.-W. Gurgel. 2007. Tidal currents in the northwestern Adriatic: High-frequency radio observations and model predictions. Journal of Geophysical Research. 112. C03S21.

Chavanne, C., P. Flament, R. Lumpkin, B. Dousset, A. Bentamy. Scatterometer observations of wind variations induced by oceanic islands: Implications for wind-driven ocean circulation. 2002 Can. J. Remote Sensing. 28, 466-474.

Chavanne, C., P. Flament, E. Zaron, G. Carter, M. Merrifield, D. Luther, E. Zaron, K.-W. Gurgel. 2010 a. The Surface Expression of Semidiurnal Internal Tides near a Strong Source at Hawaii. Part I: Observations and Numerical Predictions. Journal of Physical Oceanography. 40. 1155-1179.

Chavanne, C., P. Flament, D. Luther, K.-W. Gurgel. 2010 b. The Surface Expression of Semidiurnal Internal Tides near a Strong Source at Hawaii. Part II: Interactions with Mesoscale Currents. American Meteorological Society. Journal of Physical Oceanography. 40. 1180-1200.

Chavanne, C., P. Flament, K.-W. Gurgel. 2010 c. Interactions between a Submesoscale Anticyclonic Vortex and a Front. Journal of Physical Oceanography. 40. 1802-1818.

Duschaw, B. D. Mapping low-mode internal tides near Hawaii using TOPEX/POSEIDON altimeter data. Geophysical Research Letters. 29. 8. 1250.

Dzvonkovskaya, A., K-W. Gurgel, T. Pohlmann, T. Schlick, J. Xu. Simulations of Tsunami Signatures in Ocean Surface Current Maps Measured by HF Radar.

Eich, M. L., M. A. Merrifield, and M. H. Alford. 2004. Structure and variability of semidiurnal internal tides in Mamala Bay, Hawaii. J. Geophy. Res., 109, C05010.

Flament, P., R. Lumpkin, J. Tournadre, L. Armi. 2001. Vortex paring in an unstable anticyclonic shear flow: discrete subharmonics of one pendulum day. J. Fluid Mech. 440, 401-409.

Hamilton, P. 1996. Observations of tidal circulation in Mamala Bay, Hawaii, paper persented at North American Water and Environment Congress, Am. Soc. Of Civil Eng., Anaheim, Calif.

Hamilton, P., J. J. Singer, and E. Waddel. 1995. Ocean current measurements, final report, Mamala Bay Study, project MB-6, Mamala Bay Study Comm., Honolulu, Hawaii.

Hebenstreit, G. T., E. N. Bernard. 1985. Azimuthal Variations in Tsunami Interactions with Multiple-Island Systems. Journal of Geophysical Research. 90, 3353-3360.

Hilmer, T. 2010. Radar sensing of surface waves. Master thesis, School of Ocean and Earth Sciences and Technology, University of Hawaii at Manoa. (pending final submission)

Kunze, E. 1985. Near-Inertial Wave Propagation in Geostrophic Shear. Journal of Physical Oceanography. 15. 544-565.

Lipa, B. J., D. E Barrick, J. Bourg, and B. B Nyden. 2006. HF Radar Detection of Tsunamis. Journal of Oceanography, 62, 705-716.

Lumpkin, R., 1995. Resonant Coastal Waves and Superinertial Oscillations. Master thesis, School of Ocean and Earth Sciences and Technology, University of Hawaii at Manoa.

Lumpkin, C., 1998. Eddies and Currents of the Hawaiian Islands. PhD dissertation, School of Ocean and Earth Sciences and Technology, University of Hawaii at Manoa.

Lumpkin, R., P. Flament. 2001. Lagrangian statistics in the central North Pacific. Journal of Marine Systems. 29. 144-155.

Luther, D. S., Trapped waves around Hawaiian Islands, paper presented at 'Aha Huliko'a Hawaiian Winter Workshop, Univ. of Hawaii, Honolulu, 1985.

Luther, D.S., 1995: Waves trapped to discrete topography: existence and implications, *Proc., 8th `Aha Huliko'a Hawaiian Winter Workshop on the Interaction of Flow with Topography*, Univ. of Hawaii, January 17-20, l995, pp. 43-56.

Mofjeld, H. O., V. V. Titov, F. I. Gonzalex, J. J. Newman. 2001. Tsunami scattering provinces in the Pacific Ocean. Geophysical Research Letters. 28, 335-338.

Martini, K. I., M. H. Alford, J. D. Nash, E. Kunze, and M. A. Merrifield. 2007. Diagnosing a partly standing internal wave in Mamala Bay, Oahu. Geophysical Research Letters. 34. L17604.

Merrifield, M. A. and P. E. Holloway. 2002. Model estimates of M2 internal tide energetics at the

Hawaiian Ridge. Journal of Geophysical Research. 107. C8.

Merrifield, M. A., P. E. Holloway, and T. M. Shaun Johnston. 2001. The generation of internal tides at the Hawaiian Ridge. Geophysical Research Letters. 28. 4. 559-562.

Merrifield, M.A., Y. L. Firing, T. Aarup, W. Agricole, G. Brundrit, D. Chang-Seng, R. Farre, B. Kilonsky, W. Knight, L. Kong, C. Magori, P. Manurung, C. McCreery, W. Mitchell, S. Pillay, F. Schindele, F. Shillington, L. Testut, E. M. S. Wijeratne, P. Caldwell, J. Jardin, S. Nakahara, F.-Y. Porter, and N. Turetsky. 2005. Tide guage observations of the Indian Ocean tsunami, December 26, 2004. Geophysical Research Letters. 32, L09603.

Milburn, H.B., A.I. Nakamura, and F.I. Gonzalez. 1996. Real-time Tsunami Reporting from the Deep Ocean. *Proceedings of the Oceans 96 MTS/IEEE Conference*, 23-26 September 1996, Fort Lauderdale, FL, 390-394.

Pararas-Carayannis, George and Calebaugh P.J. 1977. Catalog of Tsunamis in Hawaii, Revised and Updated, World Data Center A for Solid Earth Geophysics, NOAA, 78.

Pawlowicz, R., B. Beardsley, S. Lentz. 2002. Classical tidal harmonic analysis including error estimates in MATLAB using T_TIDE. Computers and Geosciences. 28. 929-937.

Prince, J. P. and D. Elliott-Fisk. 2004. Topographic History of the Maui Nui Complex, Hawai'i and Its Implications for Biogeography. Pacific Science. 58. 1:27-45.

Ray, R. D., G. T. Mitchum. 1996. Surface Manifestation of internal tides generated near Hawaii.

Geophysical Research Letters. 23, 16. 2101-2104.

Rudnick, D. L., T. J. Boyd, R. E. Brainard, G. S. Carter, G. D. Egbert, M. C. Gregg, P. E. Holloway, J. M. Klymak, E. Kunze, C. M. Lee, M. D. Levine, D. S. Luther, J. P. Martin, M. A. Merrifield, J. N. Moum, J. D. Nash, R. Pinkel, L. Rainville, T. B. Sanford. 2003. From Tides to Mixing Along the Hawaiian Ridge. Science. 301, 355-357.

Tiampo, K.F., D.K. Weatherley, and S.A. Weinstein. 2008. Earthquakes: Simulations, Sources and Tsunamis

Wunsch, C. 1975. Internal Tides in the Ocean. Reviews of Geophysics and Space Physics. 13. 1. 167 – 182.

Xie, Shang-Ping, W. T. Liu, Q. Liu, M. Nonaka. 2001. Far-Reaching Effects of the Hawaiian Islands on the Pacific Ocean-Atmosphere System. Science. 292, 2057-2060.

Zaron, E. D. C. Chavanne, G. D. Egbert, P. Flament. 2009. Baroclinic tidal generation in the Kauai Channel inferred from high-frequency radio Doppler current meters. Dynamics of Atmospheres and Oceans. 48. 93-120.

Zaron, E. D. G. D. Egbert. 2006. Verification studies for a z-coordinate primitive-equation model: Tidal conversion at a mid-ocean ridge. Ocean Modelling. 14. 257-278.